

Electrospun Polymer - Liquid Crystal Composite Fibres

Dissertation

zur Erlangung des
Doktorgrades der Naturwissenschaften (Dr. rer. nat.)

der

Naturwissenschaftlichen Fakultät II

der Martin-Luther-Universität
Halle-Wittenberg,

vorgelegt

von Frau Eva Enz
geb. am 22.10.1981 in Waiblingen

Gutachter:

1. Prof. Dr. J.P.F. Lagerwall (Seoul National University)
2. Prof. Dr. M. Steinhart (Universität Osnabrück)
3. Prof. Dr. A. Blume (Martin-Luther-Universität Halle-Wittenberg)

Tag der Verteidigung: 16.04.2013

Contents

Abbreviations and Variables	iii
1 Introduction	1
2 Theoretical Background	3
2.1 Liquid Crystals	3
2.1.1 The Nematic and Smectic Phases	5
2.1.2 Introduction of Chirality: Cholesteric and Blue Phases	10
2.1.3 A special Case: Liquid Crystal Elastomers	13
2.1.4 Thermodynamic Aspects of LC Phase Transitions	15
2.1.5 Liquid Crystals in Confinement	17
2.2 The Electrospinning Process	22
2.2.1 Fundamental Principles	22
2.2.2 Factors affecting the Fibre Morphology	26
2.2.3 Fibre Collection: Nonwovens and aligned Fibres	32
2.2.4 Coaxial Electrospinning	33
3 Experimental Part	35
3.1 Development of the Setup for coaxial Electrospinning	35
3.2 Optimising the Polymer Solutions	38
3.3 Used Materials	40
3.4 Polarising Optical Microscopy	44
3.5 Differential Scanning Calorimetry	44
3.6 X-Ray Diffraction	44
3.7 Electron Microscopy	45
4 Alignment of electrospun Fibres	47
5 Fibres with Nematic and Smectic Liquid Crystals	55
5.1 5CB: a simple Nematic Liquid Crystal	55

5.2	8CB: Extension to a Smectic A Phase	56
5.2.1	X-Ray Investigations on Fibres	59
5.2.2	Fibre Morphology and Phase Transitions of the LC in Correlation to electrospinning Conditions	62
5.3	Further Extension to the tilted Smectic C Phase	71
5.3.1	Characterisation of the bulk LC Mixture	71
5.3.2	Fibres with this Core Material	74
6	Fibres with Cholesteric and Blue Phases	83
6.1	Finding a suitable LC Mixture	83
6.2	Phase Behaviour and optical Properties of the LC in PVP Fibres	87
6.3	SEM Investigations of the external Fibre Morphology - Variations of the Polymer Solution	97
7	Electrospinning with a liquid crystalline Elastomer	105
8	Summary and Outlook	109
8.1	Fibre Alignment	109
8.2	Core-sheath Fibres filled with Liquid Crystals	109
8.3	Fibres with the LC-Elastomer	111
A	Cano Lens Calculation	113
B	Calculation of the selective reflection wavelength in fig. 6.11	115
	Bibliography	117
	List of Figures	127
	List of Tables	131

Abbreviations and Variables

η	dynamic viscosity
θ	angle of incidence and scattering angle, respectively
λ_{refl}	reflected wavelength
τ	tilt angle in SmC phase
ϕ	deviation angle in order parameters
ϕ_p	volume fraction of a polymer in solution
χ	azimuthal angle in X-ray diffraction
5CB	4-cyano-4'-heptylbiphenyl
6OCB	4-cyano-4'-hexyloxybiphenyl
6OPhPy8	2-(4-hexyloxyphenyl)-5-octylpyrimidine
8CB	4-cyano-4'-heptylbiphenyl
8OPhPy8	2-(4-octyloxyphenyl)-5-octylpyrimidine
a. u.	arbitrary unit
AFM	Atomic Force Microscopy
BP*	Blue Phase
c	concentration
c^*	dilute – semidilute transition concentration of a polymer in solution
c^{**}	semidilute – concentrated transition concentration of a polymer in solution
c_e	critical entanglement concentration of a polymer in solution
c_p	heat capacity at constant pressure
CB15	(<i>S</i>)-4-cyano-4'-(2-methylbutyl)biphenyl
cryst.	crystalline phase
d_{core}	diameter of fibre core
d_{out}	outer fibre diameter
d_{SmA}	layer distance in the SmA phase from X-ray scattering

d_T	temperature-dependent layer distance from X-ray scattering
DSC	Differential Scanning Calorimetry
FIB	Focused Ion Beam
h	height of a collector
H	enthalpy
ΔH_m	melting enthalpy
ΔH_c	clearing enthalpy
I	intensity
iso.	isotropic phase
\mathbf{k}	layer normal in a liquid crystalline phase
l_{tube}	tube length
LC	liquid crystal
M	molar mass
M_w	weight-averaged molar mass of a polymer
M_e	average molar mass between entanglement couples in a polymer as melt
n	refractive index
$(n_e)_{solv}$	solution entanglement number
Δn	birefringence
\mathbf{n}	director in a liquid crystalline phase
N	nematic phase
N*	chiral nematic or cholesteric phase
Δp	applied pressure
p	pitch length in N* phase
p_o	natural pitch length in the chiral nematic phase
P	electrical power
POM	Polarising Optical Microscopy
PVA	poly(vinyl alcohol)
PVP	poly(vinyl pyrrolidone)
q	heat

\dot{q}	heat flow
R	universal gas constant
r_{lens}	radius of lens in Cano experiment
r_n	radii of defect rings in Cano experiment
r_{tube}	tube radius
RT-SmC-LC	room temperature smectic C liquid crystal
S_{2D}	2 dimensional order parameter
SAXD	small angle X-ray diffraction
SEM	Scanning Electron Microscopy
SmA	smectic A phase
SmC	smectic C phase
t	time
T	temperature
T_c	clearing temperature
T_m	melting temperature
V	volume
\dot{V}	volumetric flow rate
\dot{V}_{LC}	flow rate of liquid crystal
\dot{V}_{out}	flow rate of outer polymer solution
WAXD	wide angle X-ray diffraction
x	molar fraction

Chapter 1

Introduction

In this thesis I will present the first larger study on the combination of two very different scientific topics, electrospinning, a method to produce fibres with diameters in the micro- or even down to the nanometer range, and liquid crystals, fascinating ordered fluids with an unique combination of optical effects and responsiveness. Electrospinning has been invented already around the year 1900 by J. F. Cooley [1] and W. J. Morton [2], but only since the 1990s it has attended much, but now more and more growing, interest within the scientific community and recently also starts slowly to be attractive for non-academic applications. Fascinatingly liquid crystals were also first studied at about the same time [3, 4], but with their nowadays widespread use in display applications they are known even to the general public. So even though both topics were studied, with more or less emphasise, in parallel since quite a long time, only recently there has been interest in combining these two topics to create new, functional materials.

As a proof of principle the possibility to gain fibres with a liquid crystalline core by the use of coaxial electrospinning, a variation in which one solution is spun as a core fluid inside another serving as a sheath of the fibre, was first shown in 2008 by J. Lagerwall in collaboration with the group of Y. Xia [5]. A quite similar result was presented by Buyuktanir et al. in 2010 [6] for the use single-phase electrospinning of a polymer solution-liquid crystal mixture which phase-separated into a core-sheath structure during solvent evaporation. For this thesis nevertheless it was decided that coaxial electrospinning was in most cases the easier and more adaptable choice, as both fluids can be controlled separately and as it does not rely on a fast enough and sufficient phase separation during the fibre formation process, so that a better process and morphology control can be expected. In this way, core-sheath fibres with different liquid crystalline materials and phases, as well as with variations in the sheath composition, could be obtained and studied, extending and generalising the approach presented by Lagerwall et al. [5].

In a first main part a general introduction to liquid crystals and electrospinning with emphasis on the topics needed as background to this thesis. Then a general experimental question on fibre alignment during electrospinning is addressed, followed by the main results, the study of coaxial fibres with liquid crystals as core material. It will be shown that liquid crystals with relatively simple phases like nematic and smectic, as well as much more complicated phases like chiral nematic and Blue Phases can be used and their properties studied. It will be further shown that as sheath material the well-known and commercially available polymer poly(vinyl pyrrolidone) (PVP) or a composite of PVP and small amounts of titanium dioxide can be applied.

Depending on the sheath composition the resulting composite mats can be transparent so that the responsiveness and the optical properties of the core fluid are transferred to the macroscopic material, which in the long-term could make them interesting as functional materials for sensor applications or “smart” clothing. Another, more fundamental aspect, is the possibility to study the liquid crystal phases in a new geometric environment, differing from the well-known planar-plate geometry but also from studies with cylindrical confinement but much smaller diameters. Finally, with fibres spun from a liquid-crystal elastomer also a system is briefly studied, in which the polymer itself builds up the LC phase so that no core-sheath structure should be needed for encapsulation this structure into fibres.

Chapter 2

Theoretical Background

2.1 Liquid Crystals

Liquid crystal (LC) phases are distinct states of matter that in certain cases appear between the ordinary crystalline solid and the isotropic fluid state that are schematically drawn in the phase diagram in fig. 2.1. They are extraordinary because they are anisotropic fluids, which means that on the one hand they are mobile, flowing materials but on the other hand they are partly ordered states leading to anisotropy in their physical properties. The fluidity can resemble that of normal liquids, while ordered structures and anisotropy are generally known from crystalline solids. Because of this intermediate character the liquid crystalline phases are often also called *mesophases* and the molecules forming them as *mesogens*.

The reason for this unexpected combination of properties of liquid crystals can be traced to the anisotropy of their building blocks. These can be either anisometric shaped molecules leading to a phase sequence mainly dependent on temperature and are therefore referred to as *thermotropic* liquid crystals (from principle thermodynamic aspects also pressure is a variable, but this is mostly neglected). A second kind of building blocks are aggregates of amphiphilic molecules in water leading to the formation of *lyotropic* liquid crystals. Their phases are mainly determined by the concentration of the amphiphiles and only slightly temperature dependent. These phases often occur in biological systems, e. g. in membranes, but also in everyday situations like surfactant-water systems like soap solutions and shampoo. As they were not part of this thesis work they will not be further covered, but a brief introduction into the most important aspects can be found for example in [7].

Thermotropic liquid crystals can be further distinguished with respect to the shape of the mesogen molecules. The most important are the *calamitic* or rod-like and the *discotic* or disc-like molecules as sketched in fig. 2.2. Both basic forms consist of a rigid core, represented as the ellipse or circle in the sketch, respectively, built up from several

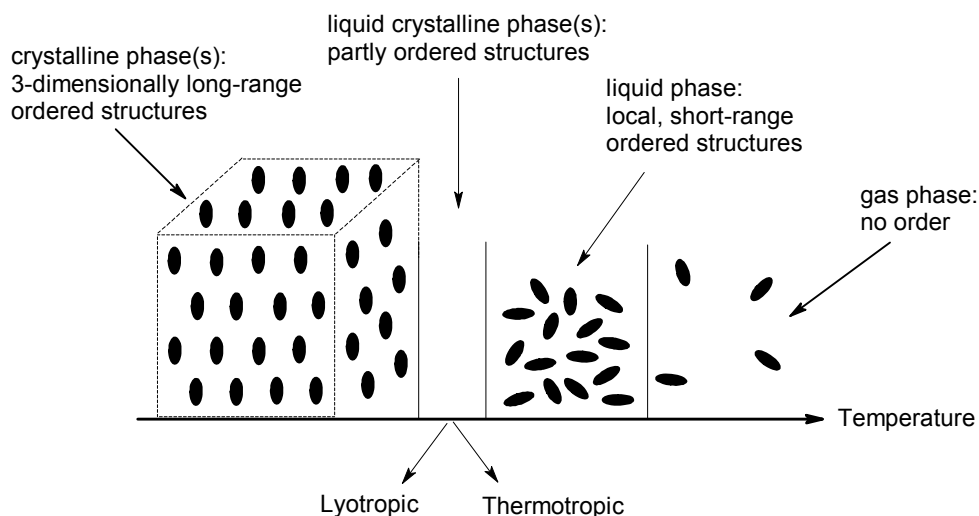


Figure 2.1: Generalised phase diagram with the liquid crystals added to the three classical phases.

phenyl or similar rings. Attached to it are flexible endgroups, like alkyl or alkoxy chains, that counteract crystallisation. In LC phases formed by calamitics the molecules arrange themselves with their long axis more or less into the same direction, leading to an orientational order found in all of these phases. With decreasing temperature also positional order can occur, even though in liquid crystals it does not reach such an extent as found in crystals. Discotic molecules can form the same phases as calamitic molecules, but they also can pile up into columns, which then can pack into the superstructures of the so-called columnar phases. Besides these two most important mesogen shapes in recent years also other forms were investigated like bent-core, sanidic (brick-like), pyramidal mesogens and many others, which can lead to new, different LC phase structures.

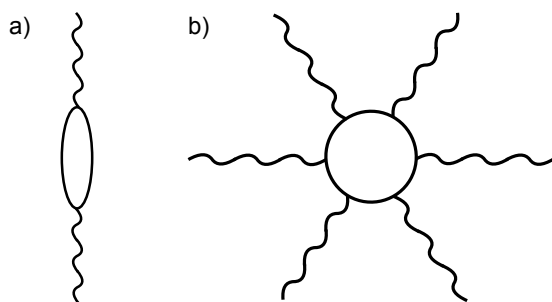


Figure 2.2: Schematic structures of a calamitic (a) and a discotic (b) mesogen, the two most important basic forms of thermotropic liquid crystals.

One of the most important of the anisotropic properties of a LC phase is the optical anisotropy, or birefringence. Beside few examples like the Blue Phase and some rare

other LC phases with cubic symmetry, all phases show birefringence (like “normal” crystals). Therefore one important characterisation method is polarising optical microscopy (POM), which means that a thin sample is observed through crossed polarisers: in the microscope one polariser is set into the light beam to generate linear polarised light which then passes through the sample and is observed after it has passed through the second polariser set with its transmission direction 90° to that of the first one. The birefringence of the LC will generally lead to a change in the polarisation state of the light, the magnitude of the change depending on the sample thickness, orientation of its optic axis, and the strength of its birefringence. For a description of more experimental details, see for example [8] and the references therein. Depending on the present phase, its orientation and the anchoring conditions, characteristic textures and defects can be found in polarising microscopy, which can lead to a (preliminary) designation of phases as explained in the book by Dierking [8] or the classical book by Demus [9]. In the following sections those liquid crystalline phases and characterisation methods that are relevant to this thesis will be described. Finally, in a last section the literature on liquid crystals in confining environment will be reviewed.

2.1.1 The Nematic and Smectic Phases

When cooling a (non-chiral) calamitic material from the isotropic (iso.) phase the first LC phase that can appear is the nematic phase, which is the simplest phase with the least order. The rod-like molecules orient on average with their long-axis along a common direction described by a sign-invariant vector \mathbf{n} , the *director*, as is sketched in fig. 2.3a. Beside this orientational preference no further order exists in this phase, which means that the relative positions of the molecules are still isotropically distributed. The degree of orientational order can be described by an order parameter S which takes into account the spatial and temporal deviation of the molecular long axes from the director with the angle ϕ :

$$S = \frac{1}{2}(3 \langle \cos^2 \phi \rangle - 1) \quad (2.1)$$

In the isotropic phase this parameter becomes 0 as on average all values for ϕ are equally probable, while for a perfect order it becomes 1. Experimentally, as well as from theoretical modelling, in the nematic phase values of 0.3 – 0.4 at the clearing point (the iso. – N transition) and 0.6 – 0.7 as saturation value at lower temperatures are found, the latter corresponding to average values of ϕ in the order of 30° [8]. In the smectic phases that may follow on further cooling (see below) the value for S will only slightly increase further.

When cooling further the next phases that might appear are the smectic phases, in which also positional order occurs, even though not in all three dimensions as in ordinary crystals. They exist in many variations (see the very end of this section), but only the

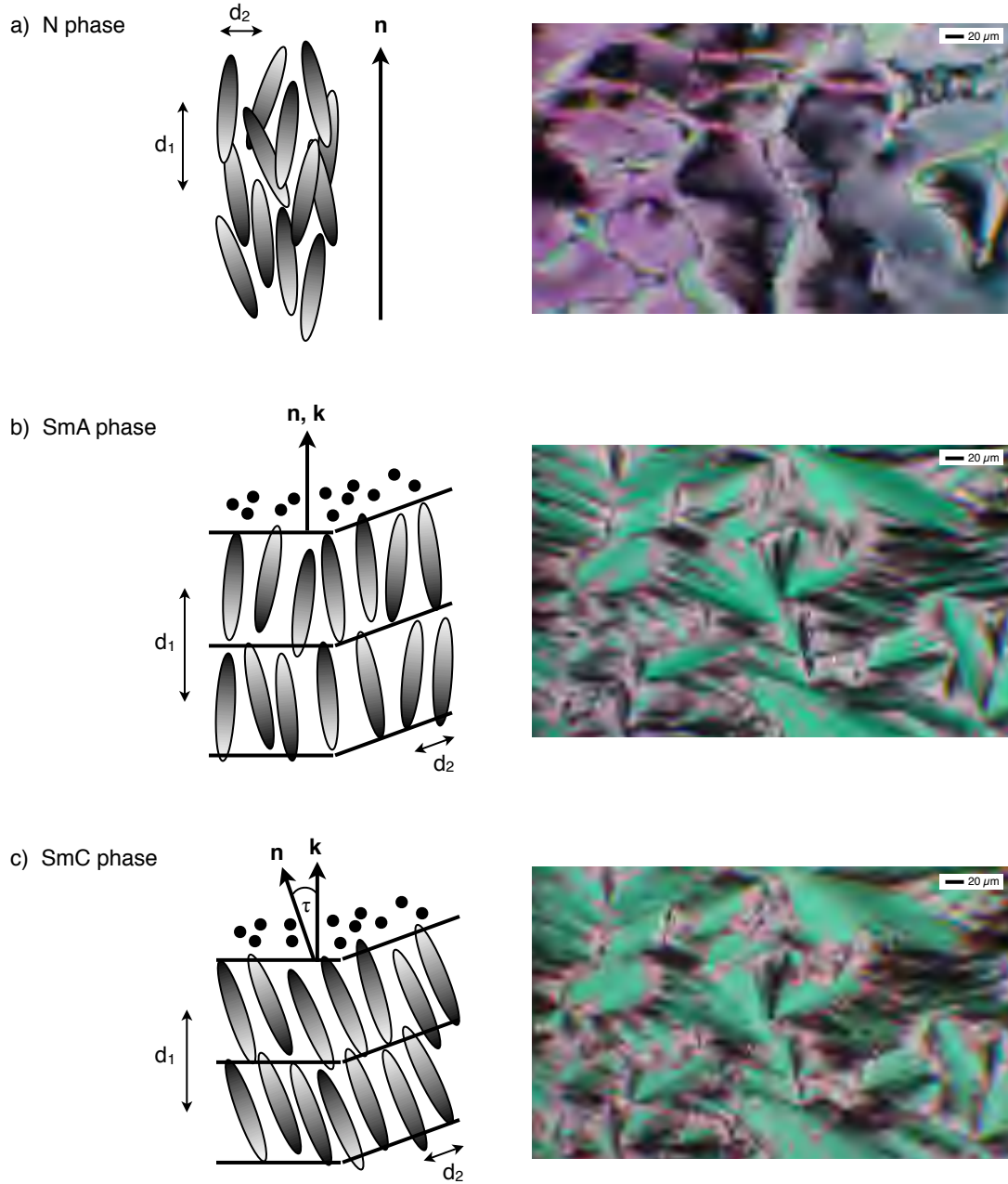


Figure 2.3: Sketch of the molecular arrangement in the nematic, smectic A and smectic C phases and typical textures of these phases in planar alignment observed in polarising microscopy (schlieren texture, fan-shaped texture and broken fan-shaped texture, respectively). Note that the degree of order in these sketches is highly exaggerated (see the discussion on the order parameter).

SmA and SmC phase, which are the most important, are relevant to this thesis. They can be considered as two-dimensional liquids: the molecules now arrange in layers in one dimension, but their positions in the two other dimensions are still isotropically distributed. In the SmA phase the director \mathbf{n} is parallel to the layer normal \mathbf{k} (fig. 2.3b) while in the following SmC phase \mathbf{n} is tilted with respect to \mathbf{k} by an angle τ (fig. 2.3c). When regarding the sketches in this figure one should remember that the order shown there is exaggerated as it only shows an average situation.

As was stated above the optical appearance of a liquid crystal in polarising microscopy depends on the LC phase as well as its orientation towards the incoming light. This can be understood when taking into account that because of the anisotropy of the mesogens the director corresponds also to the optical axis of the system. For example a nematic or smectic A phase with the molecules with their long axis perpendicular to the substrate appears dark between crossed polarisers as it resembles an isotropic liquid when observed in that way. But if the molecules are oriented differently on the substrate or the sample is tilted with respect to the path of the light, coloured textures can be observed. Therefore two important orientations must be distinguished: the just described *homeotropic* orientation and the *planar* orientation in which the molecules lay with their long axis parallel to the substrate. Of course also non-oriented situations are possible depending on the kind and strength of the interactions between the mesogen molecules and the (pre-treated) substrate. So for example a thin, rubbed layer of polymer often induces planar orientation with the director along the rubbing direction, while coating with a surfactant preferably induces homeotropic orientation. Other methods to influence the orientation are the application of an electric or magnetic field. In the right part of fig. 2.3 characteristic examples of textures of the discussed three phases in planar orientation are shown.

Beside these optical investigations the most important technique to study the structures of liquid crystalline phases is X-ray scattering. In the following X-ray scattering on the nematic, SmA and SmC phases will be discussed. The theoretical background of general X-ray diffraction will not be covered as it can be found in basic literature. X-ray scattering on liquid crystals is described for example in the relevant chapter in the Handbook of Liquid Crystals [10]. Again an important issue is if an aligned or an unaligned sample is investigated. In the latter case an average of scattering on domains of different orientation towards the incident beam is detected, like in a powder pattern of crystalline material. Examples of the resulting plots of scattering intensity I as function of scattering angle 2θ are sketched on the left part of fig. 2.4a,b for the nematic and SmA phase, respectively. The information that one can gain from this experiment are the inter-molecular distances along and perpendicular to the molecular long axis, that were designated as d_1 and d_2 in fig. 2.3a,b.

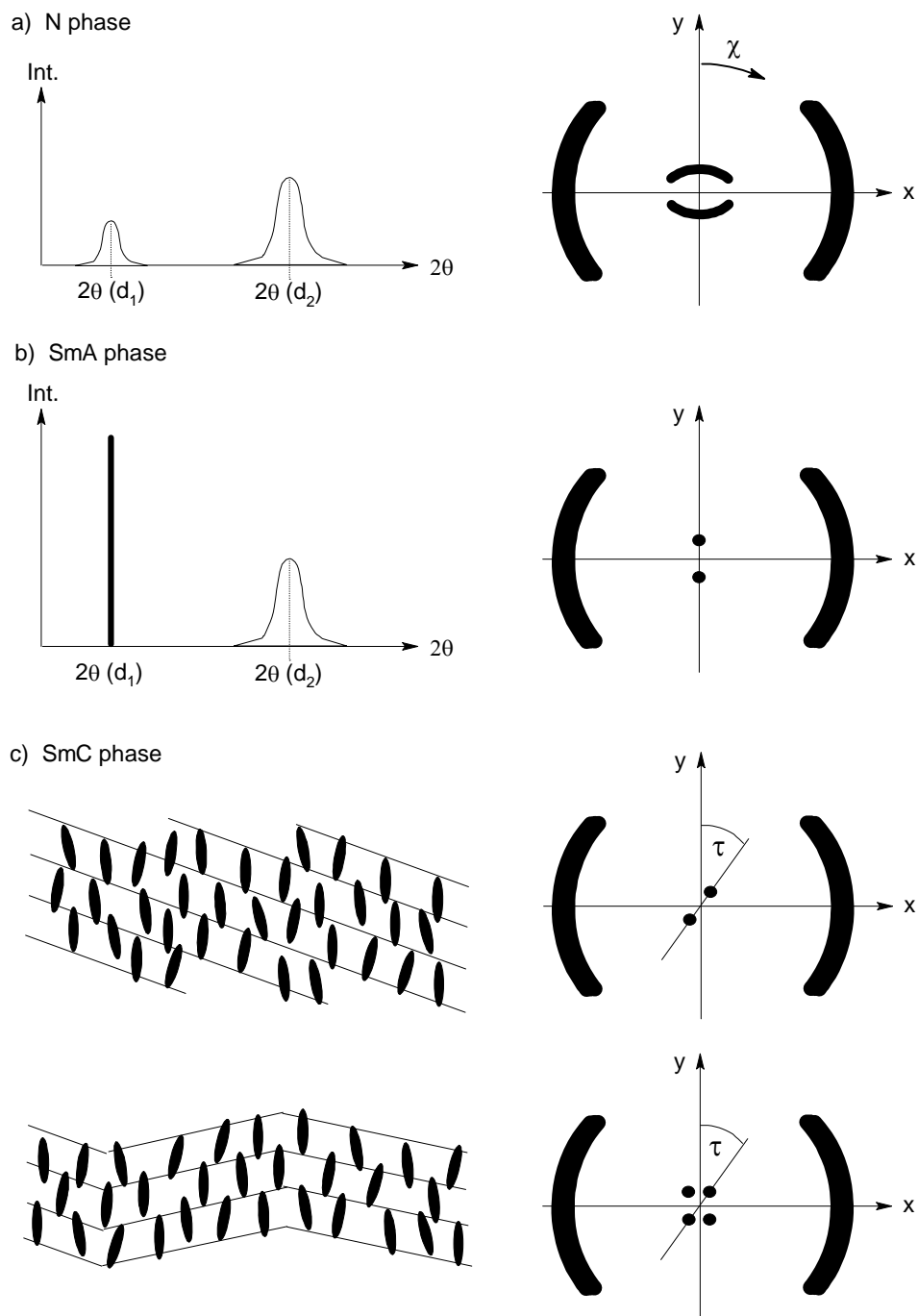


Figure 2.4: Schematic illustration of X-ray diffraction patterns of N, SmA and SmC phases. (a, b) Left side: powder pattern, right side: 2D diffractograms of aligned samples. (c) In the tilted SmC phase two diffraction patterns are possible, depending on the type of arrangement of the smectic layers. Sketches redrawn from [10].

In the nematic phase these two different average distances give rise to two separate diffuse peaks in the regions of small and wide angle diffraction (SAXD and WAXD, respectively), their maxima corresponding approximately to the molecular length and width, respectively. The diffuse appearance results from the short correlation lengths, like also in an isotropic liquid phase. In the SmA, as well as the SmC phase, the wide angle peak stays similar to that of the nematic, while the small angle peak becomes sharp and corresponds now to the layer spacing. But in contrast to true long-range ordered crystalline materials, most smectics exhibit no or only one higher-order peak, revealing the slowly decaying positional correlations.

Even more details are revealed by investigating 2-dimensional X-ray diffraction patterns of aligned samples. Examples for the nematic, SmA and SmC phase are sketched in the right column of fig. 2.4. In these patterns additionally also changes of the scattering intensity along the azimuthal angle χ are observed, giving information on the relative orientation of scattering “layers” in the sample (a powder sample observed with 2D detection would result in circles around the incident beam because of the averaging). As one can see in the sketches for all the discussed phases the wide angle scattering appears as two diffuse and wide arcs centred at the equator. The width along χ shows the imperfect alignment of the molecular long axes along the director. The most significant differences between these phases appear in the small angle region: First, in the less ordered nematic phase again arcs are observed as in the wide angle scattering, which then sharpen into spots in the layered smectic phases. Secondly, in the N and SmA phase the scattering intensity is distributed around the meridian, i. e. the d_1 and d_2 peaks appear along lines that are perpendicular to each other, which changes when entering into the tilted SmC phase.

Now two arrangements of the layers in the sample are possible, resulting in two different patterns as sketched in fig. 2.4c. If the mesogens in all layers tilt in the same direction (upper sketch) the two spots will move away from the meridian, revealing the tilt angle τ (we here assume that the director retains its vertical orientation with respect to the laboratory frame, with the layers effectively appearing tilted away from this direction). If instead the tilting occurs in a chevron-like structure, like sketched in the lower part, four spots will appear, again tilted at τ away from the meridian. Another way to establish the tilt angle is based on the approximation that the SmA layer thickness is identical to the molecular length and that the shrinking of the layer thickness in the SmC phase is only due to molecule tilting. This model can be expressed mathematically by eqn. 2.2, which can be formed to eqn. 2.3 to calculate the tilt angle. But one must take into account that the mentioned assumption on the layer spacings is not fully correct in all cases as for example some LCs show a layer shrinking much smaller than expected when determining the tilt angle by other methods [11].

$$d_{SmC} = d_{SmA} \cos \tau \quad (2.2)$$

$$\tau = \arccos(d_{SmC}/d_{SmA}) \quad (2.3)$$

As already mentioned there are more liquid crystalline phases than those discussed up to now, with more and more degree of order when decreasing the temperature. The next would be the hexatic smectic phases (SmB, SmI, SmF) with short-range positional order in the smectic layer: the molecules form a hexagonal net, but inserted defects prevent long-range in-plane positional ordering. The latter is realised in the soft crystals (B, J, G, E, K, H), which are then finally followed by the generally known, solid crystalline phase. Even though such a variety of phases are possible in an actual LC sample in general only a few of them are realised in one and the same material. A factor not mentioned up to now, but having severe influence on liquid crystalline behaviour, is *chirality* or handedness. As will be described with two examples in the following section, chirality can lead to a change of physical properties, new superstructures in the already known phases and it can even lead to the appearance of new phases [12, 13, 14].

2.1.2 Introduction of Chirality: Cholesteric and Blue Phases

Chirality can in general be introduced into liquid crystals in two ways: by the use of chiral mesogen molecules that build up the LC phase or by adding a chiral dopant to an achiral host phase.[†] To distinguish achiral from chiral phases the latter are marked with a star added to the phase designation, e. g. N* for the chiral nematic phase, a phase that is for historical reasons often also referred to as *cholesteric* phase in recognition of its discovery in cholesteryl benzoate, the substance whose investigation led to the concept of liquid crystallinity [3, 4].

In the N* phase [8, 17] the already introduced nematic order, described again by the director \mathbf{n} as in the achiral phase, is helically modulated along an axis perpendicular to \mathbf{n} as schematically shown in fig. 2.5. Determined by the absolute configuration of the chiral molecules the helix can be left- or right-handed. The pitch length p depends on the strength of the chirality effect and can have values from $\sim 0.1 \mu\text{m}$ to several hundred μm . Furthermore it is influenced by the sample temperature (generally the pitch increases with increasing temperature), in case of mixtures by the exact sample composition and it can adopt to boundary conditions, for example by slightly increasing or decreasing p in order to fill the given space by an integer number of half-pitches. The latter will become important for the discussions on fibres filled with a cholesteric LC in chapter 6.2.

Considering the optical properties of N* liquid crystals the *selective reflection* is their most fascinating facet. For short-pitch cholesterics with p in the range of visible light wavelengths this leads to the appearance of strong, iridescent colours visible directly by

[†]With the recently developed bent-core liquid crystals also the formation of chiral mesophases from achiral molecules was discovered [15, 16]. But one must state that such a phase is only locally chiral and not as a whole sample, as domains of both opposite handednesses are equally present.

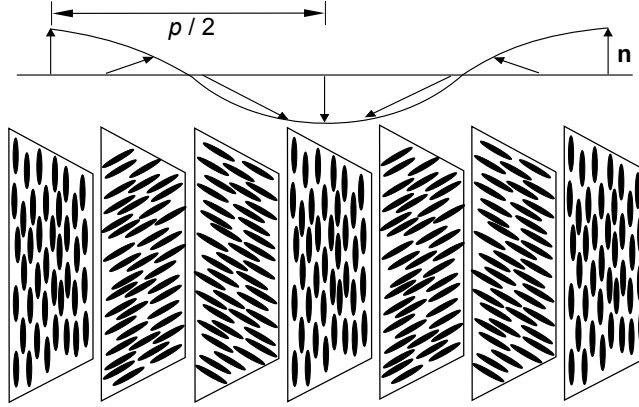


Figure 2.5: Molecular arrangement in a cholesteric phase: the local nematic order, exemplified by the layers sketched in the lower part, is continuously helically modulated along an axis perpendicular to the director \mathbf{n} . The periodicity of the helix is described by the pitch length p .

the naked eye. The reflection can be described similar to a Bragg diffraction according to

$$m \lambda_{refl} = 2 (p/2) \sin \theta \quad (2.4)$$

with m being the diffraction order, λ_{refl} the reflected wavelength in the medium, $p/2$ the optical periodicity and θ the angle of light incidence. The term selective reflection refers to the fact that only a narrow wavelength band defined by $\Delta \lambda_{refl} = p \Delta n$ is reflected, where Δn is the birefringence of a nematic layer perpendicular to the helix axis. The reason for the reflection lies in the periodical helix structure: incoming natural unpolarised light is split up in two oppositely circular-polarised components; from these the component opposite to the helix handedness will be transmitted, while the second component with the same handedness as the helix will be strongly reflected. When illuminating on the other hand with already circularly polarised light it will depend again on the handedness if it will be reflected or transmitted.

Note that with a pitch length below or above the range of visible light in principle the same optical phenomena occur, but the reflected and transmitted light will then be ultraviolet and infrared, respectively, and therefore not visible directly with the naked eye. One should further note from eqn. 2.4 that the visible colour not only varies with pitch length but also with the angle of light incidence, for example when tilting the sample with respect to the incoming light.

Another example of chiral phases are the *Blue Phases* (BP*) that appear only in chiral liquid crystals [8, 18, 19]. Up to three of these rarely occurring phases can exist between the cholesteric and the isotropic phase, but generally only in a small temperature range of about 1 K or smaller. The highest temperature phase BP III*, also referred to

as “fog phase” or “blue fog”, is still not completely understood. Macroscopically it is amorphous and has the same symmetry as the isotropic phase, but its short-range structure is not yet fully established even though several theoretical models have been suggested. In the lower temperature phases BP I* and BP II* the molecules build up *double twist cylinders*, one shown schematically in fig. 2.6a. When moving outward from the central director orientation, the local directors twist more and more up to about 45° as represented by the different colours in the sketch.

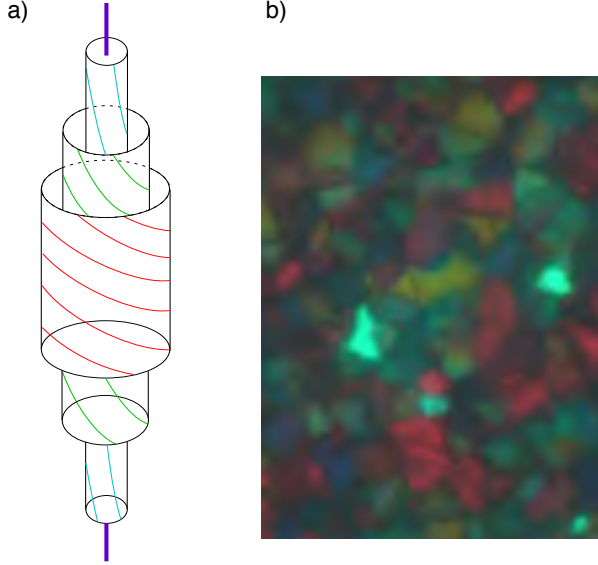


Figure 2.6: a) Schematic sketch of a double twist cylinder, the basic building block of the Blue Phases. The coloured lines represent the local director field at different distances from the centre: in the middle the director is parallel to the cylinder axis and then continuously rotates towards the outside up to an angle of $\approx 45^\circ$. b) Typical multi-coloured platelet texture of the cubic Blue Phases BP I* and BP II*.

These double twist cylinders then arrange into a body centred cubic or simple cubic superstructure, respectively. As this can only be done by at the same time introducing regularly arranged defects at the intersections between the cylinders, these Blue Phases can also be described as a lattice of disclination lines [20]. Because of their amorphous or cubic symmetry all three Blue Phases have, in contrast to ordinary LCs, no linear birefringence and are optically isotropic. They show selective reflection of circularly polarised light, like the chiral nematic phase, but with varying colours as can be seen in the platelet texture in fig. 2.6b. This results from different orientations of each of the small crystallites and therefore of the lattice planes towards the incident light.

Despite the extraordinary properties of Blue Phases, research and potential applications for example in photonics and displays have always been restricted due to their small temperature range. But in recent years several achievements were published on stabilising these phases by several methods. One approach is to add nanoparticles [21, 22] which then partly replace the disclinations and thereby reduce the energy costs of the overall structure [23]. Karatairi et al. [22] found a Blue Phase temperature range of 20 K in this way. Even a larger range of more than 60 K were reported by Kikuchi et al. on embedding Blue Phases into a polymer network [24, 25, 26]. In this case a simi-

lar stabilisation mechanism is predicted as now the polymer chains are concentrated in the disclinations. A further approach is to use new mesogen geometries like T-shaped [27, 28] or bent-shaped [29, 30] molecules. The most successful example for such a new molecular concept are dimeric molecules with high flexoelectricity presented by Coles and Pivnenko [31] that show 40-50 K wide Blue Phases.

2.1.3 A special Case: Liquid Crystal Elastomers

In the following a very different class of liquid crystals compared to the molecules discussed up to now will be described: liquid crystal polymers, with emphasis given to their subclass of elastomers. The following chapter is a summary of the recent review paper by Ohm et al. [32] on this topic. LC polymers consist of polymer chains combined with mesogenic units. As sketched in fig. 2.7 these can be either incorporated directly into the polymer backbone (main-chain polymer) or they are attached through flexible spacer units on the sides of the backbone (side-chain polymer). The latter kind can be further distinguished on whether the mesogen unit is fixed at its end (end-on) or at its middle (side-on).

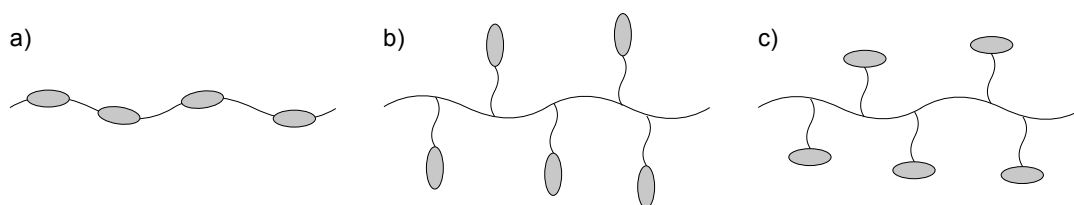


Figure 2.7: The three basic structures of LC polymers: main-chain (a) and side-chain polymers (b, c) with the rod-like mesogen units, represented as small ellipsoids, either incorporated into the polymer backbone (a) or attached end-on (b) or side-on (c) onto it.

In the LC phase (N, SmA, SmC as well as N* and SmC* elastomers have been found up to now) the anisotropy of the mesogen units leads them to become aligned along a common director. Thereby also (parts of) the polymer chain becomes aligned and stretched out along one direction, parallel to the director \mathbf{n} (main-chain and side-on arrangements) or perpendicular to \mathbf{n} (end-on arrangement). When heating above the clearing temperature the polymer chain behaves like common polymers and adopts an isotropic, coiled state (fig. 2.8a). But this deformation has only effects in small domains in the micrometer scale. In order to use this shape change also on the macroscopic scale (fig. 2.8b) two further steps must be taken: first, a monodomain sample must be achieved with the mesogen units aligned uniformly over the whole sample, secondly the chains must be crosslinked to gain a large polymer network.

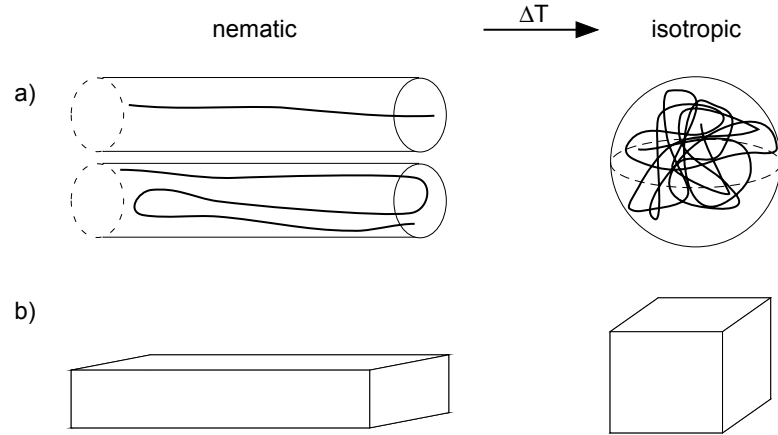


Figure 2.8: Sketches of the microscopic and macroscopic shape changes in a LC elastomer. (a) Conformations of polymer backbones in a main-chain or side-chain side-on elastomer in the nematic and isotropic phase. In the nematic phase they are stretched, leading to a linear or hairpin conformation. In the isotropic phase they transform to a random coil conformation. (b) The resulting macroscopic shape change of a monodomain sample at the transition. Graphic redrawn from [33].

For both steps several methods have been developed that will be introduced briefly in the following. The alignment can be achieved either by techniques acting on the mesogenic units which are therefore similar to techniques known from common liquid crystals: surface forces were applied for example by using alignment layers [34] or by preparing thin, freestanding films [35], nematic phases were aligned in magnetic fields [36], while ferroelectric SmC^* phases could be aligned with the help of electric fields [37]. The other way is to directly deform the polymer chains by mechanical stretching: manually with tweezers [38], by flow alignment in the confined space of a microfluidic system [39], by fibre extrusion / drawing [40], by the electrospinning process [41] or by first synthesising a very weakly crosslinked polymer network, stretch it and then crosslink it further in this state [42, 43]. For the crosslinking process, as well as the general synthesis, many methods have been developed. The crosslinking units can either be incorporated as side groups into the chain during synthesis or afterwards by adding a bi- or multifunctional crosslinking agent to the finished polymer. Several chemical reactions can be used for crosslinking, that will not be covered here, but examples can be found in the mentioned review paper [32] and the references therein. The reactions are initiated on demand by UV irradiation, temperature or by the use of a catalyst.

The gained mechanical properties depend on the quality of alignment in a sample but also on the architecture of the polymer. When the director is parallel to the long axis of the polymer chain the sample contracts in this direction at the clearing transition, if

the director is perpendicular to the polymer chain long axis an expansion results. The first case appears in main-chain-polymers and side-chain-polymers with side-on attached mesogen units. For side-chain-polymers with end-on attached mesogen units both cases are possible, as the chemical linking prefers the director to be perpendicular while geometrical constraints prefer it to be parallel to the polymer backbone. Which tendency is stronger can be influenced by the spacer length. Resulting from these considerations and from measurements on the magnitude of polymer anisotropy one can expect the largest shape change for main-chain-polymers and the smallest for the end-on systems. And indeed the largest shape changes of 400 % were found in main-chain-polymers [40, 44].

2.1.4 Thermodynamic Aspects of LC Phase Transitions

In the last sections several liquid crystalline phases have been described. But from a physical chemist's point of view also the transitions between these phases as well as parameters influencing them, for example the confinement discussed in the next section, are of interest. One of the most common calorimetric methods to study phase transitions is probably differential scanning calorimetry (DSC) as described in detail for example in the books by Haines [45] and Höhne et al. [46].

This method is based on the principle that both the actual sample and a reference material are subjected to a linear temperature scan during which the transition takes place in the sample. A phase transition or chemical reaction that involves heat transfer can then be detected as temperature difference between sample and reference: an endothermic process will lower and an exothermic will increase the temperature of the sample relative to the predefined temperature of the reference. It is therefore of great importance that the reference does not undergo a thermodynamic change of its own in the chosen temperature range. It would also be possible to directly measuring the difference between predefined and actual temperature in a sample without using a reference. But measuring a differential temperature signal has the advantage of greater sensitivity as disturbing thermic effects will act on sample and reference to the same extent and are minimised when calculating the differential signal. Based on these principles three measuring systems can be distinguished:

- *Differential Thermal Analysis*: in this oldest method the measured temperature difference is directly registered as a function of time or predefined temperature.
- *Heat Flux DSC*: the temperature difference is registered as a voltage signal by the electronics of the system. This signal is then calculated into the heat flow difference or other thermodynamic variables.
- *Power Compensation DSC*: Sample and reference are placed in two isolated, but identical chambers, not in a common one as in the two other methods, so that

no heat flow between them is possible. Very small temperature differences are registered and immediately compensated by transferring exactly the needed excess heat q to or from the sample by a second heating system. In this way sample and reference are always maintained at the same temperature. In this case the electrical power P for this compensation is the originally measured signal from which the thermodynamically relevant data is calculated from (see the equations below).

The DSC instrument used in this thesis works according to the last mentioned method. The resulting plot, the *thermogram*, consists usually of either the difference in heat flow \dot{q} or of the heat capacity C_p versus predefined temperature. The relations between the measured power P , \dot{q} , C_p and the enthalpy H can be found in eqn.2.5. The value of \dot{q} , comprises three parts (eqn.2.6): The first term refers to non-avoidable asymmetries of the temperature distribution in the measuring chamber(s). The second term results from the difference in heat capacities of sample and reference that may change in the measured temperature range. These two parts determine the baseline of the thermogram. Finally the third term results from the heat flow due to a phase transition. An example of a thermogram with two transitions is sketched in fig.2.9. For the second sketched transition the transition enthalpy can be calculated from the peak area according to eqn.2.7.

$$\frac{P}{dT/dt} = \frac{dq/dt}{dT/dt} = \frac{\dot{q}}{dT/dt} = \frac{dH}{dT} = C_p \quad (2.5)$$

$$\dot{q}(T, t) = \dot{q}_0(T) + \dot{q}_{c_p}(T) + \dot{q}_{tr}(T, t) \quad (2.6)$$

$$\Delta H = \int_{T_{on}}^{T_{off}} C_p dT \quad (2.7)$$

Note that in most literature all measured values (\dot{q} , C_p and ΔH) are referred to the molar mass of the sample. But as most samples studied in this thesis were many-compound samples with undefined exact composition the values herein were instead referred to the complete mass of the sample. One should additionally be aware that the width and the exact onset temperature of a transition is additionally influenced by the chosen scan rate as the temperature is continuously increased also during the phase transition. To establish these values more exactly it would be necessary to repeat the measurement at different scan rates and then extrapolate the results to zero scan rate. But as the found differences of the onset temperatures are in general quite small (0.5 K range or less) compared to the other effects that should be studied in this thesis this extrapolation was in general not done.

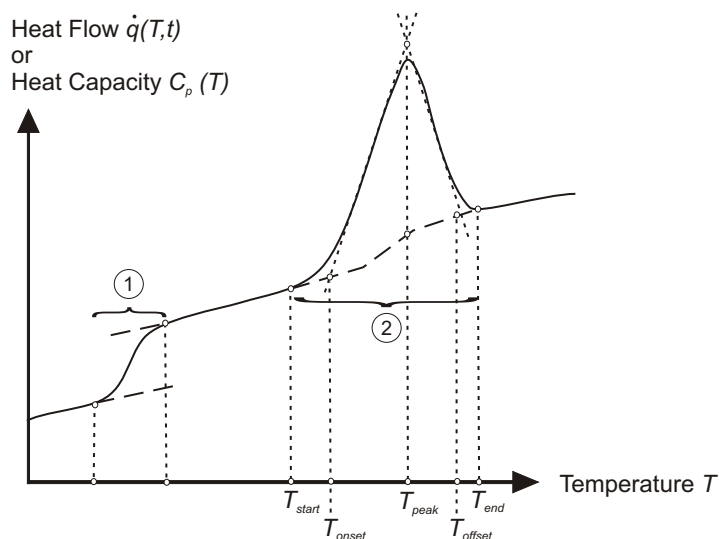


Figure 2.9: Schematic illustration of a DSC thermogram with a second (1) and a first order (2) phase transition (for an explanation see below in the main text) and of important temperatures to evaluate the curve.

The two transitions sketched in fig. 2.9 are presented as two different shapes in the curve: a step and a peak. This results from the different behaviour of the chemical potential at the transition. A classification was first established by Ehrenfest who distinguished first and second order transitions [47]. A first order transition is accompanied by a finite change in volume and enthalpy, in other words a discontinuity of the first derivatives of the chemical potential with respect to temperature and pressure. Therefore the heat capacity C_p theoretically becomes infinite at the transition temperature. The result in practice is a peak measured in the DSC thermogram. In contrast, at a second order transition volume and enthalpy are continuous, but the heat capacity, as the second derivative of the chemical potential, is discontinuous, resulting in the step in the DSC thermogram. This classification was later extended by Landau in two parts. First, by general symmetry considerations and the introduction of the very important concept of an order parameter and secondly by considerations on the thermodynamic properties of the transitions, reflected by the so called Landau expansion of the thermodynamic potential. Table 2.1 briefly summarises his results, for a more detailed description refer for example to [7, 48].

2.1.5 Liquid Crystals in Confinement

Although the first example of liquid crystals confined in electrospun fibres was presented only in 2008 [5], the general issue of confinement effects on liquid crystals is a topic that has received much attention in the research community, and it very much continues to do so today. The most important confining systems that have previously been studied experimentally—and often also theoretically—are the following:

Table 2.1: *Summary of Landau rules on first and second order phase transitions [48]*

First order transition	Second order transition
Symmetry may change or may not (no symmetry relation).	Symmetry <i>must</i> change. The transition state has to include all symmetry elements of <i>both</i> phases (symmetry relation).
Transition point: Both phases <i>coexist</i> with phase boundaries between; superheating and supercooling possible.	Transition point: Both “phases” represent the <i>same state of matter</i> (e.g. SmC with zero tilt can not be distinguished from SmA). No phase boundaries; superheating and supercooling impossible.
Order parameter varies <i>discontinuously</i> with temperature.	Order parameter varies <i>continuously</i> with temperature.

- *Planar plate confinement*

The standard configuration for studying and applying liquid crystals, the liquid crystal most often being confined between parallel glass plates. For studying confinement effects specifically it can however be advantageous to use wedge cells [49, 50, 51], imposing a varying degree of confinement to one and the same sample. While it is easy to control and vary the surface anchoring conditions, the main drawback of this sample geometry is that the minimum plate distance that can be practically achieved with any kind of precision is on the order of several hundreds of nanometers, more often a few microns.

- *Glass capillaries*

The simplest way of studying cylindrical confinement is to fill the liquid crystal in a standard glass capillary. Surface anchoring can relatively easily be switched between planar and homeotropic by using different inside coatings, although a specific planar alignment direction (e.g. along or perpendicular to the capillary axis) is challenging to achieve. Since glass capillaries are generally relatively thick, the strongest confinement studied using glass capillaries is on the order of tens of microns [52], thus comparatively weak confinement.

- *Anopore and Nucleopore / Millipore membranes*

Two systems providing cylindrical confinement in inorganic and organic matrices, respectively, are Anopore (aluminium oxide, most common pore diameter 200 nm, length 60 μm [53]) and Nucleopore (plastic, typically polycarbonate, pore diameter

in the range $0.1 - 20 \mu\text{m}$, length $10 \mu\text{m}$ [53, 54]) membranes (Millipore membranes belong to the same membrane category). Both were developed for filtration purposes but many liquid crystal researchers have filled the pores with liquid nematics or smectics to study the effects of confinement on these phases. The raw surface of Nucleopore / Millipore membranes has been reported not to enforce any preferred local molecular alignment [55], while that of Anopore should impose planar axial alignment [56]. In both cases the pore insides can however be coated with selected materials, ensuring either planar or homeotropic surface anchoring [53].

- *Aerogels and aerosils*

Another popular approach to study liquid crystal confinement effects is to use aerogels or aerosils for ensuring the confinement. These materials are formed by gelation of nanoparticles, resulting in pores that curve strongly in random ways, imposing a *disordering* influence on the liquid crystal. Aerogels are formed by letting 3 to 5 nm diameter silica particles in solution fuse into fractal clusters, forming an inorganic network that is stabilised by covalent bonds. The result is a rigid highly porous structure with silica volume fraction down to 0.05 and a typical cavity dimension in the range 10 to 100 nm [57]. Aerosils, in contrast, are prepared by dispersing silica nanoparticles in the liquid crystal and then allowing gelation to occur. The random silica network that forms is rather loosely kept together through interparticle hydrogen bonds, and it may thus break up and rearrange on moderate time scales to relieve strains imposed by the hosted liquid crystal provided that the silica concentration is not too high (at silica nanoparticle mass fractions beyond 0.1 g/cm^3 also aerosils were considered to behave rigidly) [55].

- *Vycor and Controlled-Pore Glass (CPG)*

These commercial porous glass types are similar to aerogels in that they also are random porous 3D-interconnected SiO_2 networks, albeit produced via different routes. A variety of types exist but as two examples, one study of liquid crystals confined in vycor glass was done on a sample with a mean pore diameter of about 7 nm and an average pore length of some 30 nm [58] and a study with a CPG matrix had pore diameters in the range 15 – 300 nm [59]. The nontreated silica surface yields degenerate planar surface anchoring of the director (however, steric effects promote alignment along the channel long axis) but treatment with silane enforces a homeotropic anchoring [59].

- *Ordered porous alumina templates*

Similar to Anopore, these templates provide confinement in parallel non-connected straight cylinders, but the pores are highly regularly arranged. Steinhart and co-workers studied the alignment of discotic liquid crystals in ordered porous alumina templates with pore diameters of 400 and 60 nm, respectively, and a pore length

of $100\text{ }\mu\text{m}$, either directly [60] or after first coating the pore walls with a layer of poly(methyl methacrylate) [61].

For this thesis the most interesting studies are obviously those of calamitic liquid crystals confined by surfaces imposing planar alignment, since herein calamitic mesogens were studied and since planar anchoring was found in all fibres. Moreover, the disordering effect of random porous structures is not expected in the case of electrospun fibres, providing confinement in cylinders of quasi-infinite extension (disregarding the undesired case of highly beaded fibres). The following brief review is thus restricted to liquid crystals from rod-shaped mesogens confined in straight cylinders or between flat plates, providing planar surface anchoring.

Planar plate confinement

In the simplest case the liquid crystal was confined between flat glass substrates in thin sample cells [49, 50, 51, 62, 63, 64] or such a situation was theoretically investigated [65, 66, 67]. These studies show that even the relatively weak confinement resulting from parallel plates with a spacing in the micron range can dramatically change the phase sequence of chiral smectic liquid crystals [50, 51, 62] and/or it can stabilise structures different from the bulk structure, as in the case of surface-stabilised ferroelectric liquid crystals [63] where the helix is expelled by means of confinement. This effect is at the basis of most research and applications of ferroelectric and antiferroelectric liquid crystals.

Due to the technical difficulties in realising planar cells with substrate spacing on the nanometer scale such a situation has rarely been studied experimentally but via simulations a liquid crystal with isotropic-nematic-smectic sequence in bulk was studied for the case of a flat slab as thin as 8 nm [65]. This revealed strong impact from the surfaces on the phase sequence, with an increased degree of order, both orientational and translational, at temperatures corresponding to nematic and isotropic in bulk. At lower temperatures, where the bulk sample turns smectic, this very strongly confined sample however exhibits a lower degree of order (of both types) than in bulk, according to the simulation. In another simulation work [66] the structure of a twisted nematic cell was investigated as the substrate spacing was reduced towards zero, revealing a dramatic change upon reducing the spacing to some ten molecular lengths (about 30 nm), again a spacing which is challenging to realise in practice with standard cells.

Confinement in straight cylinders

Nanoscale confinement is much easier to realise experimentally in cylindrical geometry, e.g. in Anopore or Nucleopore membranes. This is also obviously the most relevant geometry for the present study of liquid crystal-containing electrospun fibres, where

cylindrical confinement is the ideal case. Many previous studies of cylindrical confinement are however restricted to extremely small diameters, on the orders of some tens of nanometers up to 100 or 200 nm, whereas our electrospun fibres often have inner diameters about an order of magnitude larger, hence the results may not be directly comparable.

The effects found in liquid crystals confined in cylindrical pore membranes that are most relevant for this thesis are the following:

- *Isotropic-nematic transition changes from distinct first-order to gradual.*

Nuclear Magnetic Resonance (NMR) studies of the isotropic-nematic transition inside the 200 nm cylindrical pores of Anopore membranes indicated the presence of a surface-induced orientational order at temperatures well above the bulk isotropic-nematic transition temperature [68]. As a result the sharp first-order character of the isotropic-nematic transition characteristic of bulk liquid crystals disappeared and was replaced by a continuous ordering transition. Soon afterwards calorimetry investigations of the same system partially corroborated this conclusion, revealing suppression and broadening of the transition peak [69, 70]. However, the phase transition could still be resolved and it was in fact shifted to lower temperatures in the confined system. Recently computer simulations of the phase transition in very thin cylinders (diameter on the order of 10 nm) also suggested a change from discontinuous to gradual orientational transition [71].

- *Planar longitudinal alignment is preferred.*

Even with some surface coatings that provide homeotropic alignment in thicker samples, confinement in 200 nm Anopore cylinder pores resulted in planar alignment along the cylinder axis [68]. This suggests that the elastic energies in sub-micrometer channels can overwhelm surface anchoring effects if these are not very strong, the 'winning' alignment being with the director along the channel as this leads to a defect- and distortion-free director configuration.

- *Nematic-smectic transition is inhibited.*

Calorimetry studies of 8CB in 200 nm cylinder pore Anopore membranes revealed a dramatic confinement-induced suppression of the specific heat of the N – SmA transition, together with a slight shift to lower temperatures [69, 70]. Simulations of a liquid crystal confined in very thin cylindrical pores (diameter about 10 nm) with planar surface anchoring suggested that positional ordering was strongly inhibited, counteracting a transition from a nematic to a smectic phase [71].

2.2 The Electrospinning Process

Electrospinning or electrostatic spinning as a technique to produce fibres of micro- down to nanometer scale in diameter has gained increasing interest in the last 10 – 20 years. Reasons are the quite simple, laboratory scale, basic setup, the wide variety of polymers that can be used and also the range of fibre architectures accessible, like e.g. smooth, porous, core-sheath and hollow fibres. This has also given the ideas to many possible applications like filters, nanofibre-reinforced composites, “smart” textiles, sensors, optoelectronics devices, nanofibres as support for catalysts and also medical applications like drug delivery, wound healing and scaffolds for tissue engineering. The topic has since then been widely reviewed in the literature for example in [72, 73, 74, 75, 76, 77, 78] that were used as the main information source for the following part.

2.2.1 Fundamental Principles

A very basic setup for electrospinning is sketched in fig. 2.10. Its main components are:

- a viscous polymer solution or melt that is slowly pumped at a constant rate [‡]
- an electrode that is in contact with the solution (e.g. in form of a metallic tube or needle through which the solution is led or in form of a metal wire inserted into the solution)
- a grounded or oppositely charged collector on which the fibres will be deposited (in the simplest case a piece of aluminium foil) at a distance between 5 and 30 cm below the orifice out of which the solution is spun
- a high-voltage power supply connected to electrode and collector that creates an electric voltage of 1 to 30 kV between them

When a drop of polymer solution is hanging from the orifice of the metallic tube, also referred to as the spinneret, and a high enough voltage is applied the electrostatic forces acting on the solution will lead to the initiation of a highly charged fluid jet that is continuously accelerated and elongated on its way to the collector. As the surface is also increased rapidly in this process the solvent can evaporate very easily and the jet will solidify as a thin fibre on the collector. The actual properties of the resulting fibres, especially their diameter and morphology, can be fine-tuned by varying one or several of the many, sometimes correlated processing parameters. These can be related to either the polymer solution like for example surface tension and viscosity with their opposing effects or operational conditions like the strength of the applied electric field and finally

[‡]The technique of melt electrospinning will not be further explained as it was not used in this thesis. It is generally based on the same principles as electrospinning of a polymer solution explained herein.

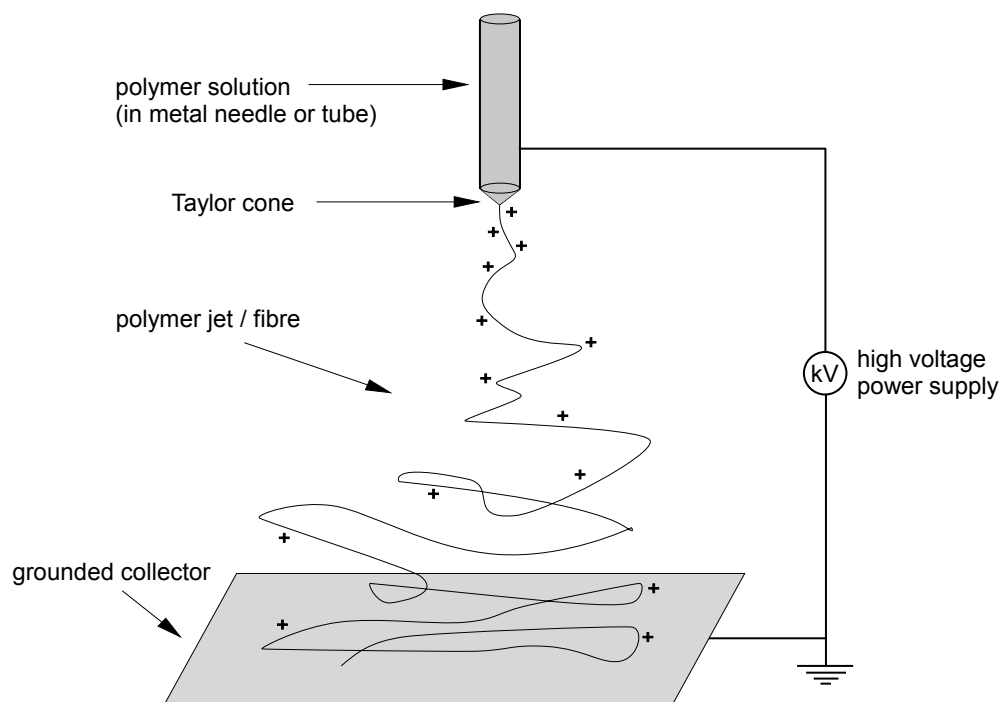


Figure 2.10: Schematic illustration of the basic setup for electrospinning and of the fibre formation.

also environmental conditions can play a role. The effects of the most important factors will be explained in detail in the next chapter.

But first, a more detailed description of the electrospinning process itself will follow. For this purpose, as for theoretical investigations, the overall process is generally divided into several stages: Charging of the solution, Taylor cone formation and launching of the polymer jet, thinning of the straight jet or electrospray, whipping instability and finally solidification into a fibre. For the following discussion one should keep in mind that electrospinning is a complex electrohydrodynamic process which is determined mainly by the interplay of the surface tension of the polymer solution on the one hand and by the electrostatic forces of the applied electric field and of the (induced) surface charges in the solution on the other hand.

As a first step necessary for electrospinning to happen charging of the solution must occur. This can be explained with two, maybe coexisting models. According to the first [77, 78], excess charges are introduced in the polymer solution that remove the electrical neutrality of the overall solution. These are formed in the contact zone between fluid and electrode when the electric field is turned on. Depending on the polarity of the

applied field either electrons are withdrawn or moving into the solution, leading to the formation of either cationic or anionic species. Which molecules of the fluid actually get charged depends on their nature and also on present impurities that can be charged as well. Because of the electrostatic force and by diffusion the ions then move to the surface of a drop hanging from the orifice of the spinneret, and distribute themselves evenly over this surface to reduce repulsive interactions between them.

In contrast, in the second model [76] the overall solution stays electrically neutral and instead a charge separation takes place. This should hold especially when the solution itself is conductive, for example when it contains ions already at the start. As the positive and negative ions can be separated and can move independently from each other at different velocities when the voltage is turned on, they will either move towards the drop surface or towards the electrode wall, respectively, depending on the polarity of the field. This explains why the addition of an ionic compound can help to improve the produced fibres as the resulting higher conductivity increases the effect of electrostatic forces in comparison to the generally less affected surface tension.

By increasing the applied voltage further the electric field strength between spinneret and collector increases as well, leading to an attracting force on the charges in the solution towards the collector. At the same time the higher voltage leads to an increased charge density in the drop and thereby also of the repellant forces between the like charges. As a result the drop deforms from spherical to conical (compare fig. 2.11a and b), a shape referred to as Taylor cone. It can be explained as a compromise shape between the surface tension preferring a drop shape to minimise the surface area and the electrical forces pointing towards the collector.

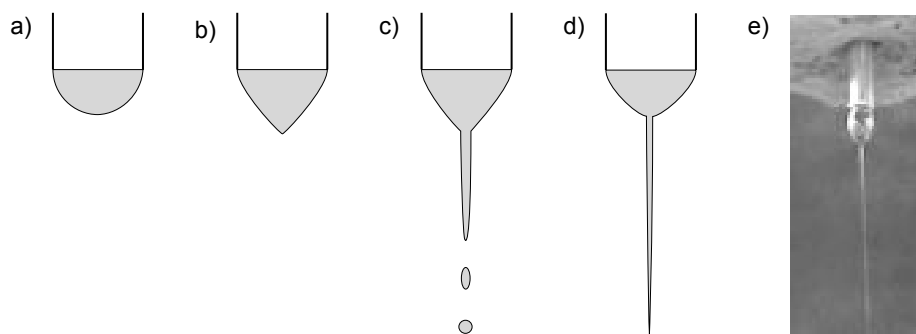


Figure 2.11: *Behaviour of a polymer solution at increasing electric field. a) A drop of solution with no voltage applied. b) As the voltage is applied the drop deforms to a Taylor cone. c) Above a certain threshold voltage a fluid jet is ejected. d) Steady state: equal amounts of fluid are transported to and away from the drop. e) Photograph of an actual drop with ejected filament.*

Above a certain threshold voltage the surface tension can be overcome and additional surface area for the increased amount of charges is created by shooting out a fluid jet

from the tip of the cone that is barely visible with the naked eye (cf. fig. 2.11c,e). Usually at the beginning of the electrospinning process one goes through a short regime with alternating jetting and dripping as the electric field is not strong enough to transport away all new incoming fluid before it falls down because of gravitation. But by carefully adapting the voltage and the flow rate a steady state between fluid transported to and away from the drop can be established. This leads finally to a continuous jet and the shape of the drop relaxes back to a more spherical shape (cf. fig. 2.11d).

As a result of the attracting electrostatic force the fluid jet follows initially a straight path towards the collector, while it is strongly accelerated with up to 600 ms^{-2} , making gravitational forces in comparison negligible [75]. The repulsion between the like charges in the jet, enhanced by solvent evaporation which reduces the distance between them, leads to an increase in surface area, which is realised by a drastic stretching and consequent reduction of jet diameter. Opposing to this effect, the surface tension still promotes a reduction in the surface area, favouring a droplet shape. This Rayleigh instability is generally prevented in electrospinning because of the viscoelasticity of the solution containing long, entangled polymer chains. But for fluids of low molecular mass compounds the Rayleigh instability leads to a break-up into single, like-charged droplets. If the solvent is then evaporated, the increasing charge density causes these droplets to further explode into even smaller droplets, an effect known as *electrospraying* which is made use of in electrospray ionisation for mass spectrometry. In electrospinning nevertheless conditions of strong surface tension in comparison to the opposing effects can result in fibres with a “pearls on a string” or “beaded” morphology.

After a short, straight path the jet is affected by further instabilities, a result of small effects like lateral fluctuations and inhomogenities in charge distribution, as schematically sketched in fig. 2.12. The axisymmetric instability (b), leading to bead formation, and the splitting instability (c), that can lead to a break up of the fluid jet into two parts, are less common, but the bending or whipping instability (d,e) is maybe the most important part of the electrospinning process, as it leads to a dramatic further decrease of fibre diameter that cannot be reached by common fibre drawing processes.

The bending can be explained by considering that as soon as a slight lateral fluctuation acts on one of the like charges in the fibre, an electrostatic force F_{res} is generated that points outward and amplifies the fluctuation (compare fig. 2.12a and d). Therefore the straight path is deformed into a spiral with increasing diameter, that can even undergo further bending instabilities leading to the formation of ever smaller spirals overlaid on the previous ones [79]. This gives rise to a complex, three-dimensional coiling jet path, a simplified sketch is given in fig. 2.12e. The path is often also represented as to take place in a cone between the spinneret and the collector with a typical radius of about 10 – 15 cm at its lower end [75].

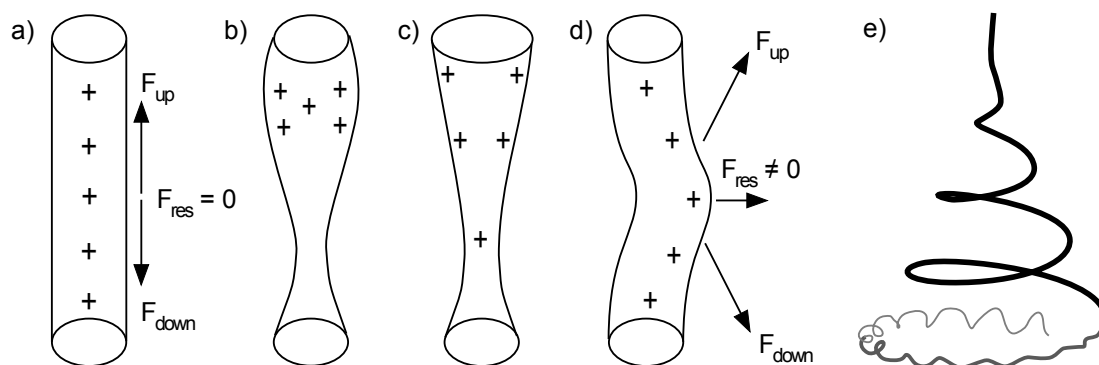


Figure 2.12: (a – d) Sketches of charge distributions in a fluid jet that can lead to instabilities: ideal, straight jet without instability (a), axisymmetric instability (b), splitting instability (c) and bending or whipping instability (d), redrawn according to [77, 78]. (e) Simplified sketch of a possible jet path with a straight segment in the beginning which then transforms into a spiral with the onset of bending instability. The grey part represents a region with a superimposed second bending instability. Redrawn from [78].

At the deposition point the jet has reached velocities of 40 ms^{-1} or more [74], a strain rate on the order of 10^5 s^{-1} has been applied [79] and the cross section of the jet is reduced by a factor of 10^5 [79] which also corresponds to a large increase of jet length. When all solvent has been evaporated until this point a solid fibre reaches the collector, where it gets discharged. Because of the extreme strain rates, the polymer molecules tend to become elongated along the fibre axis, which can be proved by birefringence visible in polarising microscopy or by investigating them with X-ray diffraction. Finally it should be mentioned, that as a result of the coiling motion the fibres are in general deposited as a random nonwoven mat. By the use of more sophisticated collector designs this can be altered and aligned fibre mats or single fibres can be deposited in a controlled way. This will be dealt with in more detail in chapter 2.2.3.

2.2.2 Factors affecting the Fibre Morphology

As already stated the properties of the resulting fibres depend on many factors which can be divided into three kinds: properties of the polymer solution, operational parameters and environmental conditions. In the following the most important of these factors and their effects will be explained as was found in the literature on electrospinning experiments. A summary of the found trends is shown in fig. 2.13. For fibres made with the polymer poly(vinyl pyrrolidone) (PVP) electrospinning conditions were investigated extensively in the papers by Yang et al. [80], Chuangchote et al. [81] and Munir et al. [82]. Theoretical models and their predictions, most importantly studied by Rutledge, Reneker and Yarin, will not be dealt with as they are beyond the scope of this thesis.

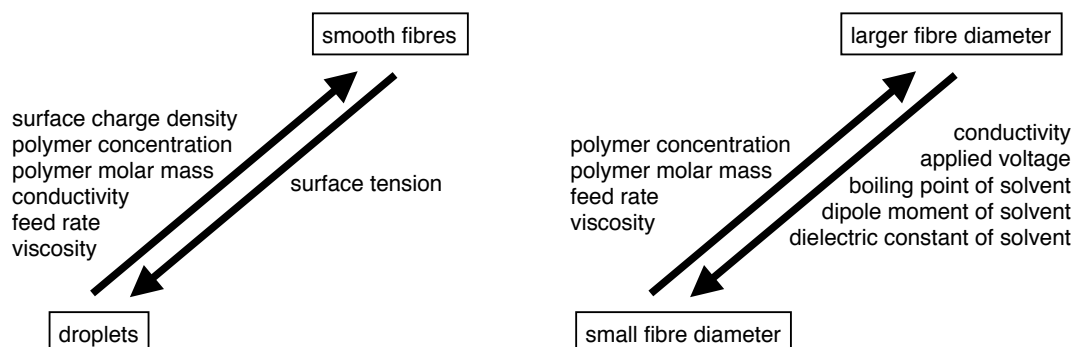


Figure 2.13: Influence of processing parameters on the two most important morphological aspects of electrospun fibres: transformation between droplets, pearls-on-a-string structures and uniform, smooth fibres and the diameter of the resulting fibres.

Polymer properties and the importance of entanglement

It was already mentioned in the previous chapter that a solution containing only low molecular mass compounds leads to electrospraying rather than electrospinning when a high enough electric field is applied. For electrospinning to occur the solution must have a high enough viscosity (see below) to oppose the Rayleigh instability and there must be enough entanglements between the polymer chains. The latter is mainly related to the molar mass and the concentration c of the polymer, but also a flexible, linear, chain-like conformation is necessary, which depends on the interaction between solvent and polymer [83], on the solution temperature [84] and by the chemical nature of the polymer [85]. In this thesis mainly PVP with a very high molar mass was used as polymer, but when using poly(vinyl alcohol) (PVA) or an LC elastomer instead it was difficult to electrospin them, a result that we explain by the relatively low molar masses of the samples used. Therefore and as this aspect is ignored in many studies it shall be explained here in more detail, based on the description in the book by Andradý [76].

In polymer studies generally three concentration regimes are distinguished for a polymer solution: in the dilute solution the polymer chains have a coiled conformation and do not interact each other, in the semi-dilute regime the chains start to overlap even though their volume fraction in the solution is still low, and finally in the concentrated regime the chains are so dense that they topologically constrain each other. These regimes are labelled I to III in fig. 2.14a, the transition concentrations are c^* and c^{**} , respectively. If the molar mass of the polymer is high enough, the semi-dilute as well as the concentrated regime undergo a further transition at the critical entanglement concentration c_e from unentangled to entangled semi-dilute or concentrated, respectively (labelled IV and V in fig. 2.14a). The values for c^* , c^{**} and c_e can be determined from rheological measure-

ments as the slopes of a diagram of viscosity as function of concentration changes at these points, but also a calculation from other polymer properties is possible.

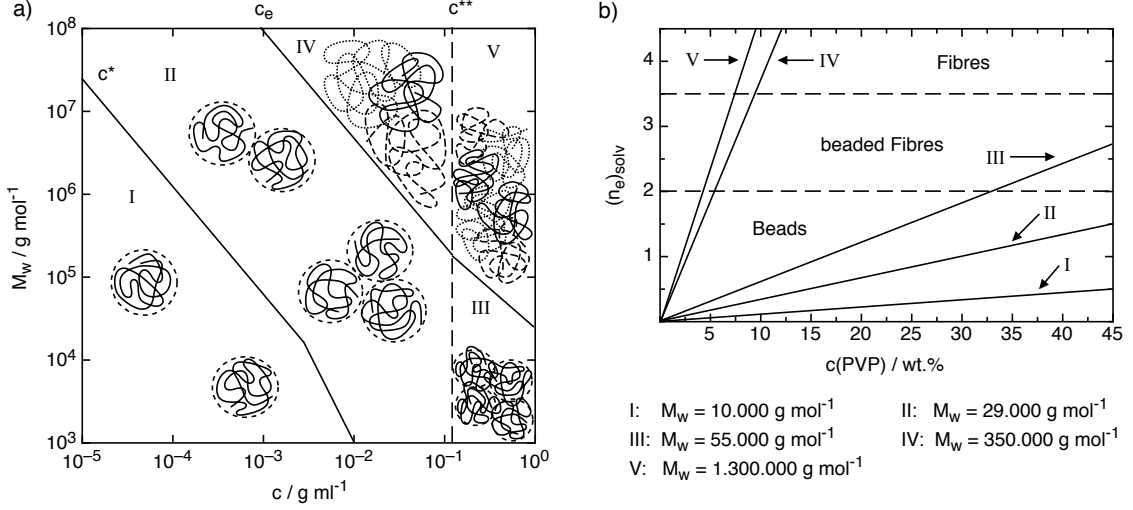


Figure 2.14: a) The five regimes of a polymer solution as function of concentration and molar mass including schematic drawings of the behaviour of the polymer chains. I: dilute, II: semidilute, III: concentrated, IV: semidilute-entangled, V: concentrated-entangled. b) Plot of calculated entanglement numbers as a function of concentration and molar mass for PVP in ethanol and its influence on electrospinning results. Numerical values as calculated in [82] (I-IV) and [86] (V), respectively.

Ignoring other effects it is found that electrospinning only occurs in the semi-dilute entangled and concentrated entangled regimes and, as discussed in [76], the best results in the sense of non-beaded, long fibres should be expected for the latter regime. Following the description above, one method to assure that one of these regimes is used for an electrospinning experiment, is to determine a diagram like in fig. 2.14a for the used polymer-solvent combination or at least the values for c^* and c_e , see for example [87, 88, 89]. Note that instead of these values also sometimes the Simha-Frisch parameter $[\eta]c$ is given, where $[\eta]$ is the intrinsic viscosity. If $1 < [\eta]c < 10$ the solution is in the semi-dilute regime, below and above in the dilute or concentrated regime, respectively, but there is no measure if there are also enough entanglements.

A different approach to predict the electrospinnability is the solution entanglement number $(n_e)_{solv} = \phi_p M_w / M_e$ developed by Shenoy et al. [86]. Herein M_w is the molar mass, ϕ_p the volume fraction of the polymer in solution and M_e the average molar mass between entanglement couples in the polymer as melt. Values for M_e can be found for many polymers in the literature but they can also be calculated from other polymer properties [90]. They could show for several polymers that if $(n_e)_{solv} \lesssim 2$ only droplets,

for $2 \lesssim (n_e)_{\text{sol}} \lesssim 3.5$ short, beaded fibres appear and for $(n_e)_{\text{sol}} \gtrsim 3.5$ smooth fibres are observed in electrospinning experiments. For PVP of different molar mass a plot of calculated values of $(n_e)_{\text{sol}}$ as a function of concentration is shown in fig. 2.14b. For the highest molar masses a good agreement between prediction and experiments was found [82, 86], while for the three lowest molar masses Munir et al. found the transitions shifted to lower concentrations than expected which they explain by solidification of the still very high concentrated solutions before the Rayleigh instability can lead to bead formation [82].

To summarise, both approaches can give a first approximation which molar mass and concentration a polymer in a solution should at least have for electrospinning to be possible, even though the transition is generally not as sharp as suggested by the diagrams. Also, as mentioned above other factors can play a major role leading to severe deviations from the expected behaviour, see for example [89]. Furthermore one has to keep in mind that changes in molar mass and / or concentration also change the viscosity of the system, which largely affects the electrospinning results [81, 91]. On the other hand, when adapting the concentration to the same viscosities for different molar masses, fibres with the same morphology and the same range of diameters were found [81].

Solution properties

One of the most important properties with regard to electrospinning is the **viscosity** of the solution. For electrospinning to occur at all, a minimum viscosity is necessary whose value depends on the chosen polymer. As the viscoelasticity of the solution helps to oppose the Rayleigh instability increasing the viscosity leads to a transformation from droplets to beaded fibres to finally smooth fibres and as the viscoelastic force also opposes the rapid thinning of an electrospun jet, the diameter of the resulting fibres increases with increasing viscosity. These phenomena were for example studied for PVP and several polymers in [72, 80, 81, 82, 88, 92, 93, 94]. As furthermore shown in these papers the viscosity is proportional to the **polymer concentration**. Also the choice of solvent influences the viscosity, but to a much minor extent [80, 81, 95]. At very high concentrations / viscosities electrospinning will become difficult again as the solution can get too viscous to be pumped at a steady flow rate and also the droplet on the spinneret and/or the jet ejected from it are more affected by gravity than by electrostatic forces.

The **surface tension** of the polymer solution affects the occurrence of beads or smooth fibres, but unlike the viscosity has no effect on the fibre diameter. Its value is mainly determined by the used solvent(s) [80, 81, 95] and to a minor extent by the polymer concentration [94, 95, 96]. If the surface tension of the used solution is too high and beading shall be avoided, the addition of a small amount of non-ionic surfactant

can drastically lower it yielding smooth fibres as well as an reduction of the minimum voltage needed for electrospinning to occur [97, 98].

As an electrohydrodynamic process electrospinning is also affected by solution properties that make them influenced by electric fields. The most important are the **conductivity** and the **(surface) charge density**. Both depend on the chosen solvent and on the presence of ionic impurities as well as purposely used additives, e.g. inorganic salts [72, 92, 99] or ionic organic compounds [83, 100, 101]. A minimum conductivity is necessary for electrospinning to occur [76], but there can be also an upper limit reached where the Taylor cone becomes unstable [102]. In between a higher conductivity and / or higher charge density leads to a decrease in fibre diameter and and to a reduction or even complete prevention of beading. Both effects can be traced back to an higher influence of the electrostatic forces on the solution so that the thinning whipping instability is favoured while the Rayleigh instability is disfavoured [95]. When comparing solvents of similar other properties also the **dielectric constant** and the **dipole moment** can play a role. In both cases an increase was found to lead to a reduction in fibre diameter [80, 81, 83, 103].

Solvent evaporation during the very short time in which the charged jet travels from the spinneret to the collector is an necessary issue to gain stable fibres. Therefore the **solvent volatility** was found to be responsible for different fibre outer morphologies. The most obvious effect is that if not all solvent is evaporated the fibres fuse on the collector. If on the other hand the solvent is too volatile this can lead to an inhomogenous drying of the jet: the outer surface already forms a dry, solid “skin” while in the “core” the solvent is still present. When the remaining solvent finally has evaporated through the outer layer the volume of the “core” is decreased drastically with respect to the “skin” which in its solid state could not adapt any more to this change. This leaves an almost hollow tube which can collapse into ribbons [104] or wrinkled “raisin-like” structures [105].

Operational parameters

The applied **flow rate** of the polymer solution should ideally match the rate of removal from the spinneret. A too low flow rate leads to an intermittent or even depleted Taylor cone while a too high flow rate leads to fused fibres or even to dripping as the increased volume can not be transported away fast enough. But in a small range the flow rate can be adjusted: a lower flow rate decreases the diameter of the resulting fibres as well as of eventually present beads, however the number of beads might be increased [82, 92, 106]. The equilibrium between solution transported to and from the spinneret also depends on the strength of the **electric field** as was shown for example by Reneker and Yarin [78]: at a constant flow rate only in a certain range of applied voltage stable electrospinning

could be achieved, below dripping occurred while above the Taylor cone became unstable as the droplet got smaller and finally was depleted, see also [94, 107].

Within the **voltage** range where electrospinning takes place increasing the voltage can help to avoid beading and to decrease the fibre diameter until a certain value, even though sometimes with a broader diameter distribution [106, 107]. But in some cases it was also found that the diameter oscillated with voltage: first, an increase leads to a decrease in diameter up to a certain minimum, at increasing the voltages further the diameter increases again but not to a value as high as for the lowest voltage, and for even higher voltages it decreases again [81, 108]. Note that according to [81] this effect also depends to some extent on the polymer concentrations as it becomes negligible for low polymer concentrations. The explanation generally given for this oscillating behaviour is as follows. A higher voltage leads to higher charge density followed by an increase of the electrostatic force attracting the jet to the collector as well as the of repulsive Coulomb force between the like charges in the jet. The two forces have contradicting effects with respect to this problem: the Coulomb force causes a stronger stretching effect and therefore a smaller fibre diameter as observed for minor voltage increases; on the other hand the electrostatic force causes a higher mass flow from the spinneret so that the diameter can increase again.

With regard to the **gap distance** between spinneret and collector two opposing effects must be considered: by increasing the distance the electrified jet has more time to travel and to get thinner during the process [81, 109], but for a constant applied voltage the electric field gets weaker so that less stretching can occur which can lead to thicker fibres [106] or even a complete stop of electrospinning when not enough electric field strength can be applied to the setup. Also one has to take care that one stays within the range that the fibres are not still wet because of too low distance or have already dried too high above the collector so that no difference is visible for different distances [92].

Environmental conditions

The **humidity** of the atmosphere in which the electrospinning is performed influences mainly the evaporation rate of the solvent, but can also influence chemical and molecular interactions of the polymer and solvent. For example de Vrieze et al. [110] could identify controversial trends for the water absorbing polymer PVP and cellulose acetate that is not water soluble: for PVP a decrease of fibre diameter with higher humidity, for the cellulose acetate an increase of diameter was observed. The latter case they explain by the fact that water absorption leads to a faster precipitation of the polymer in the jet which prohibits the elongation and thinning during electrospinning to some extent. For PVP on the other hand water absorption leads to slower solidification so that the

elongation and thinning process can continue for a longer time and the fibres get thinner, an effect also observed for PEO [111, 112].

If the humidity is too high however only fused fibres are deposited on the collector. For PVP at room temperature this effect was found for 60% relative humidity [110]. But also the atmospheric **temperature** played a role as it affects the evaporation rate: for 10 °C they found the fused fibres already at 45% relative humidity. A lower temperature also increases solution viscosity and conductivity and decreases surface tension so that the overall effect can not be generally predicted [110, 113]. In the paper by de Vrieze et al. for both tested polymers a minimum diameter was obtained at room temperature. Of course also a too dry atmosphere can cause problems and might even prevent electrospinning if the solvent evaporates strongly while the solution droplet is still hanging on the spinneret [114].

2.2.3 Fibre Collection: Nonwovens and aligned Fibres

As was stated already, if the simplest collector, a grounded metal plate, is used, the fibres are deposited in a random way. The resulting fibre mat is therefore also described as a nonwoven mat. But with other collectors it is also possible to achieve mats of aligned fibres or the controlled deposition of single fibres. An extensive review of different collector designs and other setup variations was written by Teo and Ramakrishna [115]. One often used collector to achieve aligned fibres is a rotating drum or mandrel [116, 117, 118] in which the rotating speed determines the degree of alignment.

A different, very simple method to achieve uniaxially aligned fibres was proposed by Li et al. in 2003 [119]. Instead of one single electrode as collector two parallel aligned electrodes are placed in one plane below the spinneret, positioned symmetrically about the latter (cf. fig. 2.15a). Both are connected to ground, in this way realising a split collector configuration. This introduces a strong horizontal component of the electric field in the vicinity of the collector, in contrast to the standard configuration where the field lines are essentially perpendicular to the collector at this level (cf. fig. 2.15b,c).

Due to the symmetry of the configuration the horizontal component changes sign at the middle (defined by the vertical extension of the spinneret). This has the effect that a charged section of a fibre on the right side of the middle is attracted to the right electrode, whereas a corresponding section on the left side is attracted to the left electrode, when the fibre approaches the plane of the collector. When a fibre is deposited on the collector it is thus stretched between the electrodes producing a mat in which the fibres are aligned preferentially perpendicular to the electrodes. The effect is further enhanced by the electrostatic repulsion between the deposited fibres spanning the gap between the electrodes, all carrying the same sign of charge, which is not immediately neutralised. In a similar way aligned fibres can also be gained by using a configuration where the electrode forms a rectangular frame [120]. For the quality of alignment in

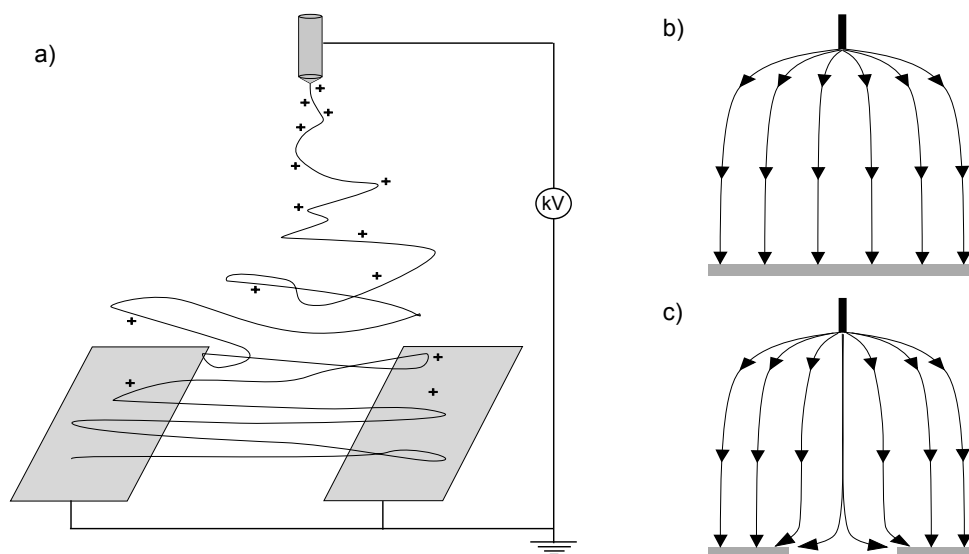


Figure 2.15: a) Electrospinning setup with split electrodes as collector to gain uniaxially aligned fibres. b,c) Electric field lines for a single electrode and a split electrode collector, respectively.

these methods the gap width between the electrodes [119, 121], the collection time [119], the applied voltage [121] as well as the used collector material, especially its dielectric properties like the relative permittivity [122], are important control parameters.

2.2.4 Coaxial Electrospinning

In this thesis mainly a special version of electrospinning referred to as coaxial electrospinning is applied. It was first shown in 2002 by Loscertales et al. [123] that when two immiscible liquids are pumped through two needles, where one needle is set concentrically inside the other (cf. fig.2.16), a coaxial Taylor cone is generated if a high enough electric field is applied. They could furthermore show that for this coaxial Taylor cone to appear it did not matter if the electric field is applied to the inner or to the outer fluid. However, in this first paper electrospinning led to a breakup of the jet so that not fibres, but monodisperse compound droplets with one liquid encapsulated inside the other, were the final result of the experiment. The first coaxial fibres were reported soon afterwards by Sun et al. [124] who spun two solutions of different polymers inside each other. An advantage is that not only polymers can be used in this method but the inner fluid can also be a low-molecular mass compound that normally could not be electrospun [125, 126]. If the inner fluid evaporates during electrospinning [125] or is removed by extraction afterwards [126] also hollow fibres can be realised.

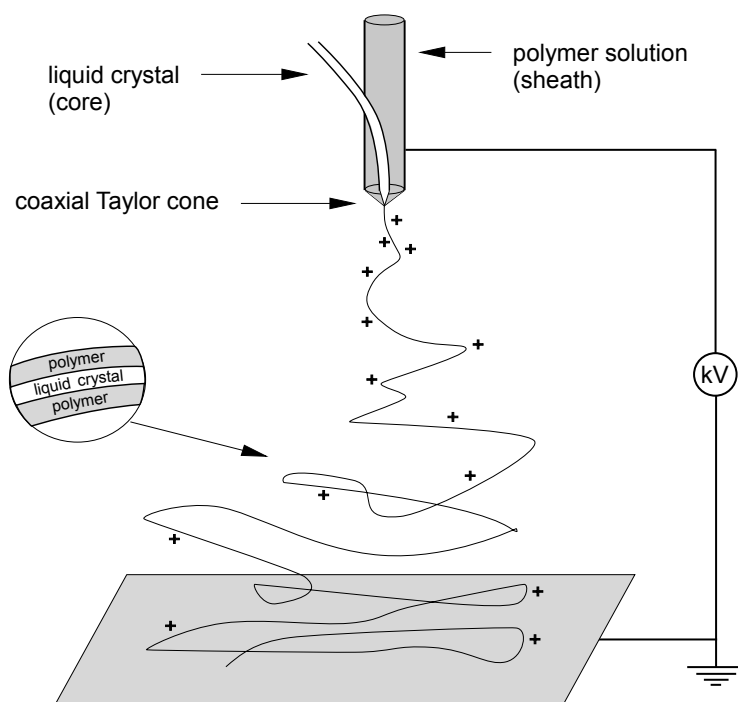


Figure 2.16: Schematic drawing of a setup for coaxial electrospinning showing the insertion system in the spinneret, the coaxial Taylor cone as well as the resulting core-shell fibre.

Note that if only the outer fluid is connected to the high-voltage power supply, also only this fluid gets charged during the process, while the core fluid is not affected directly by the electrostatic forces [127]. Instead the core fluid is subjected to mechanical stress as a result of the electrostatic driven stretching of the outer fluid. Compared to the high speeds of this process diffusion processes between the outer and inner fluids are very slow and can be basically neglected. This leads to the effect, that in some cases miscible fluids or even fluids with identical solvents remain as core-shell systems, nevertheless it seems that immiscible fluids show a sharper core-shell boundary [128]. An overview of materials used in coaxial electrospinning as well as of the effects of material and processing parameters can be found in the review paper by Moghe and Gupta [129], even though systematic studies of the latter are rare up to now and some results are in contradiction to each other. Coaxial electrospinning has found already many possible applications as described for example in the review papers by Yarin et al. [128, 130]: from medical issues like the encapsulation of biologically active compounds for protection or drugs for a later release to applications as microfluidic channels, for the formation of nanotubes or as functionalised textiles.

Chapter 3

Experimental Part

3.1 Development of the Setup for coaxial Electrospinning

As already introduced in chapter 2.2, an electrospinning setup consists of these main components: a polymer solution that is pumped through a metallic needle or tube, a high voltage power supply to charge the solution and a grounded collector on which the resulting fibres are deposited. For coaxial electrospinning a second fluid is introduced into the system by pumping it through a fine capillary inserted into the polymer solution as was sketched in fig. 2.16. In the following the setup developed in our laboratory will be described in detail.

In most cases the quite viscous solutions are pumped by syringe pumps resulting in the disadvantage of long stabilisation times for the flow rates (45 minutes or longer is not uncommon), difficult temperature control and the need for one syringe pump for each solution. To avoid this and make the system more flexible a microfluidic control unit with four independent channels (Fluigent MFCS-4C-1000mbar) is applied replacing up to four syringe pumps (fig. 3.1a). This device is used to pressurise a vial with solution. Through an outlet tube dipped into the solution, the solution starts to flow out when an overpressure compared to the atmospheric pressure is reached. In case of laminar flow the volumetric flow rate \dot{V} is then determined by the dynamic viscosity of the solution η , the tube dimensions (inner radius r_{tube} and length l_{tube}) and the pressure difference Δp between the ends of the tube. The relation is described by the Hagen-Poiseuille equation below.

$$\dot{V} = \frac{dV}{dt} = \frac{\pi}{8\eta} \frac{r_{tube}^4}{l_{tube}} \cdot |\Delta p| \quad (3.1)$$

With the microfluidic system a new flow rate is stabilised within seconds and so much faster than with the syringe pump method. The disadvantage is that the value of the flow rate cannot be directly read and controlled since only the pressure is adjustable.

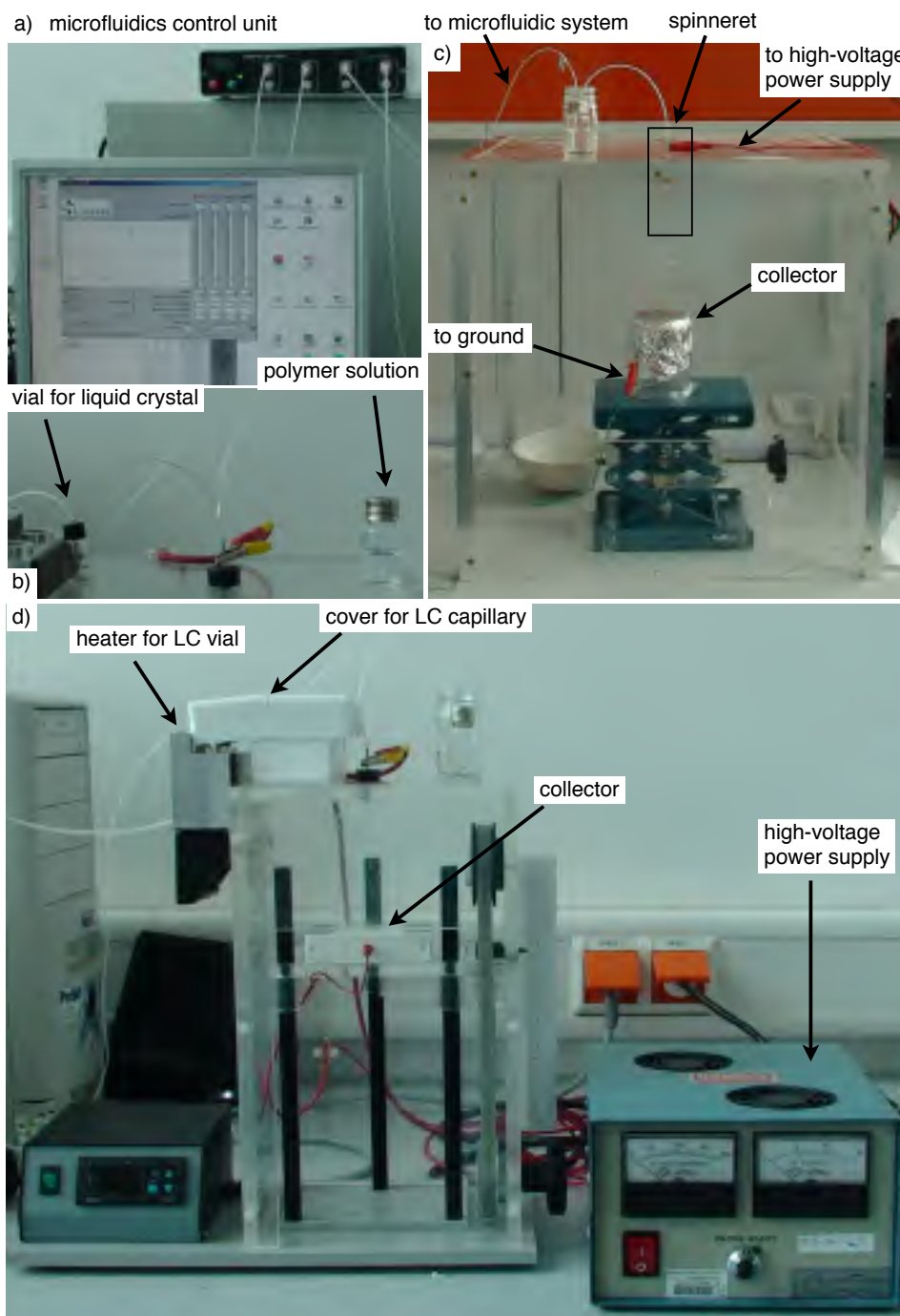


Figure 3.1: The electrospinning setup as developed in our laboratory. a) Microfluidics device with software control. b) Connection of the tubings for coaxial electrospinning, ending in the metallic tube that is attached to the high voltage power supply. c) Very simple setup consisting mainly of a plexiglas box with the spinneret at the top and the grounded collector inside. d) Advanced setup with heater for the liquid crystal.

Instead, this value has to be calculated for each pressure from the mass of the solution pumped in a certain time and its density.

Two kinds of vial were used: For larger volumes (5 or 10 ml) vials with screw caps with a septum were used through which the air and outlet tube could be easily inserted and replaced if necessary. But since the liquid crystals in most cases are not available, and also not needed, in such large volumes as core material, smaller vials were used where no screw caps with septum were available. In these cases holes were pierced through the caps, the tubes inserted and the cap then sealed with epoxy glue which was left for drying over night before application. The polymer solution was pumped through a teflon tube with inner diameter of 1.45 mm and the core fluids through polyimide-coated silica capillaries (BGB Analytik AG), with 250 or 320 μm inner diameter (350 or 450 μm outer diameter, respectively), both materials being resistant against heat and most chemicals.

The connection of the inner capillary and the outer tube was done by piercing a very small hole into the tube just large enough to introduce the capillary. Because the teflon tube then closes very narrowly around the capillary by itself, it was not necessary to fix the capillary with glue but it was enough to wrap this part densely with teflon tape to achieve a stable and tight connection (fig. 3.1b). In this way the inner capillary as well as the outer tube can be removed easily without having to replace the whole system, for example when using a new fluid or in case of clogging.

Because no syringe pump was used in the setup there was also no need to apply a syringe *needle* as metallic connection to the high voltage power supply (Gamma High Voltage Research). This aspect was quite beneficial as it turned out to be difficult to buy syringe needles with a desired *inner* diameter. In most cases only the outer diameter could be chosen, sometimes the inner diameter was not even indicated. In our setup it was therefore replaced by a simple metal tube with either 0.7 mm or 1 mm inner diameter, for single-fluid and coaxial systems, respectively, and an outer diameter of 1.45 mm, fitting directly to the diameter of the teflon tube. The inner capillary must be pushed until the end of the metallic tube to avoid that the outer and inner solutions meet already in this part.

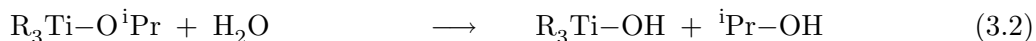
As shown in fig. 3.1, in the first very simple setup (c) as well as in the more advanced second version of the setup (d), the actual fibre formation takes place in a plexiglass box. The metallic tube is attached through a hole at the top of the box and the fibres form between the orifice and the grounded collector, whose height can be varied. With the high voltage power supply a voltage up to +30 kV can be applied. To ensure an undisturbed electric field from the spinneret to the collector, the clip to the power supply is attached to the metallic tube on the outside, not inside the box. When the box is closed, the humidity of the atmosphere can be regulated with a drying powder. It was adjusted between 30 and 45 % relative humidity, as for PVP in ethanol it was found that a relative humidity of 60 % or higher leads to fusion of insufficiently dried fibres

on the collector [110] while too dry atmosphere might prevent electrospinning by drying already the droplet hanging on the spinneret [114].

In the present version of the setup a heating block is attached on the side which heats the vials. With a ventilator on its top the generated warm air also flows along the tubing, so that the temperature difference between the pumped fluids and the outer atmosphere is reduced. At the maximum heater temperature of 140 °C an air temperature of almost 80 °C can be achieved below a Teflon cover surrounding the capillary. With this heater it is possible to also use liquid crystals that are crystalline or too viscous at room temperature.

3.2 Optimising the Polymer Solutions

From the very first study of coaxial electrospinning with liquid crystalline core, done by J. Lagerwall in cooperation with J. McCann and Y. Xia from the University of Seattle [5], it was known that PVP in combination with a sol-gel process resulting in TiO_2 was a suitable sheath material for such composite fibres. Therefore it was a natural choice to do the first experiments with our own electrospinning setup with this sheath. The liquid crystal however was replaced by the alkane hexadecane as a model non-polar core fluid. The sheath solution was composed of 0.3 g PVP, 5 ml ethanol, 3 ml of titanium(IV) isopropoxide ($\text{Ti}(\text{O}^i\text{Pr})_4$, chemical structure depicted in fig. 3.3) as sol-gel-precursor and 2 ml acetic acid as catalyst [131, 126]. The sol-gel conversion involves two reaction steps: hydrolysis of the metal alkoxide groups to hydroxides (cf. eqn. 3.2 below), followed by condensation reactions between two hydroxide groups or between a hydroxide and an alkoxide group (eqn. 3.3 and 3.4, respectively) [132]. In the scheme R can represent the original O^iPr group, an OH group or an already condensated part, depending on the stage of the reaction.



It was found that this outer solution had a too low viscosity to work properly in our setup, so that even with the lowest pressures there was always electrospinning overlaid with dripping. Probably the cause was that the employed teflon and metallic tube had larger inner diameters than in the previous experiments (metallic needle with 0.5 mm inner diameter compared to 0.7 – 1 mm in the present case). Since this parameter could not be changed so easily, the viscosity of the solution was increased. Therefore a solution was prepared that contained 1 g PVP instead of 0.3 g, while the amounts of the other components stayed the same. And indeed the dripping could be avoided in this way. But another problem occurred: despite that the spinneret was wiped regularly with a cotton

bud soaked in ethanol to clean it from titanium acetate formed as intermediate reaction step, clogging of both the inner and outer tube occurred in about 30 minutes. Since this clogging had already happened with the previous solution, although in a smaller extent, it was decided to try if one could work with a solution with only the polymer and no sol-gel-process.

As a next step, a solution of 10 wt.% PVP in ethanol was attempted. But the resulting fibres were not smooth, as they should be, but contained many beads as can be seen from fig. 3.2a, even though in non-coaxial electrospinning this was not the case. One simple method to prevent beads is to increase the flow rate. Thereby the amount of beads could be reduced, but not fully prevented before the flow rate was so high that also dripping started during the spinning process. As beading occurs when the surface tension of the polymer solution is stronger than the electrostatic forces, the latter force should be strengthened by increasing the solution conductivity by the help of a small amount of salt added to the polymer solution [72].

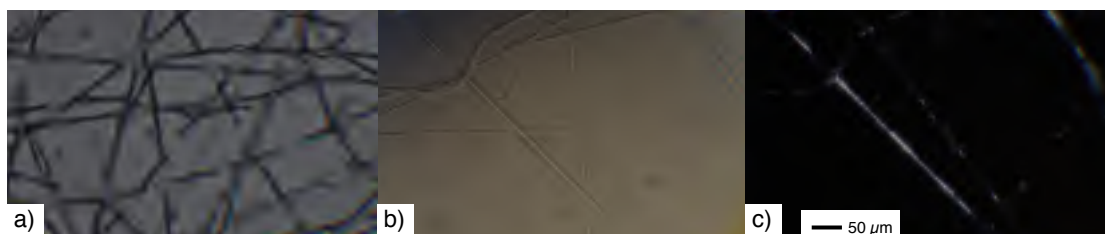


Figure 3.2: a) Coaxial fibres from an outer solution of 10 wt.% PVP in ethanol and inner fluid hexadecane showing many beading structures. They were spun at flow rates of 0.42 and 0.26 ml h^{-1} , respectively, with a voltage of 10 kV over 10 cm distance. (b, c) Smooth fibres made with an outer solution of 15 wt.% PVP and 0.5 wt.% NaCl in ethanol, filled with the nematic liquid crystal 5CB, the right picture observed by polarising optical microscopy. The flow rates were 0.7 and 0.03 ml h^{-1} for outer and inner fluids, respectively.

For PVP concentrations of 10, 12.5 and 15 wt.% the addition of 0.5 and 1 wt.% NaCl was investigated. In all cases, no beads were observed any more. For the higher salt concentration a slightly smaller mean fibre diameter was found while the range of diameters stayed the same. With increasing polymer concentration the fibre diameter increases, as to be expected. As can be seen for example in the photo in fig. 3.2b, where the hexadecane is replaced by the liquid crystal 5CB, smooth fibres were achieved also with this core fluid by using these outer solutions. Furthermore, it turned out that the pure PVP sheath is transparent and almost optically isotropic so that one can directly observe the birefringent liquid crystal core through a polarising optical microscope and follow the phase sequence.

Since ethanol is a quite bad solvent for NaCl, for both studied concentrations there was always a rest of non-dissolved, crystalline salt staying at the bottom of the solutions. The actual equilibrium concentration of the salt was not determined, but theoretically it should be the same for both added amounts. From this argumentation it was decided to use the 0.5 wt% NaCl to keep the amount of crystals that are pumped with the solution and thereby disturbing the electrospinning process as small as possible. For these solutions a voltage of 10 kV and a spinneret – collector distance of 10 cm were established as standard conditions.

As will be described in detail in chapter 6.3 it was found by scanning electron microscopy (SEM) investigations on the fibres with the cholesteric liquid crystal that the morphology of fibres made with these solutions is sometimes not as regular as it appears in optical microscopy. Especially with increasing LC filling the fibres may become half-cylindrical instead of having a completely circular cross section, a difference impossible to distinguish by optical microscopy. The conditions leading to this situation and its possible origins will be discussed in the mentioned chapter. But it was also found that the morphology could be significantly improved when introducing about 9 wt.% of TiO₂ into the fibre by the sol-gel-process described above (the original mixture results in 73 wt.% TiO₂ in the fibre). Since these SEM investigations were possible only shortly before the end of this thesis work, this could be taken into account only for the fibres with the room-temperature SmC LC (chapter 5.3).

3.3 Used Materials

Following the discussion in the previous section and experience with poly(vinyl alcohol) of Nicole Sonnenberger in her bachelor thesis [133] the following outer polymer solutions were used:

- 12.5 wt.% PVP solution: 625 mg PVP ($M_w = 1\,300\,000\text{ g mol}^{-1}$, Acros) and 25 mg NaCl (0.5 wt.% of solution) dissolved in 5.505 ml ethanol (purity $\geq 99.8\%$, Roth) by stirring over night. The flow rate was set at 1.8 or 3.0 ml h⁻¹ ($\Delta p = 20$ or 40 mbar).
- 15 wt.% PVP solution: 750 mg PVP and 25 mg NaCl dissolved in 5.350 ml ethanol. Flow rate: 0.6 or 0.7 ml h⁻¹ ($\Delta p = 30$ or 50 mbar).
- PVP-TiO₂ solution: 439 mg PVP (9.5 wt.% of solution), 0.150 ml Ti(OⁱPr)₄ (purity 97%, Aldrich) and 0.100 ml acetic acid dissolved in 5 ml ethanol. When the sol-

gel-process is completed these fibres contain 9 wt.% TiO_2 .[‡] Flow rate: 0.9 ml h^{-1} ($\Delta p = 10 \text{ mbar}$).

- PVA solution: 1.4 g (26 wt.%) PVA ($M_w = 20\,000 - 30\,000 \text{ g mol}^{-1}$, 88% hydrolyzed, Acros) in 4 ml water. This solution was prepared by bath ultrasonication over night. Applied pressure: $\Delta p = 30 \text{ mbar}$.

All liquid crystals except the nematic mixture RO-TN-403/015S (cryst. $< 0 \text{ N } 81.5 \text{ iso. } / ^\circ\text{C}$, Hoffmann-La Roche) were bought from Synthon Chemicals. The structures and exact chemical names are shown in fig. 3.3. For the studies on nematic and SmA phase the liquid crystals 5CB (cryst. $21.8 \text{ N } 33.1 \text{ iso. } / ^\circ\text{C}$, onset temperatures from DSC) and 8CB (cryst. $20.5 \text{ SmA } 32.0 \text{ N } 39.2 \text{ iso. } / ^\circ\text{C}$) were used. To achieve a liquid crystal with a SmC phase at room temperature a mixture of 6OPhPy8 and 8OPhPy8 at mass ratio of 50/50 was prepared with a phase sequence of SmC $49.7 \text{ SmA } 59.8 \text{ N } 67.9 \text{ iso. } / ^\circ\text{C}$ (DSC and POM investigations). The chiral dopant CB15 is known for inducing not only cholesteric but more interestingly also the rarely occurring Blue Phases when added to nematic host phases. An overview of investigated mixtures is given in [134]. For this study the multi-component nematic mixture RO-TN-403 was doped at 50/50 mass ratio with CB15. The resulting short-pitch liquid crystal had the following phase sequence: N* $28.5 \text{ BP}^* 30.2 \text{ iso. } / ^\circ\text{C}$.

In the experiments with 8CB, the SmC mixture and the cholesteric mixture the flow rate of the LCs in the coaxial system was varied. In table 3.1 and in fig. 3.4 the relation between applied pressure and resulting flow rate are shown. 8CB and the cholesteric mixture were used at room temperature. Instead of this for the SmC mixture a temperature of $140 ^\circ\text{C}$ was set for the heater of the LC vial. The air surrounding the capillary, up to the connection to the outer tube, was thereby heated to almost $80 ^\circ\text{C}$ (with the help of the ventilator and the cover). This high temperature ensured that the liquid crystal was still isotropic before the point where the capillary was introduced into the tube for the polymer solution. Which temperature, and corresponding phase, the LC had at the end of the spinneret could not be determined, but one has to expect a temperature drop and therefore also a drop of flow rate when the capillary with the LC is surrounded by the polymer solution that had an estimated temperature of only $30\text{--}40 ^\circ\text{C}$ [§].

In a first experiment to determine the flow rate of the SmC mixture this fact was not taken into account as only the heated LC was pumped without the surrounding cooler

[‡]The $0.150 \text{ ml Ti}(\text{O}^i\text{Pr})_4$ correspond with a density of 0.955 g ml^{-1} and a molar mass of $284.26 \text{ g mol}^{-1}$ to an amount of 0.504 mmol . After the reaction is fully completed these 0.504 mmol correspond to 40 mg TiO_2 in the fibres.

[§]Even though the vial for the polymer solution was not in the heater or below the cover, it was also heated to a smaller extent by the flow of warm air. The reason for not heating it directly was to prevent a too high temperature that would lead to a too fast evaporation of the solvent and / or too fast sol-gel-process.

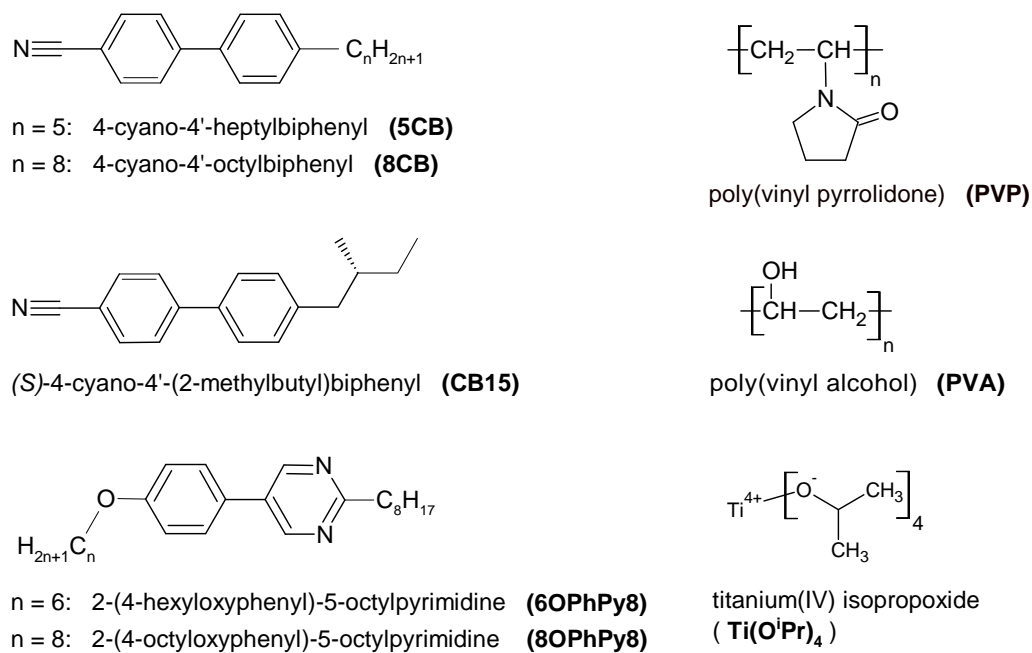


Figure 3.3: Chemical structures of the liquid crystals used as core materials and of the two polymers used as sheath of the electrospun fibres.

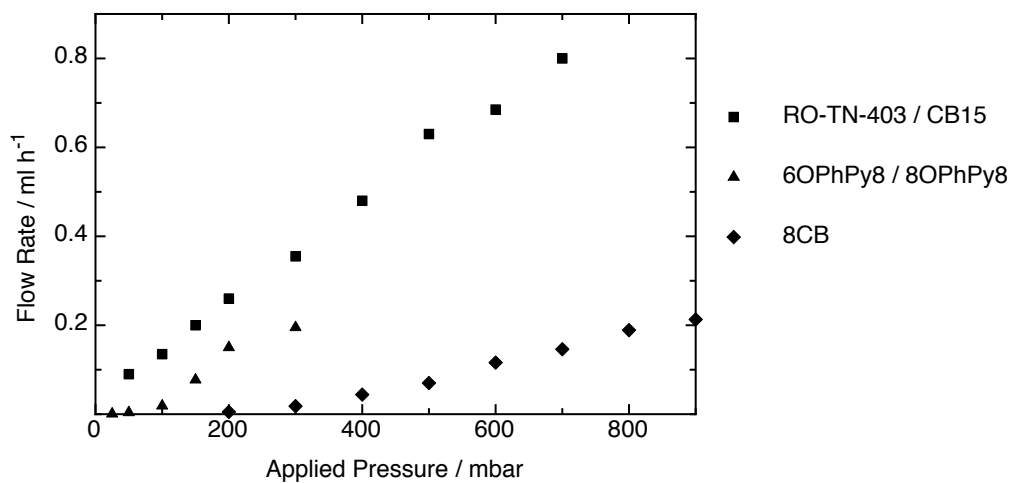


Figure 3.4: Flow rates of the different liquid crystals as used in the experiments in this thesis.

Table 3.1: Flow rates (in $\mu\text{l h}^{-1}$) of the used liquid crystals as function of applied pressure

Δp / mbar	8CB ^a	CB15 / RO-TN-403 ^b	6OPhPy8 / 8OPhPy8 ^c	
			measured	calculated ^d
25			5	1
50		90	25	4
100		135	125	20
150		200	515	80
200	5	260	1030	150 ^e
300	20	355	1320	200
400	45	480		
500	70	630		
600	115	685		
700	145	800		
800	190			
900	215			

^acapillary dimensions: $r_{tube} = 160 \mu\text{m}$, $l_{tube} = 24 \text{ cm}$

^bcapillary dimensions: $r_{tube} = 125 \mu\text{m}$, $l_{tube} = 24 \text{ cm}$

^ccapillary dimensions: $r_{tube} = 125 \mu\text{m}$, $l_{tube} = 24 \text{ cm}$

^dcalculated from the previous column as described in the main text

^emeasured value from coaxial flow

polymer solution. Therefore the obtained values were much higher than for the other LCs. To find out the difference between these values and the true flow rates a second experiment was performed: for one pressure the coaxial flow of LC and polymer solution was repeated exactly like in the electrospinning experiment. In this case of course only the mass of LC plus polymer solution per time was directly measured, but as the flow rate of the latter was already known, the amount of LC could be calculated. The LC flow rate determined in this way was then only about 15% of the value obtained in the first experiment. For the other pressures a similar reduction can be assumed and the values calculated in this way fit much better to the flow rates of the other LCs. Also it turns out that the fibres with this LC have diameters in the same range as with the other LCs, which would be quite unexpected for a LC content as suggested by the much higher, originally determined flow rates.

For details on the experiments with the LC elastomer refer to the relevant chapter.

3.4 Polarising Optical Microscopy

The optical properties of the liquid crystal cores, their phases and phase transitions, were investigated on a Nikon polarising optical microscope (Eclipse LV100), equipped either with an Instec or a Mettler hot stage. Photographs were taken with a Sony Handycam video camera or a ScopeTek DCM500 microscope camera. Fibre diameters and the fibre angles for study on their alignment were determined with the software ScopePhoto (ScopeTek). For each studied condition 50 measurements were averaged.

3.5 Differential Scanning Calorimetry

For the calorimetric measurements a thick, nonwoven mat was spun on a glass slide. This was then kept in the laboratory at room temperature and moderate to low humidity for at least one day to ensure complete evaporation of the solvent or a complete sol-gel-reaction, respectively. About 5 to 15 mg of the mat were peeled off the glass slide with a spatula and carefully folded to a small, dense piece that would fit into the aluminium sample cell. For these fibre samples standard DSC cells for solids could not be used, because when closing these cells the cover is pressed directly on the sample, so that the thin fibres get squeezed and destroyed. Instead, cells designed for liquids were used, where only the brim of the cover is pressed onto the lower part, and in this way no pressure acts on the sample. The measurements were carried out on a Perkin Elmer Pyris 1 DSC. The standard temperature program was: heating from 20 °C to a temperature about 20 K above the expected clearing temperature of the LC, cooling to 20 °C, repeat the heating; all parts at a rate of 10 K min⁻¹. This program was modified if necessary, with a lowest possible temperature of 10 °C. The phase transition temperatures were determined as the onset-temperatures in the DSC thermograms on heating.

3.6 X-Ray Diffraction

Fibres and bulk liquid crystals were investigated by X-ray scattering experiments by Dr. Ute Baumeister, Martin-Luther-Universität Halle-Wittenberg. The diffraction patterns were recorded with a 2D detector (HI-STAR, Siemens) using Ni-filtered CuK_α radiation. Samples of bulk liquid crystals on a glass plate were aligned at the sample-air interface by cooling slowly from the isotropic phase or by applying a magnetic field.

To gain information about the orientation of the liquid crystal molecules (and the layers of the smectic phases) inside the fibres, 2D X-ray diffraction patterns were recorded on uniformly aligned fibres. About 5 to 15 mg fibres were rolled up to achieve a compact sample. Scrolls with two perpendicular roll-up directions were investigated (fig. 3.5b), freely hanging on the sample holder shown in fig. 3.5a. It turned out that for the first

sketched way the orientation is more clearly distinguishable in the diffraction pattern than for the second way. This is mainly due to the facts that the roll up direction can be better controlled in the first case and that in the second case the X-ray beam is directed along rather than across the fibres in a large part of the sample, thereby not producing any significant scattering response. A temperature-controlled heating stage was used to heat the sample. To reduce the temperature difference to the environment a teflon cover for the sample holder was used. The heating stage was calibrated for samples lying on thin glass plates directly placed on the heater, but not for a hanging sample as in this case. Because of this an error for the temperature of ± 5 K is expected.

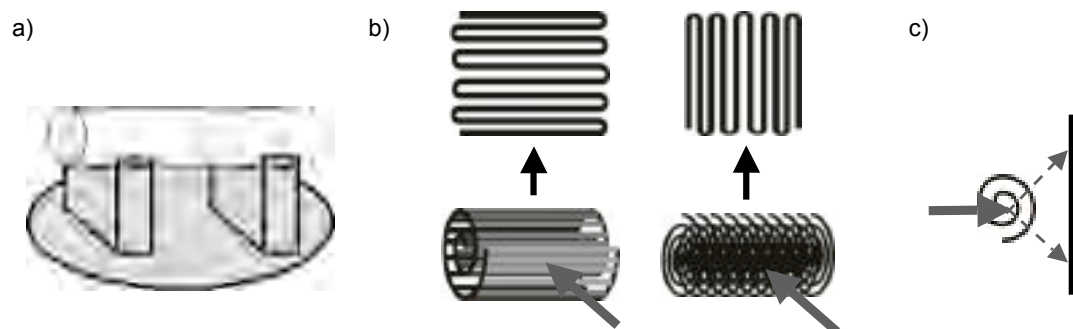


Figure 3.5: a) Sketch of the used sample holder designed for samples in a glass capillary (sketched as transparent cylinder), in our case used for holding a rolled fibre mat. The heating stage below and the cover are not shown. b) Schematic sketch of oriented fibres at two perpendicular roll up directions. The incident X-ray beam is represented by the grey arrow. c) Diffraction from a rolled fibre. Grey arrow: incident beam, dashed arrows: diffracted beams, black vertical line: 2D detector. (Sketches in (b, c): courtesy of Dr. Ute Baumeister)

3.7 Electron Microscopy

The outer fibre morphology was investigated by scanning electron microscopy by Dr. Giusy Scalia and Oronzo Calò at ENEA Portici (Naples), Italy. For this purpose the fibres were spun onto a silicon target instead of a glass slide. It is important to note that the samples were not metallized prior to investigation, as is often the case in SEM investigations of polymers, but it was really the true fibre surfaces that were studied.

Focused ion beam (FIB) investigations were performed by Dr. Giusy Scalia and Vera La Ferrara at ENEA Portici (Naples), Italy. The samples were prepared in the same way as for the SEM investigations.

Chapter 4

Alignment of electrospun Fibres

As was already described in chapter 2.2.3 there are several methods to achieve uniaxially aligned electrospun fibres. Among the easiest to practically realise is to use a collector consisting of two conducting strips separated by a gap [119] or a frame of conducting material [120]. When we tried to establish these alignment methods in our own laboratory we encountered an unexpected problem. Especially when using a frame collector the fibres sometimes did not form a freely hanging mat as expected, but were drawn to the bottom in the middle of the collector, as can be seen in fig. 4.1. Starting from this observation and since no information on the possible influence of the height of the electrodes to the bottom for such collectors was described in the literature a systematic study was carried out.



Figure 4.1: *Poly(vinyl alcohol) (PVA) fibres with 8CB as core material deposited with a grounded frame of aluminium foil as collector (reproduced from [133]).*

Three collector configurations with separated electrodes and two configurations with the electrode forming a continuous frame, of varying dimensions, were investigated (fig. 4.2). They consisted of styrofoam as supporting material on which the electrodes of (folded) aluminium foil were placed. For each configuration the height h of the electrodes relative to the bottom was varied and poly(vinyl pyrrolidone) (PVP) fibres were spun onto them. After each spinning experiment the resulting fibre mat was transferred to glass slides for the microscopic investigation. It was found of great importance that the slide was not held manually between the collectors during electrospinning, but was

placed there either before or after spinning had been stopped. Otherwise the orientation of the fibres got worse. The most likely explanation is that by introducing the glass slide while holding it on one side with one's fingers, the electric field between the electrodes gets disturbed.

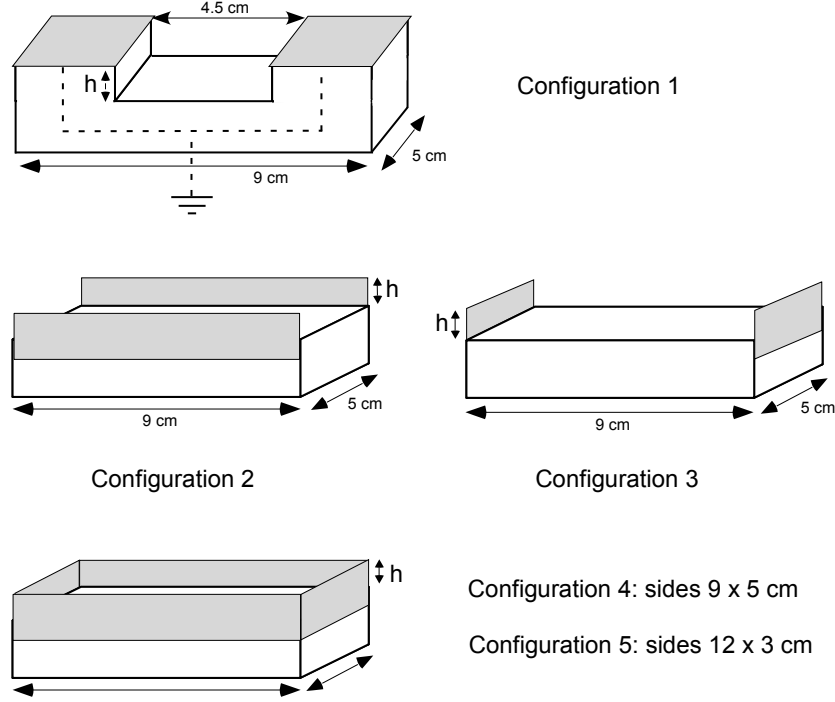


Figure 4.2: Collector configurations investigated in this part, that should gain aligned fibres. The grey areas indicate the aluminium foils which are connected to the ground (only sketched for collector 1).

To gain quantitative data on the quality of alignment a representative area of each sample was chosen and for 50 fibres the angle x between the fibre and the ideal orientation was determined. For configuration 1 with horizontal stripes the distributions of angles as well as photos of the fibres are shown in fig. 4.3, for configuration 3 and 4 the distributions are shown in fig. 4.4. The configurations with dual vertical electrodes, 2 and 3, and that with the continuous framed electrode, 4 and 5, show similar tendencies. From the angles the two-dimensional orientational order parameter S_{2D} could be calculated and the corresponding data are plotted in fig. 4.5.

$$S_{2D} = 2 \langle \cos^2 \phi \rangle - 1 \quad (4.1)$$

When having a closer look at the photos and the distributions of angles one can see that in all samples there are a few fibres that show large deviations from the optimum

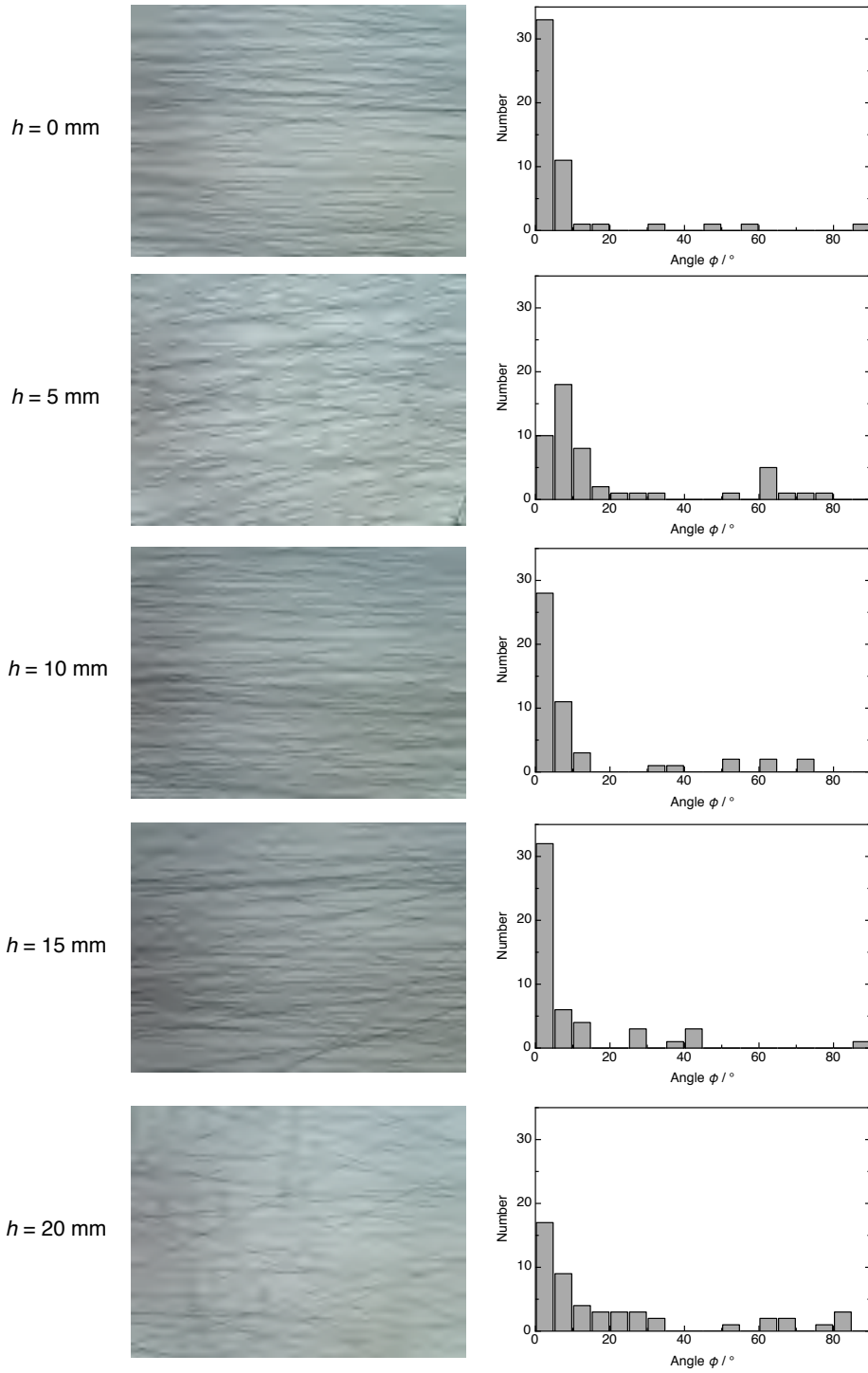


Figure 4.3: Left row: Microscope photos of aligned fibres as resulting from collector configuration 1 on varying height h . Right Row: Distribution of the corresponding fibre angles, as determined from 50 measurements.

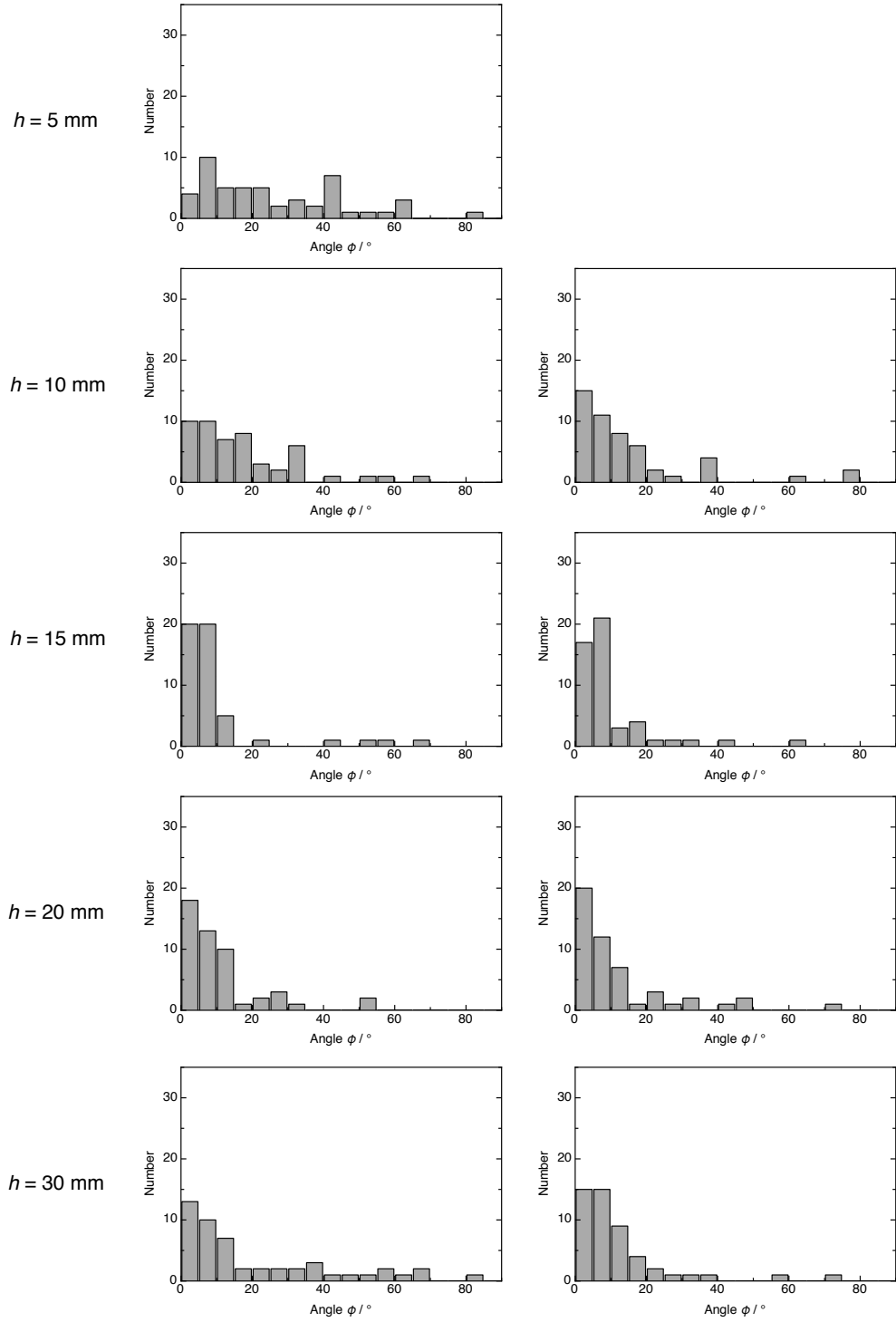


Figure 4.4: Distribution of fibre angles, as determined from 50 measurements, for collector configurations 3 (left row) and 4 (right row) at varying height h .

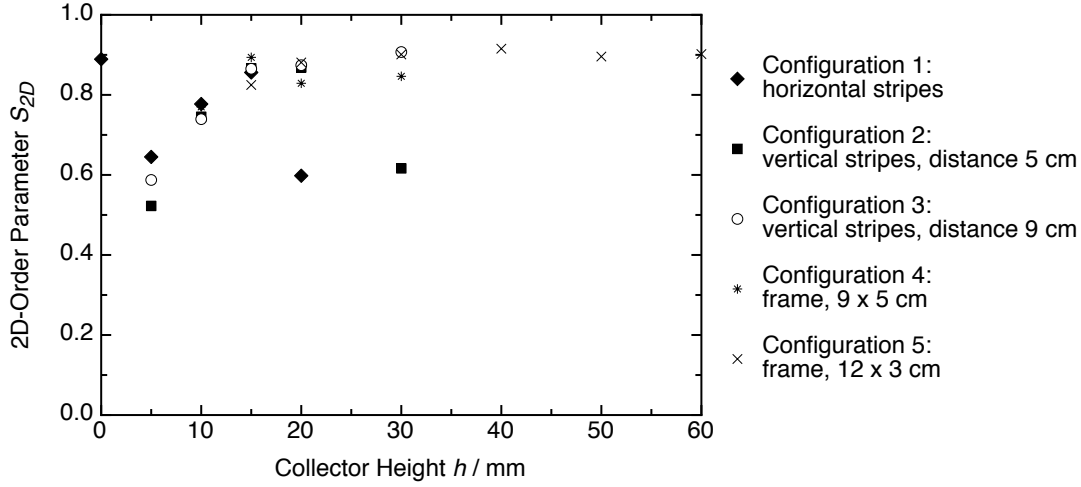


Figure 4.5: 2D-order parameter S_{2D} of the aligned fibres as dependent on the electrode height for the five studied collector geometries.

orientation. In most cases they seem to be loose ends of a fibre that did not reach the second stripe of the collector. For the collectors of configuration 1 the mats have in general quite narrow angular distributions, in the range of $0 - 10^\circ$, but for $h = 5$ and 20 mm a broader distribution is found. Moreover, the latter sample shows a great inhomogeneity of alignment: in some areas it is as good as the others of this series but in most areas the alignment is drastically worse.

Also for the other collector configurations studied an electrode height of 5 mm yielded a very broad distribution, resulting in a minimum of the order parameter for this electrode height around $S_{2D} \approx 0.6$. Between $h = 10$ mm and 15 mm the alignment improves with increasing height for these collector configurations, finally reaching distributions where the fibre angle is almost fully confined to the range of $0 - 10^\circ$, corresponding to an order parameter of $S_{2D} \approx 0.9$. Between $h = 15$ and 30 mm the results are similar with the order parameter staying approximately between 0.8 and 0.9 (exception configuration 2, $h = 30$ mm). Since the configurations 2 – 5 became mechanically more and more unstable with increasing height, as will be discussed below, even greater heights were only investigated for the larger framed collector 5 giving again results of S_{2D} around 0.9 .

Summarised, for the three configurations consisting of conducting stripes a strong influence of the height is found. At $h = 5$ mm they show a minimum of the order parameter followed by a distinct increase, but in two cases it suddenly decreases again above a certain height. The framed collectors appear to show almost no dependence on the collector height in this study, but one must note that the investigated minimum height was above the seemingly important 5 mm. Their minimum of order parameter is

found at 10 mm with a similar value as for the others, so that one can assume an overall similar correlation between h and S_{2D} in this part. The differences between frame, horizontal or vertical stripes as electrodes as well as the side lengths of the electrodes seem to be less important (for the latter parameter at least in the order of magnitude investigated here). A possible explanation for the correlation between collector height and quality of alignment can be given when considering the behaviour of the fibres during collection as will be discussed now.

During electrospinning, for all configurations but that with $h = 0$, it was observed that the fibres do not immediately form a flat mat hanging in the same horizontal plane as the electrodes, but they rather form bows below and above the gap as is sketched in fig. 4.6a. After a short time (about one second) it seems that the bows are pulled towards a horizontal plane between the electrodes and thereby forming the aligned mat, cf. fig. 4.6b. But the process is too fast to follow the movement of a single fibre by the naked eye. Prior to this transition to the planar mat a difference between the upper and lower fibres might occur: those that are in the upper bows can always easily be pulled downwards, but those in the lower bow can stick to the bottom of the collector if that is too close.

Therefore it was observed that for a height up to about 15 mm the oriented fibres did not form a completely freely hanging mat, but were partly or even all hanging down to the bottom of the collector and staying like this, similar to what was seen in fig. 4.1. The lower the collector the more fibres stick to the bottom. In case of vanishing director height $h = 0$, however the downwards directed bow is suppressed by the styrofoam that fills the space between the electrodes, hence the fibres are deposited directly on the middle of the collector as had been described in [119]. We can thus conclude that the best choice for achieving aligned fibres is either to have flat electrodes at the same height as the dielectric base of the collector, or to have vertical electrodes extending sufficiently high up from the dielectric base, at least some 20 mm under the conditions investigated here, but not so high as to render the collector mechanically unstable (see further comments on this below).

After having observed this, the glass slides used as targets were always introduced before the start of the electrospinning process to avoid that they had to be pushed through the hanging fibres for transferring the mat. Doing so results in a random bottom mat, formed by the fibres that were hanging down and attaching to the collector bottom, over which the better aligned mat of free-hanging fibres is eventually picked up. For the frame collectors there was no other option but to introduce the glass slide before fibre formation, otherwise the mat would have been destroyed during transfer. But even though the quantitative results presented here are for samples where this procedure was obeyed, the collector height still turned out to be an important parameter on alignment quality. Let us therefore have a closer look on what might be different between fibres

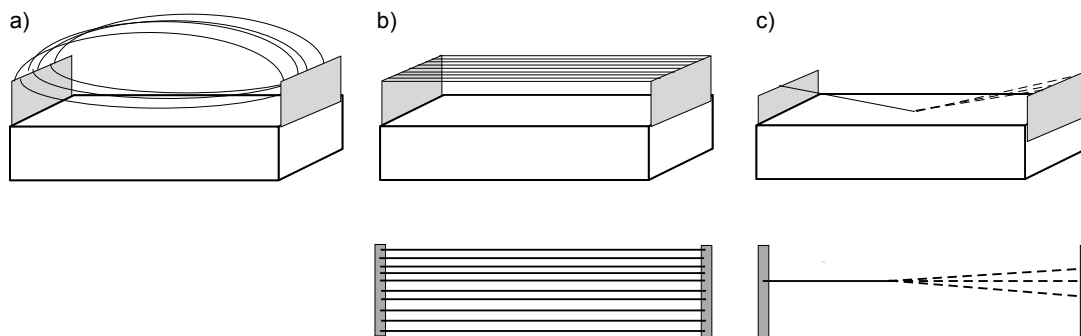


Figure 4.6: Behaviour of electrospun fibres on the investigated collectors immediately after deposition (a) and when completely dried (b, c), viewed from the side and from above. Without sticking to the collector bottom and under ideal conditions the fibres align parallel to each other (b). But if they stick the orientation is lost (c).

touching the collector bottom (or the glass slide) during deposition and those that stay freely hanging.

As already mentioned, in the second case the result is a mat with (almost only) parallel aligned fibres as sketched in fig. 4.6b. A model of what seems to be happening in the first case is sketched in fig. 4.6c for a single fibre: near the electrode of origin (here the left one) the fibre is perpendicular to this electrode when observed from above, as forced by the Coulomb interaction between fibre and electrode, but after hitting the bottom this orientation gets lost in the highly inelastic collision with the collector bottom. The effect is further enhanced by the roughness of the styrofoam bottom surface (which was not perfectly smooth as the collector forms were cut with a knife). Further phenomena may give additional contributions but these are outside the scope of this thesis, as the study of fibre alignment is not a main focus.

The observation that at larger heights sometimes the alignment gets worse again can be explained with the observation that the collector construction is not strong enough to avoid that the fibres pull the electrode stripes towards each other. One can assume that this happens to a smaller extent already before it is clearly visible by eye, so that the distance between the electrodes becomes unequal resulting in less homogenous electric field. For collector 1 this happened because the middle part of styrofoam was made thinner and thinner with increased height, so in principle one could avoid this effect by improving this construction.

After having accomplished quite good results for the alignment of PVP fibres, also **PVA** fibres were studied as they had also been found applicable for electrospinning with liquid crystalline core in the study by Sonnenberger [133]. In contrast to that study, the alignment here was investigated for a sample of lower molar mass ($M_w = 20\,000 - 30\,000$

vs. $88\,000\text{ g mol}^{-1}$) but with a higher concentration (26 vs. 15 wt.% in water) which led to astonishingly disappointing results: with a frame collector it was not possible at all to achieve aligned fibres. The fibres were very short and formed only at the outer or inner side of the frame, but they did not connect the opposite electrodes, even though for the original PVA solution this was possible as was seen in fig. 4.1. For the stripe collectors the results again were unexpected: most of the fibres did not form a mat between the electrodes but instead they were deposited somewhere else (upper part of fig. 4.7). Also those fibres deposited between the electrodes did not form a uniform aligned mat, but the fibres extended almost randomly in all directions within the mat plane (lower part of fig. 4.7).



Figure 4.7: *Attempt to achieve aligned PVA fibres with a collector of configuration 1. Left photo: Most of the fibres are not collected between the grounded aluminium stripes, but go from there to other parts of the setup. Middle and right photo: Two areas of the achieved sample showing the much worse alignment compared to the PVP fibres.*

Which of the changed properties, concentration, solvent (PVA was dissolved in water whereas PVP was dissolved in ethanol) or molar mass, should have such an influence on the fibre properties remains unclear. One should note, however, that the used molar mass of PVA is at the lower limit of electrospinnability, even though with the higher concentration this effect can be overcome to some extent. Remember in this context that concentration and molar mass, or to be more precise the polymer chain length, influence the entanglement of the polymer chains, a property needed for electrospinning. This effect would at least explain the shortness of the fibres deposited on the frame collector. A similar observation that alignment was not possible with the kind of collectors discussed in this chapter was later found also in the experiments with the LC elastomer. The latter also has a relatively low molar mass, giving a hint that this parameter might indeed play a key role. This still remains to be clarified with more experiments, however.

Chapter 5

Fibres with Nematic and Smectic Liquid Crystals

5.1 5CB: a simple Nematic Liquid Crystal

In a first step the well known liquid crystal 5CB with a nematic phase between 21.8 and 33.1 °C was used as core material to investigate the general properties and possible investigation methods of such composite fibres. The sheath of pure PVP turned out to be transparent and largely non-birefringent so that one could directly observe the birefringence of the liquid crystal core through a polarising optical microscope (POM) and follow the phase sequence (cf. fig. 5.1). The fibres are thermally stable enough to be heated repeatedly into the isotropic phase of the contained liquid crystal and cooled down to room temperature again without any change in appearance. In DSC investigations only the transitions of the liquid crystal are found up to about 80 °C where irreversible peaks appear which can be explained by softening of the PVP sheath due to a reduced glass transition temperature. This finding turned out to be a quite general and will be described and explained in more details in chapter 6.3 in context of the external fibre morphology. When kept below this temperatures a fully dried thick fibre mat shows relatively good mechanical stability so that it can be pulled from the glass slide substrate and folded or rolled together.

The shown fibres were spun with a sheath solution of 15 wt.% PVP and 0.5 wt.% NaCl in ethanol at outer and inner flow rates of 0.7 and 0.03 ml h⁻¹, respectively. They had a broad range of diameters, but most of them were rather thin (about 2 µm outer diameter) and only partly filled. When heating these fibres in the microscope one could see the nematic to isotropic transition starting at 37 °C but some birefringent spots stay until about 40 °C (see fig. 5.1). In the DSC measurements only the melting peak is visible, but no clearing point (fig. 5.2a). Most likely the latter is not detectable in the fibres investigated because of the small amount of LC compared to the total mass of the

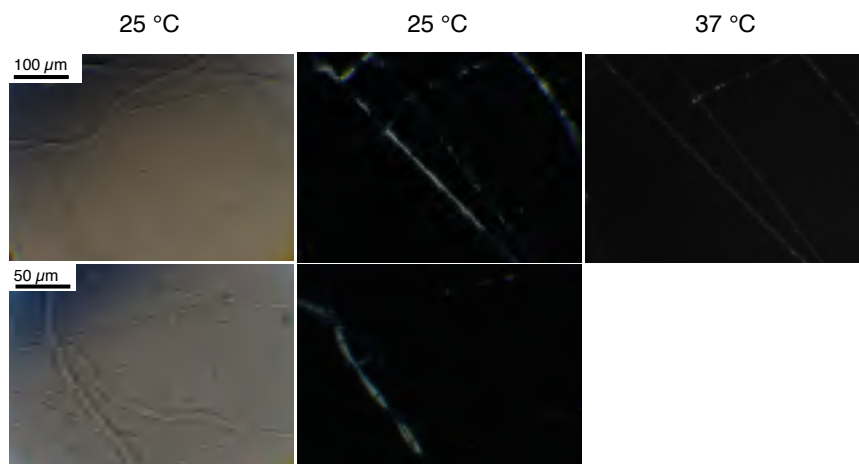


Figure 5.1: Microscopy photographs showing two areas of the same sample of PVP fibres with the liquid crystal 5CB as core material. The three photos on the right are observed with polarising microscopy, showing the birefringent properties of the LC visible through the sheath. On heating to the isotropic state the birefringence disappears stepwise, first in the thicker and at higher temperature in the thinnest fibres (in the photo at 37°C still some bright spots are visible).

sample (about 20 wt.% from the ratio of melting enthalpies of fibre and bulk sample), the broad transition range in the fibres and of course also the quite small clearing enthalpy compared to that of melting (see fig. 5.2b).

The same confinement-induced extension of the nematic phase and loss of clear first order phase transition behaviour was seen in the previous study with the nematic mixture RO-TN-403 [5]. The uncommon shape of the melting peak can be attributed to different melting points in fibres of different diameters that are superposed. For the DSC the samples had been kept at 10 °C for 10 minutes before the first heating to induce crystallisation, which was not done in POM. When looking at the cooling and the second heating part of the DSC measurements (without isotherm at 10 °C), no crystallisation was found in bulk 5CB and a partial crystallisation in the fibres. Surface interaction inducing a faster crystallisation in the thinnest fibres than in the bulk and in the thicker fibres might explain this.

5.2 8CB: Extension to a Smectic A Phase

As a second step the liquid crystal 8CB was used as core, which also exhibits a smectic A phase below the nematic. With an inner flow rate of 0.06 ml h^{-1} , the other conditions kept the same as for the described fibres with 5CB, quite well-filled fibres were achieved as can be seen in the photograph in fig. 5.3. Most fibres had outer diameters between

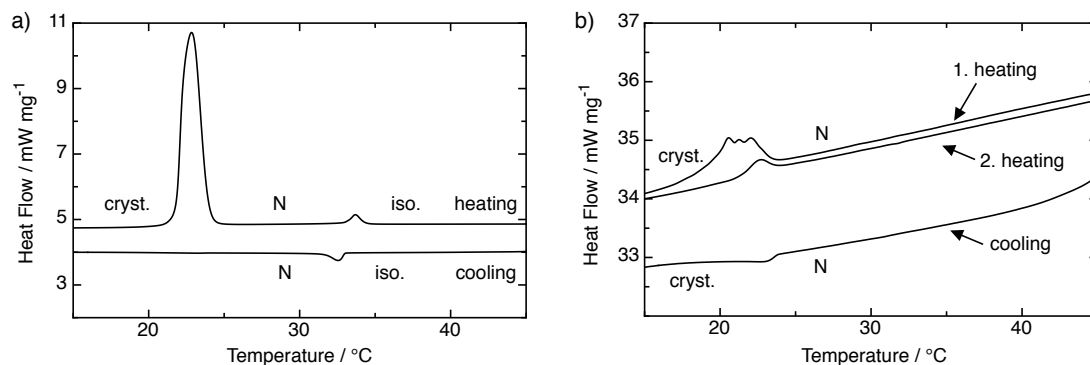


Figure 5.2: DSC thermograms of bulk 5CB (a) and fibres with 5CB core (b) for comparison.

5 and 10 μm , which in comparison to the fibres with 5CB is a larger mean diameter and a narrower distribution, even though the latter was still quite broad. In a way unexpected it was established that one could use this LC directly at room temperature in the SmA phase without having to heat to decrease the viscosity. When heating the spun mat in the microscope the smectic phase could be distinguished from the nematic phase only in the thickest fibres through the disappearance of defects between 33 and 37 $^{\circ}\text{C}$ (left row in fig. 5.3). The clearing transition was clearly visible in all fibres and again the temperature range was broadened to 36 – 42 $^{\circ}\text{C}$, as for the nematic phase of 5CB and the RO-TN-403 mixture. A correlation between clearing temperature and fibre diameters was not found in this sample.

When comparing the DSC thermograms of bulk 8CB and the one obtained with this fibre sample (fig. 5.4) only small differences are found as the onset temperatures of the phase transitions are unchanged. The nematic to isotropic transition is broadened, as was already seen in the microscopy investigations. The most significant change occurred to the SmA – N transition, which seems to have changed from a (weakly) first to a transition with more second order character: It is visible as a kink in the fibre thermogram rather than as a peak in the bulk material and also the continuous transition of the optical properties as seen in the left column in fig. 5.3 supports this.

The melting peak is unexpectedly small in both samples, especially when comparing to literature values where the same temperature, but a transition enthalpy of 25 kJ mol^{-1} can be found [135]. This difference can be explained by assuming that both samples are to a large extent in a supercooled SmA phase before the experiment and only a little part of it is actually crystalline. One must further take into account that what on a first glance looks like crystallisation peaks in the cooling runs are in fact artefacts of the measurement due to instrumental problems (also it would be thermodynamically impossible that melting occurs at a lower temperature than crystallisation, while the

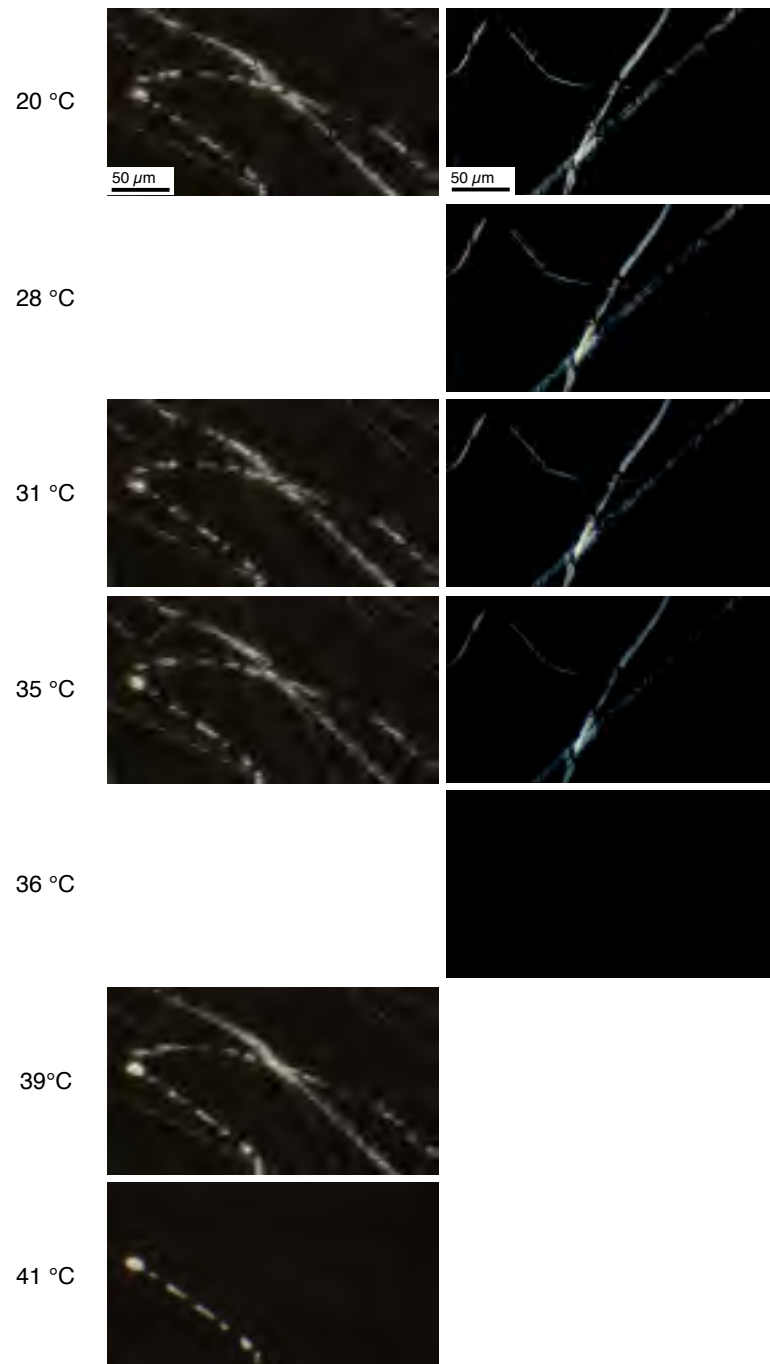


Figure 5.3: POM photos of two different areas of the first 8CB-PVP composite fibres on heating. The SmA – N transition is only visible in the thick fibre in the left column as a stepwise reduction of defects between 31 and 39 °C. The clearing transition has also extended over a temperature broad range.

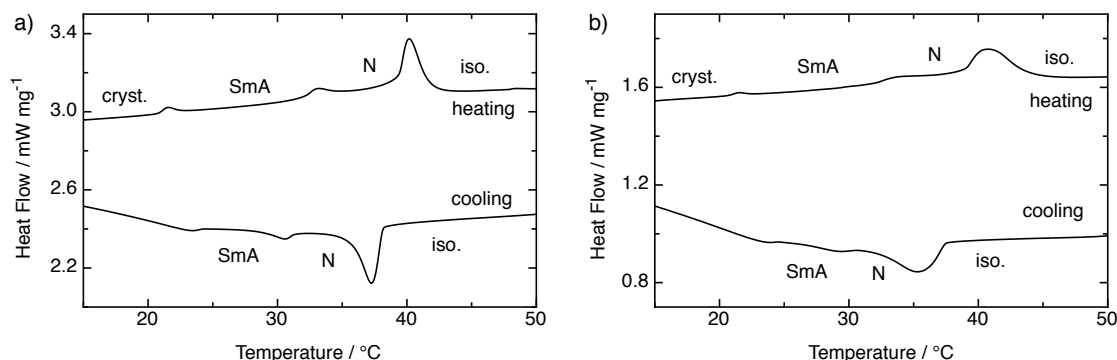


Figure 5.4: DSC thermograms of bulk 8CB (a) and the fibres with 8CB core (b) for comparison.

opposite supercooling effect is well known). By prolonging the stabilisation time at the starting temperature before the experiment or by applying a slower cooling rate maybe a (more) complete crystallisation could have been reached. Finally one should mention that the amount of 8CB in the fibre could not be calculated from these DSC results as was possible for 5CB. First, because of this incomplete crystallisation and second, also a calculation from the clearing peak is unreliable because of its overlap with the SmA – N transition.

5.2.1 X-Ray Investigations on Fibres

In order to assure that all the phases of the bulk 8CB were also present in the fibre as suggested by the DSC data and to find out if one can at all investigate the properties of liquid crystals inside such an electrospun composite fibre by X-ray scattering several experiments were made. In a first attempt a nonwoven mat was used that had to be densely packed to get enough scattering intensity.

As one can see in the first diffraction pattern in fig. 5.5a at room temperature an inner sharp ring and two diffuse rings in the middle and wide angle region were found. The inner ring at scattering angle $2\theta = 2.8^\circ$, corresponding to a periodicity of 3.08 nm, can be attributed to the layer spacing of the SmA phase when comparing to the value of 3.14 nm measured for bulk 8CB (cf. fig. 5.5b and fig. 5.6d) and to literature values [136, 137]. The middle and outer diffuse ring (corresponding to periodicities of about 0.8 and 0.4 nm) can be explained by scattering of the PVP sheath, since these are also found in fibres of pure PVP (compare to the pattern in fig. 5.5c and to the plot in fig. 5.6d). The higher intensity of the outer ring in the composite fibre in comparison to the pure PVP fibre is due to the overlaid diffuse scattering of the liquid-like distributed lateral distance between the LC molecules.

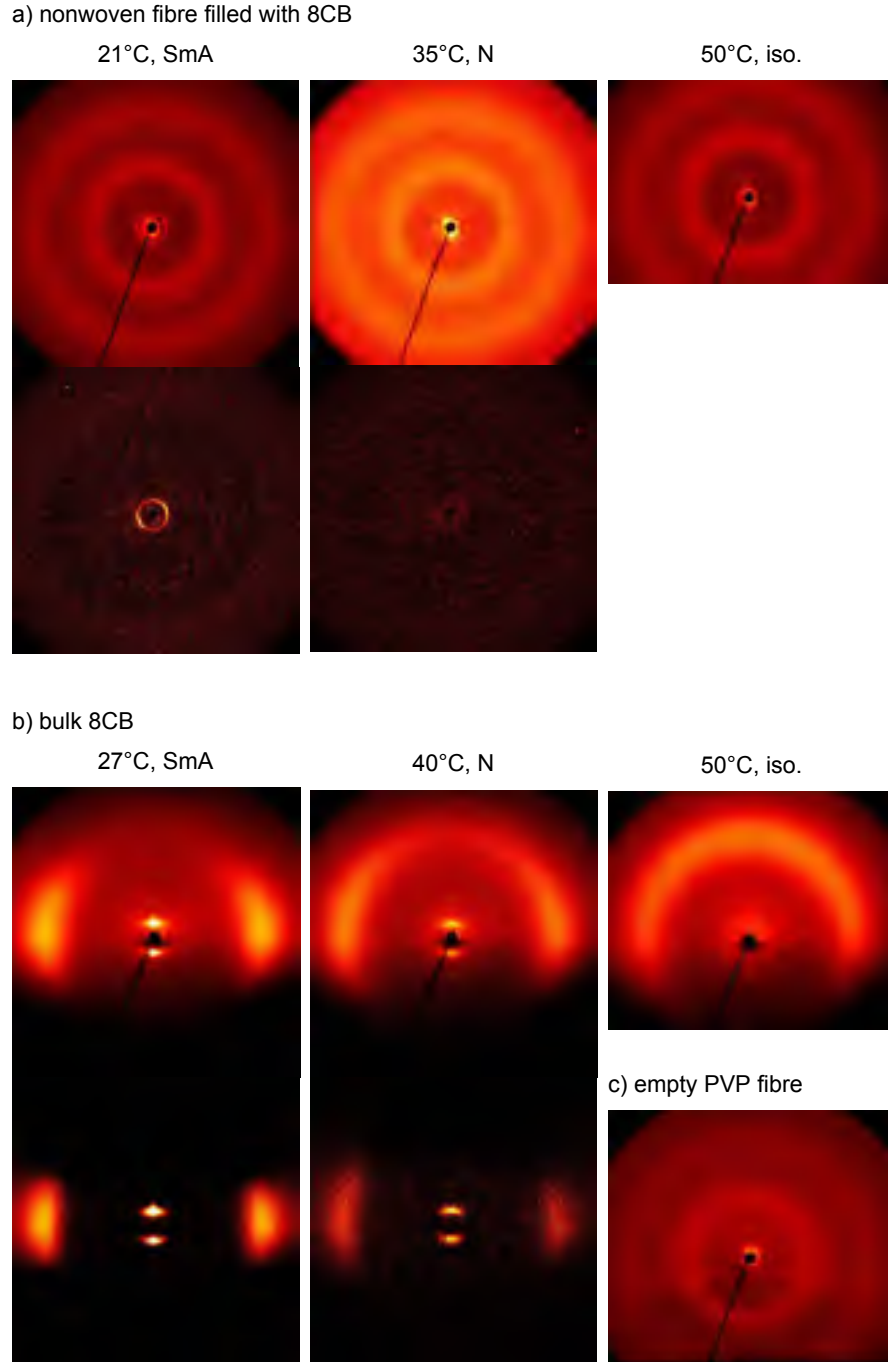


Figure 5.5: Results of the X-ray measurements on 8CB-PVP composite fibres, bulk 8CB and empty PVP fibres, part 1: 2D X-ray diffraction patterns for different temperatures. Upper patterns: original scattering intensity $I(T)$. Lower patterns: $I(T) - I(iso.)$, scattering intensity after subtraction of the scattering of the isotropic liquid to enhance the effect of the anisotropic distributions.

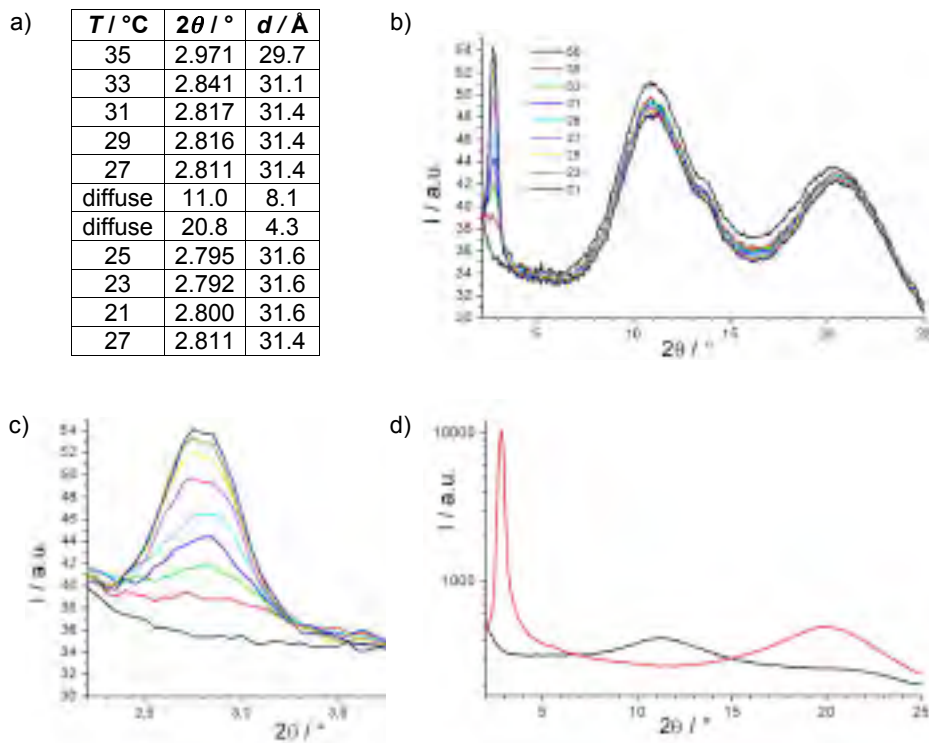


Figure 5.6: Results of the X-ray measurements on 8CB-PVP composite fibres, part 2: Θ -scans on cooling. (a) Table of maxima in the scattering angle 2Θ and corresponding distances d for different temperatures, (b) Θ -scans of filled fibres as function of temperature, (c) small angle region of Θ -scan (colour code as in b), (d) Θ -scans of unfilled PVP fibres (black) and of bulk 8CB (red).

To investigate the sample above room temperature it was inserted into a glass capillary and placed again onto the sample holder. The capillary ensured a sufficient heat flow from the heated sample holder to the fibres. As the setup was calibrated for samples in such glass capillaries the measured temperature values can be taken as actual sample temperatures. When heating from room temperature the intensity of the inner ring decreases and turns diffuse at 35°C (middle pattern in fig. 5.5a and fig. 5.6b,c). This signifies the transformation of the layered SmA phase to the nematic phase. When heating further no more changes are observed (right pattern in fig. 5.5 and fig. 5.6b,c).

To gain also information about the orientation of the liquid crystal molecules (and the layers of the SmA phase) inside the fibres, the X-ray scattering experiment was repeated with aligned fibres (only at room temperature). They were then rolled up in two directions: perpendicular or along the fibre formation axis (compare to fig. 3.5 on page 45). From the corresponding scattering patterns in fig. 5.7a,b and the scattering intensities along χ in fig. 5.7d,e one can see that the orientation is more clearly distin-

guishable for the sample rolled perpendicular to the fibre formation axis than for the other. We explain this by the facts that the roll up direction can be better controlled in the first case and that furthermore in the second case the X-ray beam is directed along rather than across the fibres in a large part of the sample, thereby not producing any significant scattering response.

For the perpendicular rolling the layer reflections of the SmA phase in the small angle region can be seen on the equator of the 2D pattern. The diffuse pattern of the lateral molecule distances appears perpendicular to it on the meridian. The scattering angles and so also the distances calculated from them are the same as in the previous discussed sample. When considering the orientation of the fibres with respect to the incident X-ray beam the finding of layer reflections on the equator and of transverse spacing peaks on the meridian leads to a model, in which the smectic layers are arranged perpendicular to the fibre formation axis, as illustrated in fig. 5.8.

This was at first somewhat unexpected, since the fibres are spun at a temperature at which the liquid crystal is in its smectic phase, in which the lowest shear viscosity is along the layers and not perpendicular to them. When taking into account only the shear flow [138, 139] one would thus expect concentric layers extended along the fibre axis in contrast to our experimental results. However shear flow is actually negligible during electrospinning which is dominated by strong stretching along the fibre formation axis due to the electrostatic forces. For this process the elongational viscosity is the relevant parameter and this may have a different anisotropy. Also the interaction with the inner PVP sheath surface has a strong influence on the orientation of the LC molecules, as indicated by the fact that the LC texture sometimes changes spontaneously within the stable fibres after electrospinning. The most beneficial alignment during electrospinning thus does not have to be the one remaining stable in the fibres.

5.2.2 Fibre Morphology and Phase Transitions of the LC in Correlation to electrospinning Conditions

To investigate the effect of different strength of encapsulation to the LC in the fibres, a series of fibres were produced with varying LC flow rate \dot{V}_{LC} while the other parameters were kept constant. For spinning the sheath the 12.5 wt.% PVP-solution at a flow rate of 1.8 ml h^{-1} was used. The pressure applied to the LC at room temperature was increased in 100 mbar steps from 100 to 900 mbar, corresponding to flow rates of 5, 20, 45, 70, 115, 145, 190 and $215 \mu\text{l h}^{-1}$, as was plotted in fig. 3.4 on page 42. Microscopy photos of characteristic examples of the produced fibres can be seen in fig. 5.9. From the optical microscopy also the fibre diameters were determined and plotted in fig. 5.10. As there are not only the mean diameters, but also minimal and maximal values are plotted, one can see that with higher LC flow rates a broader range of diameters is found, a phenomenon that will be explained below.

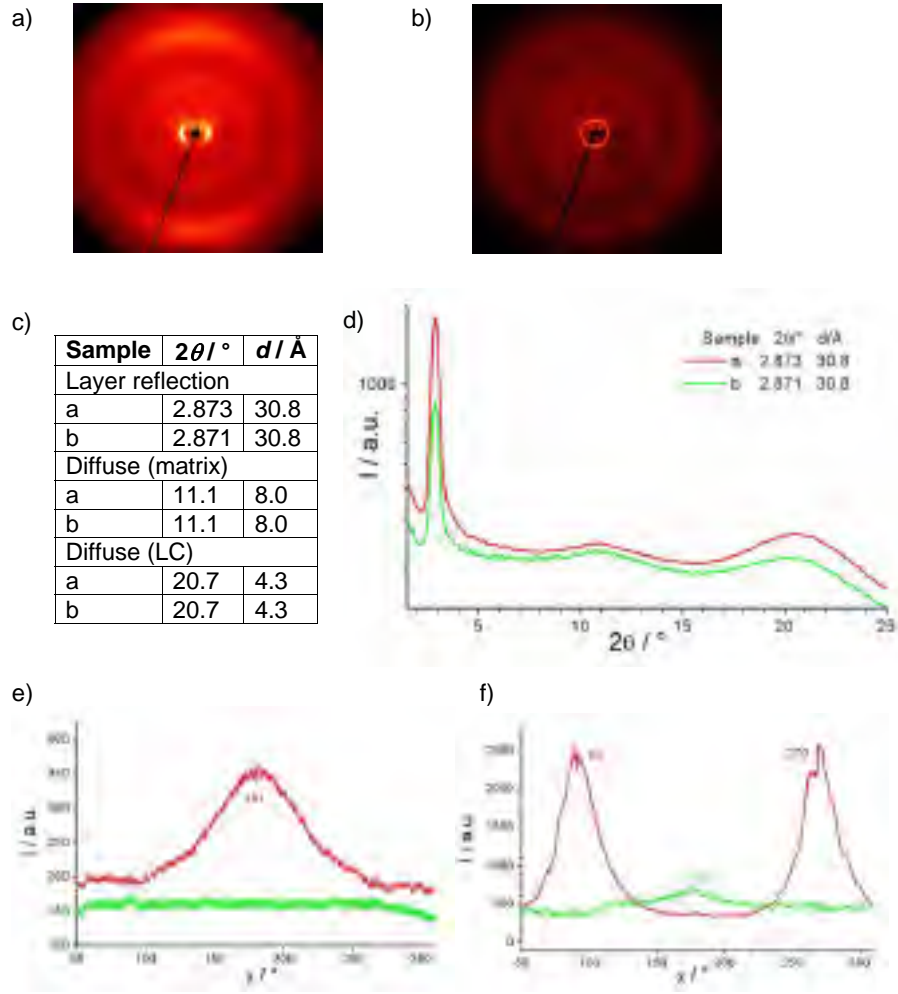


Figure 5.7: Results of the X-ray measurements on oriented 8CB-PVP composite fibres. 2D X-ray diffraction patterns of fibres rolled up perpendicular (a) and along (b) the fibre formation axis, as was schematically sketched in fig. 3.5 on page 45. (c) Table with the maxima of the Θ -scans and corresponding d -values for the two patterns. (d) Θ -scans for the two orientations. (e, f) χ -scans for the outer diffuse scattering and for the layer reflections, respectively.

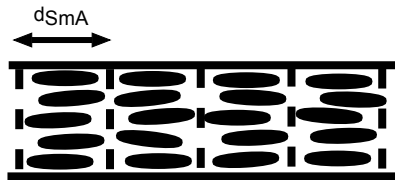


Figure 5.8: Sketch of the arrangement of LC molecules and the smectic layers in an electro-spun fibre as resulting from the X-ray experiments.

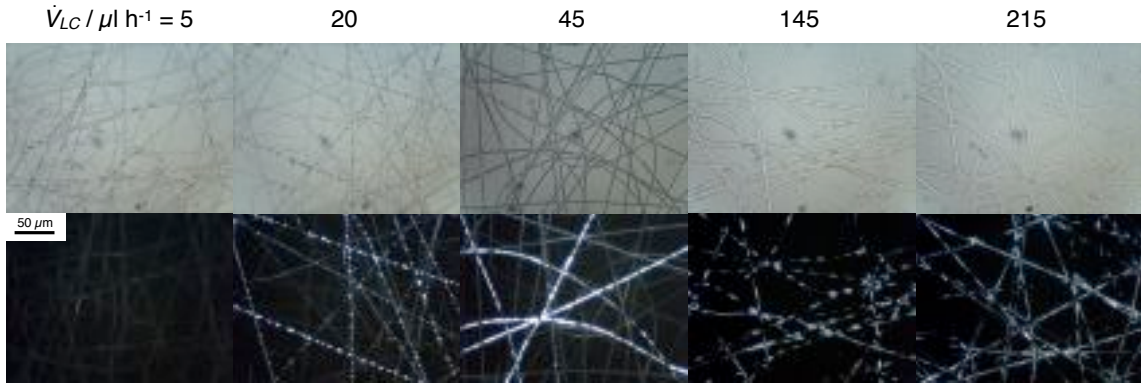


Figure 5.9: Microscopy photographs of characteristic samples when varying the flow rate of the liquid crystal \dot{V}_{LC} , while retaining the flow rate of the polymer solution constant. Upper row: sample seen without polarisers; lower row: same sample position seen between crossed polarisers. From ref. [140].

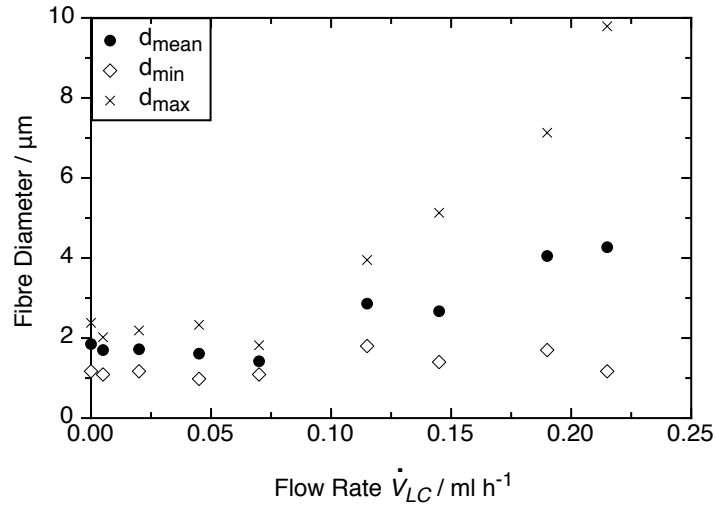


Figure 5.10: Outer fibre diameters as a function of LC flow rate as determined from 50 measurements by optical microscopy on each sample. From ref. [140].

In a first regime from the smallest flow rate up to $70 \mu\text{l h}^{-1}$ the outer fibre diameter of around $2 \mu\text{m}$ is unchanged within the accuracy of this kind of measurement from optical microscopy. At the beginning only a few fibres contain liquid crystal and it appears as small separated droplets which transform to elongated segments with increasing flow rate. In the second regime from around $100 \mu\text{l h}^{-1}$ all fibres, except some very thin ones, are (partially) filled and now also the fibre diameters grow substantially with the flow rate. At points where many fibres meet they fuse and in a last regime from about $175 \mu\text{l h}^{-1}$ this tendency increases further up to the very smeared-out morphology in the last picture shown.

The transformation of the LC core from droplets to segments and finally a complete filling of the fibres with increasing flow rate will turn out as a common behaviour of the LCs studied in this thesis if a sheath of pure PVP is used (for sheaths of a PVP-TiO₂ composite a different behaviour is observed as discussed in chapter 6.3). And so it should be discussed what the origin of this separation into droplets can be since one could as well expect a continuous thinning of the cylindrical core formed at the beginning of the coaxial electrospinning process. If this separation would happen already during the fibre formation, a beaded outer fibre morphology [141] or even a complete separation into filled droplets and unfilled fibres [126] would be the most likely results as was found for the combination of mineral oil in a PVP sheath. This means that in these cases the break-up of the non-liquid crystalline core resulted in a serious deformation of the still very fluid outer sheath.

The different behaviour in the two mentioned studies might be caused by slight differences in both the core and sheath materials (or a combination of both): First, physical properties of the used oils as e.g. viscosity and surface tension are only given in [141] and are therefore not comparable. Secondly, in [141] *N,N*-dimethylformamide was used as solvent for the PVP, while in [126] ethanol was used. As it was also shown in [126] that the break-up could be prevented by the use of a composite TiO₂/PVP sheath instead of pure PVP without changes in the core fluid, one must conclude that the exact properties of the outer solution play a major role.

But the described morphologies (beading or complete break-up) were *never* observed for the coaxial fibres with LC core of this thesis. The explanation seems to lie in the extraordinary properties of the liquid crystals. Even though their single molecules are low-molecular-mass compounds like the oil in the cited studies, the macroscopic behaviour of a LC phase in one hereby very important aspect resembles the outer polymer solution: they are both non-Newtonian fluids, i.e. relatively long filaments can be drawn from them. In contrast, Newtonian fluids, to which most low-molecular mass compounds belong, would rapidly separate into droplets due to the Plateau-Rayleigh instability. The rapid stretching process to which the inner fluid is subjected during the spinning process, can therefore be followed much better by an LC core than by an oil core. But

if the argumentation up to now is true, the visible separation of the core into droplets must occur when the fibre formation is (almost) finished and cannot affect the sheath morphology to a larger extent any more.

This correlates with the observation that sometimes flow within the liquid crystalline core could be detected directly after deposition. At least for thicker fibres this was clearly visible in the optical microscope as spontaneous textural changes that could in some cases also be initiated by knocking onto the side of the glass slide with a spatula. This means that initially a thin but continuous inner core is formed in the spinning process, which is then in the fibre transformed into the droplet morphology in order to reduce the interfacial area between the nonpolar LC and the polar sheath polymer. This would require that the sheath still contains a sufficient amount of solvent to be soft enough to accommodate for a slight morphology change, an assumption that is not unreasonable directly after fibre deposition. In contrast such a flowing behaviour of the core was not observed for fibres with PVP-TiO₂ composite sheath. Instead in this case non-moving LC droplets were formed even for the highest investigated LC flow rates. The droplet formation can be explained by unmatched elongational viscosities between core and sheath during spinning while the non-existence of LC flow after deposition can be explained by the faster and stronger onset of sheath rigidity.

A different picture must be drawn however for the smeared-out fibres in the last regime obtained for the highest LC flow rates. When taking into account the knowledge on fibre morphology gained later from the SEM measurements on N*-LC-filled PVP fibres (chapter 6.3) one must consider that these fibres may actually not be fibres with a regular circular cross section but rather semi-cylinders on the glass surface, as sketched below in fig. 5.11b. It seems that with increasing LC loading surrounded by the same amount of polymer (the outer flow rate was kept constant !), a situation that must lead to a decrease of sheath thickness, the fibres get soft and the elastic cylindrical sheath (especially in comparison to a sheath containing the more rigid TiO₂) can deform when the fibre hits the substrate. Wetting of the substrate by the polymer solution most likely also contributes to this deformation.

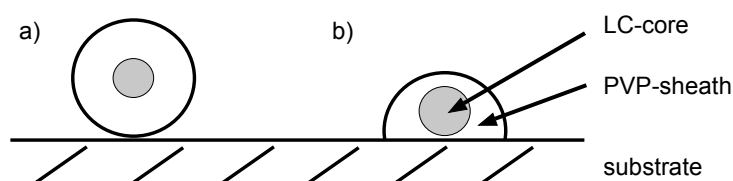


Figure 5.11: Schematic drawing of cross sections through fibres with small and large core, described as regime 1 and 3 in the text. In (a) the fibre forms a stable, regular cylinder, but with a larger core (b), corresponding to a thinner sheath, it can deform into a half-cylinder on the substrate.

Maybe one could obtain stable structures even at that high flow rates if the fibres would first be produced as freely suspended mat and transferred to a substrate later, avoiding that the fibres hit the substrate with high velocity and in a still slightly wet state. Note that the liquid crystal nevertheless is still encapsulated in channel-like structures along the fibres as visible in the POM photos. On the other hand there are still some unfilled parts (invisible through crossed polarisers, but visible without them) that do not have this smeared-out morphology but look like the fibres of regime one. These fibres correspond to the minimal diameters in fig. 5.10, while the smeared-out fibres correspond to the maximal diameters.

DSC thermograms of the discussed fibres are presented in fig. 5.12, as well as again the thermogram of bulk 8CB for comparison. The effect of confinement on the LC phase sequence can be clearly seen. For the higher flow rates the DSC is similar to the one already discussed in fig. 5.4. The clearing peak is broadened and its end shifted towards higher temperatures, but the variations between the samples are only small when decreasing from 215 to 115 $\mu\text{l h}^{-1}$. The smectic to nematic transition is shifted to higher temperatures with decreasing LC content until it finally disappears completely in the last shown sample (5 $\mu\text{l h}^{-1}$). During this process the shape of this transition in the thermogram transforms continuously from a peak in the bulk sample to a step, signifying a change from (weakly) first- to second-order character of the transition.

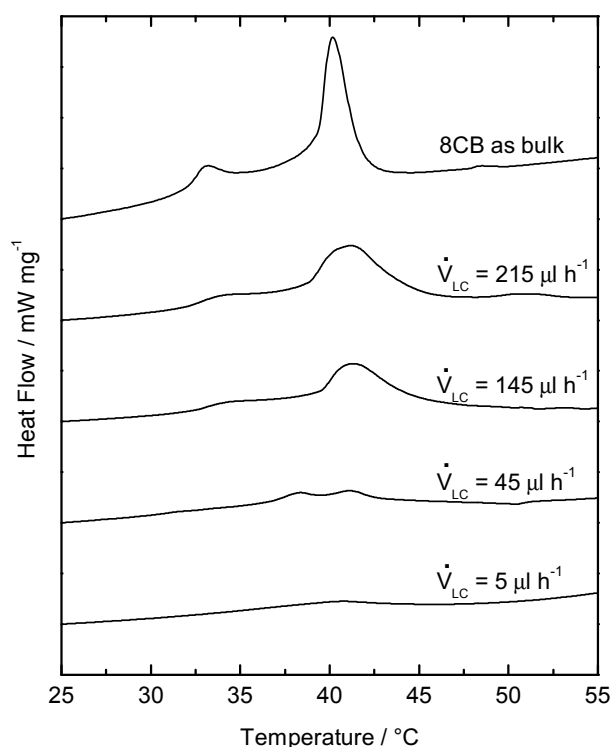


Figure 5.12: Staggered plots of DSC thermograms on heating of 8CB as bulk and as inclusion compound in PVP fibres produced with different LC flow rates \dot{V}_{LC} . From ref. [140].

Another remarkable effect is that in the thermograms obtained for samples spun with $\dot{V}_{LC} = 20, 45$ and $70 \mu\text{l h}^{-1}$ during a first heating experiment the SmA – N as well as the clearing transition were visible, but in the cooling and a directly subsequent second heating experiment only one transition was found (cf. fig. 5.13a – c). Even though it was shifted towards lower temperatures this is interpreted as the clearing transition, which was also confirmed by POM observation of a reduced clearing temperature in a heating experiment directly after having heated and cooled the sample quickly from room temperature to the isotropic state and back. The original phase sequence is retained when repeating the experiment after several weeks with the sample kept at room temperature, as can be seen by comparing fig. 5.13c and (d).

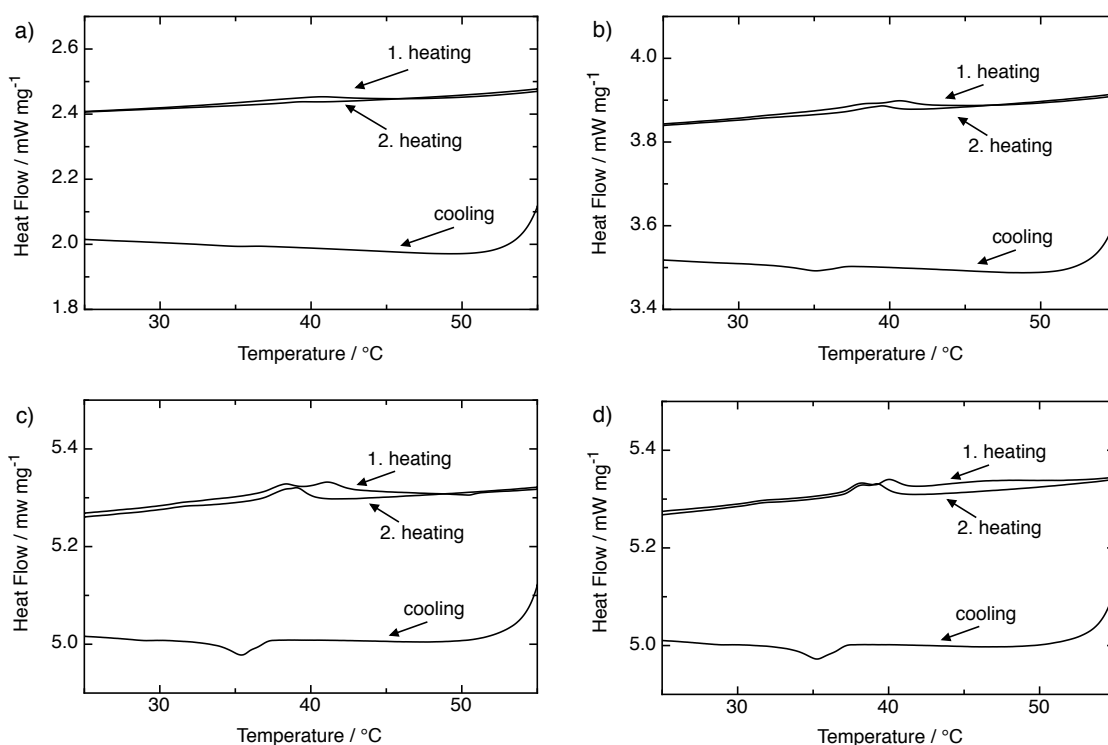


Figure 5.13: a – c) DSC-thermograms of composite fibres spun with $\dot{V}_{LC} = 20, 45$ and $70 \mu\text{l h}^{-1}$ showing a heating run with a directly subsequent cooling and second heating run. d) Repetition of the experiment of (c) after 1 month with the same sample that had been stored at room temperature.

When considering the X-ray results leading to a model with the mesogen molecules oriented along the inner surface of the polymer sheath, these DSC observations suggest a strong supercooling effect of the nematic phase: the transformation from the nematic to smectic phase on cooling is kinetically hindered in the encapsulated liquid crystal because

of the anchoring to the polymer sheath that prevents a rearrangement of the molecules to the layered smectic structure even though it is the thermodynamically stable phase at room temperature. With the same model the increase of the SmA – N transition temperatures in the first heating with decreased fibre diameter can be explained: if the smectic phase is present in the fibre the layer geometry will be retained even when the temperature is raised somewhat above that where a bulk sample goes nematic, because the mesogens at the inner sheath surface are anchored in the smectic configuration, with 1D positional order. The extreme surface-to-volume ratio in a thin fibre gives these surface molecules a much stronger influence on the whole sample behaviour than normally expected. Especially for the thinnest fibres with essentially the same diameter as an unfilled fibre, corresponding to a very small core diameter with only a small fraction of the LC molecules not affected directly by the polymer surface, such strong effects can be expected.

Besides the flow rates of inner as well as outer solution and the concentration of the polymer solution, also the electric field strength applied during electrospinning can affect the result. So another series of experiments was made, starting with the already discussed system with $\dot{V}_{LC} = 70 \mu\text{l h}^{-1}$ and $\dot{V}_{out} = 1.8 \text{ ml h}^{-1}$ in which now voltages of 10, 12.5, 15 and 17.5 kV were applied (over a spinneret – collector distance of 10 cm). In a second series the same field variation was done with fibres of outer flow rate of 3.0 ml h^{-1} and finally a third series with a polymer concentration 15 wt.% was produced. Fig. 5.14 and 5.15 show microscopy photos and mean fibre diameters of these fibres.

In the POM photos one can see how the texture of the LC core changes with increased field strength. In the upper row a smooth inner core is achieved at a voltage of 12.5 kV, while with increased outer flow rate a voltage of 15 kV is required. At even higher voltages the filling gets non-uniform again and it becomes more and more difficult to acquire a homogenous fibre mat. The first part of that behaviour had been predicted in a numerical study on flow patterns in coaxial electrospinning [142]: annular flows with smooth core-sheath interfaces should appear only above a certain threshold level of the electrical field strength. The generally observed reduction of fibre diameter upon increasing field strength had been found in the special case of coaxial electrospinning not to be coupled to any substantial decrease in wall thickness [126]. This means that the reduction of total fibre diameter would be almost completely given by a reduction of core thickness.

In the fibres presented here, the outer fibre diameters, measured by optical microscopy, show an almost linear reduction with increasing voltage for all three series. The possible reduction due to increased voltage is in all cases in the range of $0.5 \mu\text{m}$. A rather small variation in comparison to the other parameters, inner and outer flow rate and polymer concentration, studied in this series (compare to fig. 5.10 and fig. 5.15). One contribution might be that the inner flow rate chosen for this series of increasing voltage

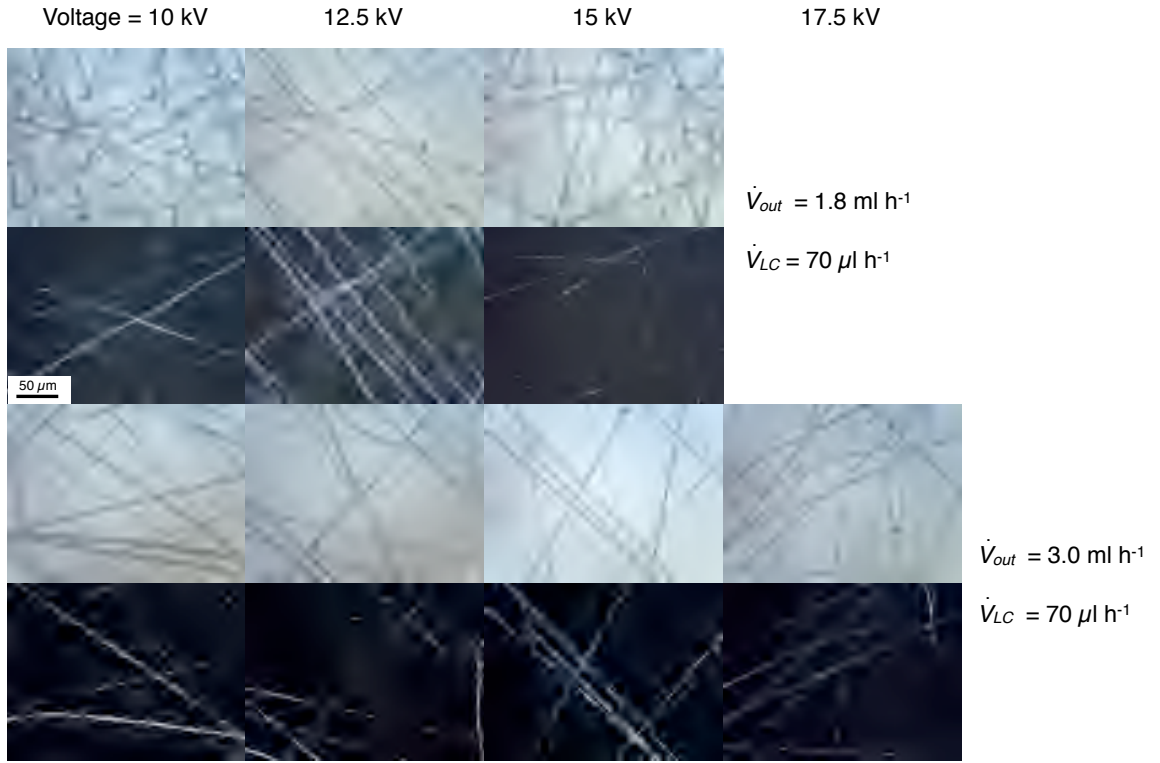


Figure 5.14: The liquid crystal core shows a transformation from bubbly to smooth and to bubbly again with increasing electric field strength, the threshold voltage being dependent on the ratio of outer to inner flow rate. From ref. [140].

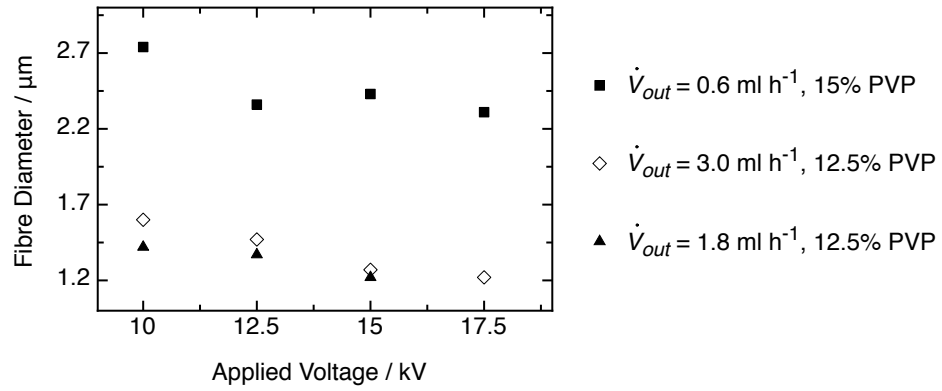


Figure 5.15: Influence of the applied voltage and the flow rate of the polymer solution on the mean fibre diameter.

is in the range for resulting in small diameters anyway so that a much further reduction is not possible as the core cannot be further compressed. When measuring DSC on these samples, for *all* of them almost identical transition temperatures and phase behaviour was found. Some, but not all of them are shown in fig. 5.16. This observation suggests that for fibres in the μm range, as were studied in this thesis, the effect of electric field strength variations on the inner diameter is in fact almost negligible, in contrast to the cited literature with fibres in the sub- μm range.

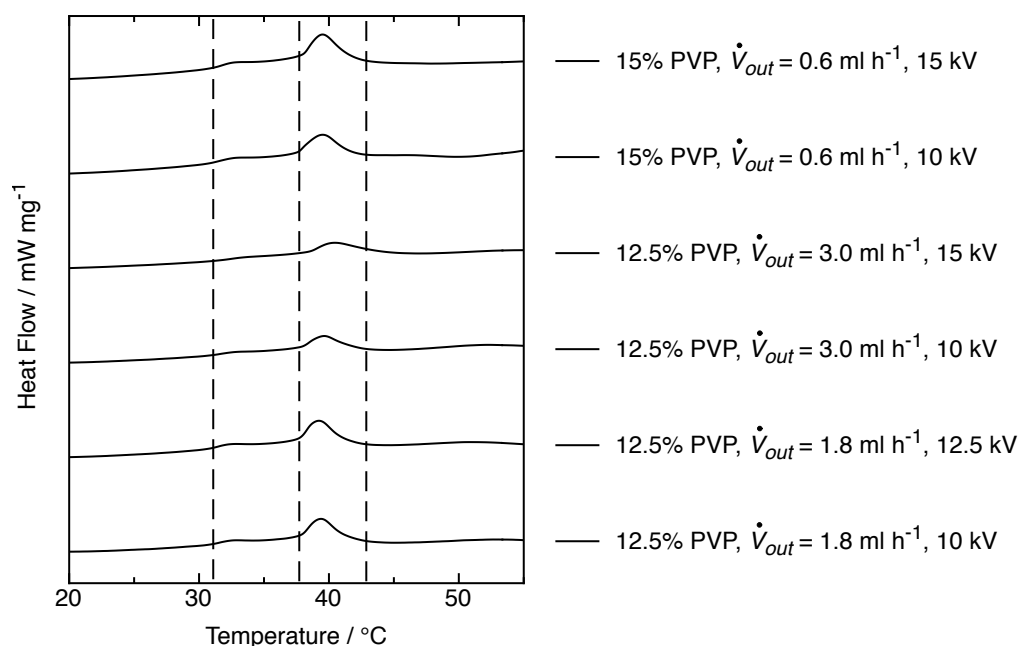


Figure 5.16: A selection of DSC thermograms (as staggered plot) of the fibres, whose diameters were plotted in fig. 5.15.

5.3 Further Extension to the tilted Smectic C Phase

5.3.1 Characterisation of the bulk LC Mixture

For the investigations described in this part a liquid crystal material was needed with a SmC phase and crystallisation below room temperature (it had been found that for well filled fibres crystallisation can destroy the fibre structure, see the short discussion of fibres filled with CB15/6OCB at the beginning of chapter 6.1). To achieve this a mixture was prepared of two phenylpyrimidine mesogens, 6OPhPy8 and 8OPhPy8 (chemical structure: see experimental part, fig. 3.3), that themselves have a phase sequence of

SmC – SmA – N – iso., but crystallisation around 30 °C. A theoretical melting diagram on mixing these two compounds was calculated with the Schröder – van Laar equation [143, 144]:

$$T_m = \frac{1}{\frac{1}{T_m^*} - \frac{R}{\Delta H_m^*} \ln x} \quad (5.1)$$

With this equation the reduced melting point T_m of a substance in a mixture is calculated from the melting temperature T_m^* and melting enthalpy ΔH_m^* of the pure substance, its molar fraction x and the gas constant R . When plotting this function for both components of a binary system, the eutectic point in the melting diagram can be found. Using this method one must take into account that the equation is based on thermodynamic ideal mixing, so that the calculated values are in general only approximations to the actual melting diagram. By DSC measurements $T_m^* = 302$ K, $\Delta H_m^* = 27.7$ kJ mol⁻¹ and $T_m^* = 303$ K, $\Delta H_m^* = 35.5$ kJ mol⁻¹ were determined for 6OPhPy8 and 8OPhPy8, respectively. Using these values the diagram in fig. 5.17 is established with a eutectic composition of $x_{6OPhPy8} = 0.55$ (corresponding to 53 wt.%) and a melting point of 13 °C.

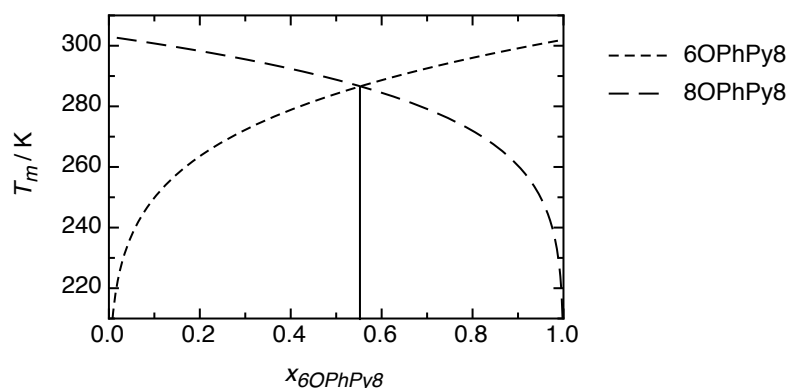


Figure 5.17: Predicted melting temperatures as function of composition for the binary system 6OPhPy8/8OPhPy8, calculated by the Schroeder – van Laar equation (cf. eqn. 5.1 in the main text).

With a mixture of 50/50 by weight of each compound a phase sequence of SmC 49.7 SmA 59.8 N 67.9 iso./°C was obtained. The presence of the SmC phase could be verified in POM investigations on the one hand by observing the LC in homeotropic alignment in which the SmA and N phase appear optically isotropic while the tilted phase shows birefringence. On the other hand in planar alignment all three liquid crystalline phases show birefringence and typical textures and also the transitions between them could be observed. The exact transition temperatures were obtained by DSC investigations (cf. fig. 5.18).

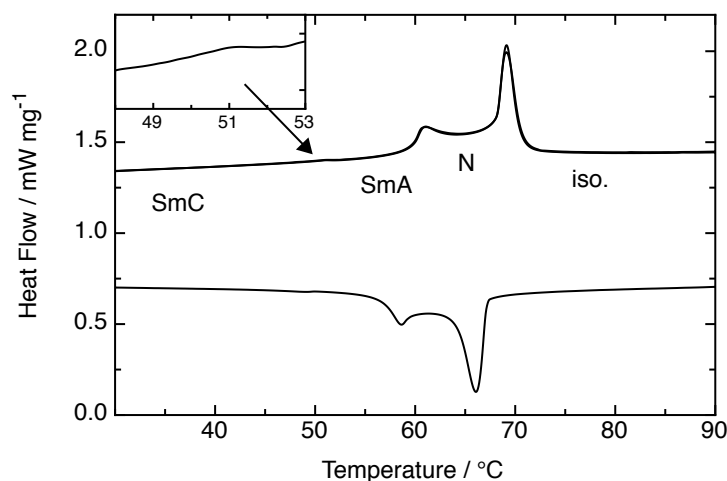


Figure 5.18: DSC thermogram of the 50/50 mixture of 6OPhPy8/8OPhPy8.

The SmC – SmA transition peak is very small, as expected for this second order phase transition. The crystallisation temperature was not determined, but when storing the samples at room temperature (bulk material as well as in the fibres) no crystallisation was observed. This room temperature SmC liquid crystal mixture (RT-SmC-LC) was furthermore studied with X-ray scattering which also confirmed this phase sequence (fig. 5.19 and fig. 5.20). The 2D patterns of a surface aligned sample are similar to those already described for 8CB: two diffuse maxima on the equator in the wide angle region and two sharper, temperature dependent maxima on the meridian in the small angle region.

On cooling from the isotropic liquid (no alignment, the inner diffuse scattering has approximately the same intensity as the outer one; not shown in fig. 5.19) cybotactic groups appear which develop into a nematic phase (maximum of the outer diffuse scattering on the equator of the pattern, halos of the inner diffuse scattering with their maxima on the meridian which become more and more intense with decreasing T). On further cooling the inner scattering turns into sharp reflections on the meridian, whereas the outer scattering stays diffuse and on the equator. This pattern is typical for a smectic phase and does not change drastically on further cooling. But the dependence of the layer spacing d from temperature shows the appearance of a SmC phase below the SmA phase: d is almost constant at high temperature (or even slightly increasing with decreasing temperature) but decreases with T in the low temperature phase. The latter can be explained by an increasing average tilt of the molecular axes in a SmC phase. In the SmA phase the scattering angle corresponds to a layer spacing of 2.83 nm which

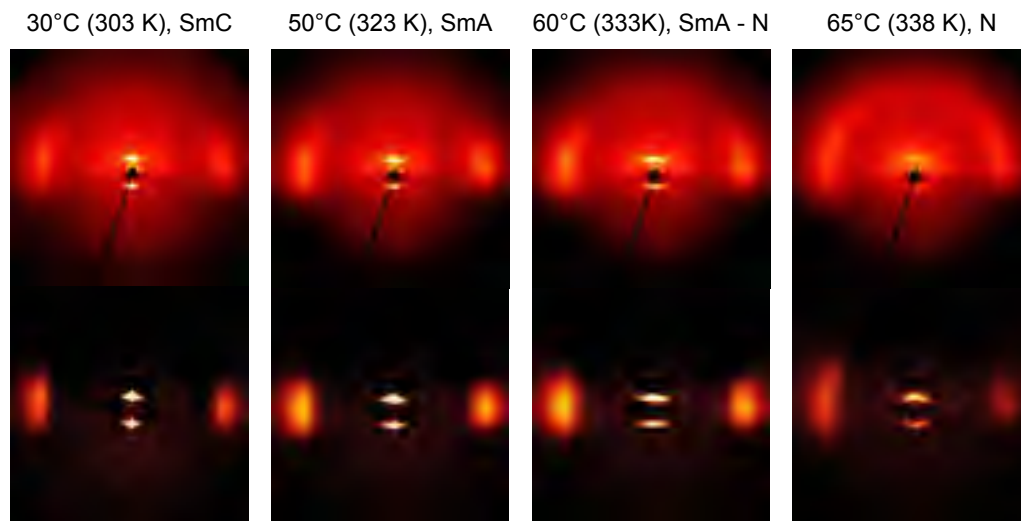


Figure 5.19: Results of the X-ray measurements on the bulk RT-SmC-LC mixture, part 1: 2D X-ray diffraction patterns for different temperatures. Upper pattern: original; lower pattern: $I(T) - I(iso.)$.

decreases to 2.70 nm at 30 °C. The tilt angles in the SmC phase, estimated according to $\tau = \arccos(d_{SmC}/d_{SmA})$, increase from the phase transition to room temperature up to about 17 °.

5.3.2 Fibres with this Core Material

In contrast to the previously described experiments, for these fibres a new outer solution containing PVP in combination with a small amount of $Ti(O^iPr)_4$ as sol-gel-precursor was used. After complete evaporation of the solvent and hydrolysis of the precursor, fibres containing ≈ 9 wt.% TiO_2 in the sheath were the result. This relatively small amount of TiO_2 led to a more uniform and stable morphology and less elasticity of the fibres, as was studied in more detail in chapter 6.3. In the fibre series discussed here the flow rate of the outer solution was kept constant at 0.9 ml h^{-1} , while the flow rate of the preheated LC was varied stepwise from 1 to $200 \mu\text{l h}^{-1}$ (refer to table 3.1 on page 43).

As can be seen from the POM photos in fig. 5.21 the morphology of the LC core in the fibres as function of flow rate shows a similar behaviour as with 8CB. At the lowest flow rates of $\dot{V}_{LC} = 1$ and $4 \mu\text{l h}^{-1}$ only small droplets appear that turn into elongated segments at $\dot{V}_{LC} = 20 \mu\text{l h}^{-1}$ and finally an almost completely filled fibre at $\dot{V}_{LC} = 150 \mu\text{l h}^{-1}$. Surprisingly up to this very high flow rate (about 4 times of the highest investigated for 8CB) only a very small increase of outer diameter from $1.8 \pm 0.3 \mu\text{m}$ to $2.2 \pm 0.3 \mu\text{m}$ is found (cf. fig. 5.22). When increasing the flow rate even beyond that

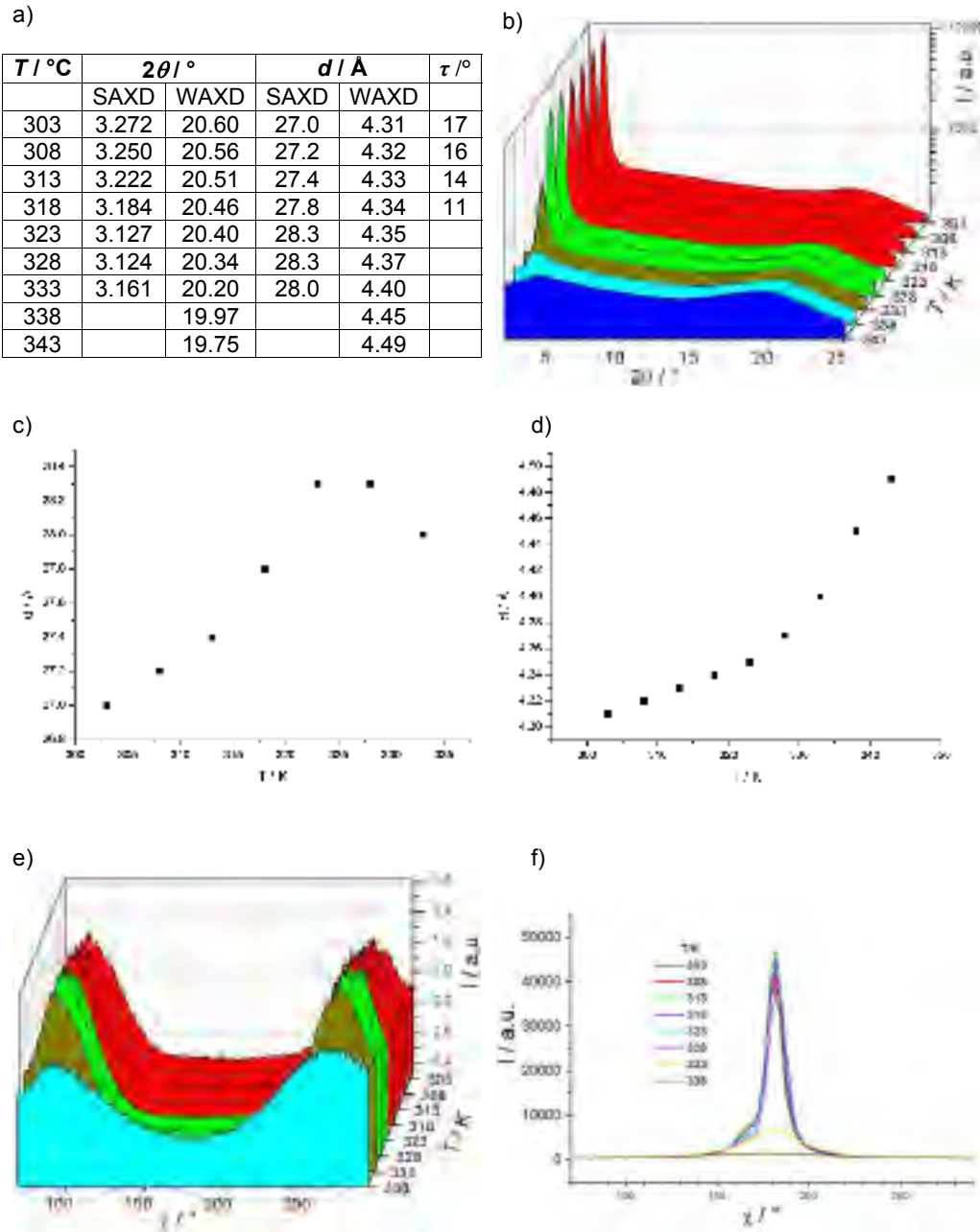


Figure 5.20: Results of the X-ray measurements on the bulk LC mixture, part 2: Θ -scans and χ -scans on cooling. (a) Table of maxima in the scattering angle 2Θ , corresponding distances d and tilt angles in the SmC phase calculated from these d -values as explained in the main text. (b) Θ -scans of filled fibres as function of temperature. Colour code: red ... SmC, green ... SmA, dark yellow ... SmA – N, cyan ... N, blue ... iso. (c) Plot of d for the maximum of SAXD. (d) Plot of d for the maximum of WAXD. (e) χ -scans for the maxima of WAXD (colour code as in b). (f) χ -scans for the maximum of SAXD.

point a sudden, drastic increase of diameter to $5.8 \pm 1.5 \mu\text{m}$ at $\dot{V}_{LC} = 200 \mu\text{l h}^{-1}$ is found and also LC on the outer surface and between the fibres is observed in the microscope. An explanation is that when too much LC reaches the orifice of the spinneret at once not all can be incorporated into the fibres and this material then forms drops deposited between the fibres. But in contrast to the experiments with 8CB even these fibres have no smeared-out morphology which shows the great stabilisation effect of the quite small amount of TiO_2 in the PVP sheath.

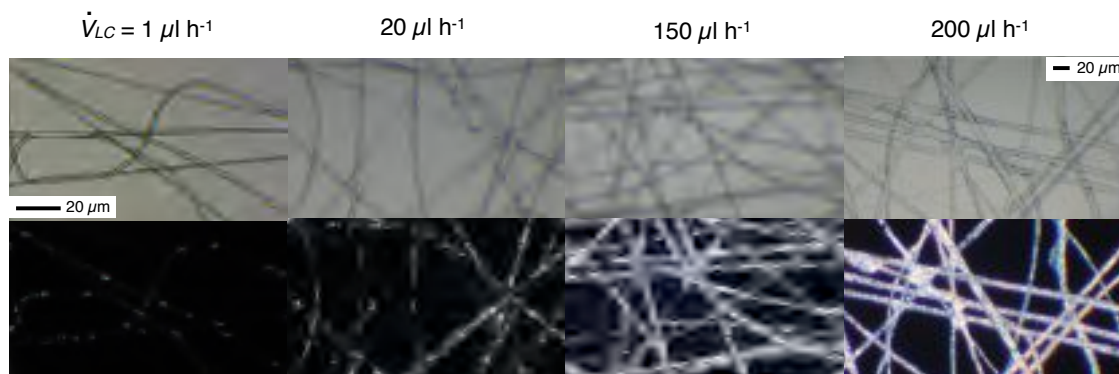


Figure 5.21: Microscopy photographs of the fibres with the RT-SmC mixture. The lower row shows the same sample area as the upper one but seen through crossed polarisers. Note the smaller scale bar for the last sample.

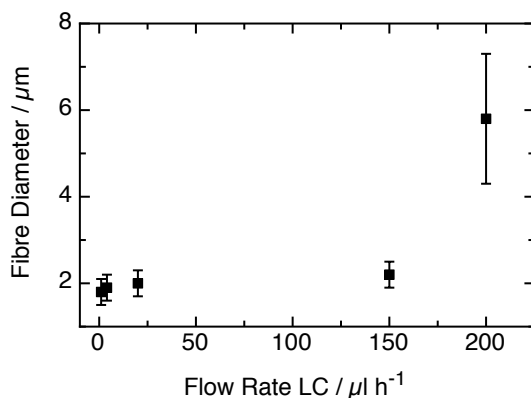


Figure 5.22: Outer fibre diameters (measured by microscopy) as a function of LC flow rate. When the fibres are completely filled at the highest flow rate a distinct increase of diameter is obtained.

Despite the similar effects on the LC core structure as for 8CB and the thin fibre diameters achieved, the encapsulation effect on the LC phase sequence in this series is rather small. In fig. 5.23 the first heating parts of the DSC thermograms measured on these fibres are shown (for the highest flow rate no DSC was measured because of the LC outside the fibres). As one can see, the SmA – N transition transforms from a peak

in the bulk, signifying a first order transition, to a kink in the fibres, signifying a second order transition, similar to the results for 8CB. The transition temperature is however not changed. For the clearing transition the peak becomes broader, but in this case the temperature at the end of the peak is unchanged with flow rate down to $20 \mu\text{l h}^{-1}$ while for thinner fibres a slight *decrease* is seen, as can be seen from the dashed lines in the diagram. For the onset temperature this decrease is seen also in the thicker fibres. The SmC – SmA transition is not detected even in the fibres with the two highest flow rates, most likely because it is already very small in the bulk (compare to fig. 5.18).

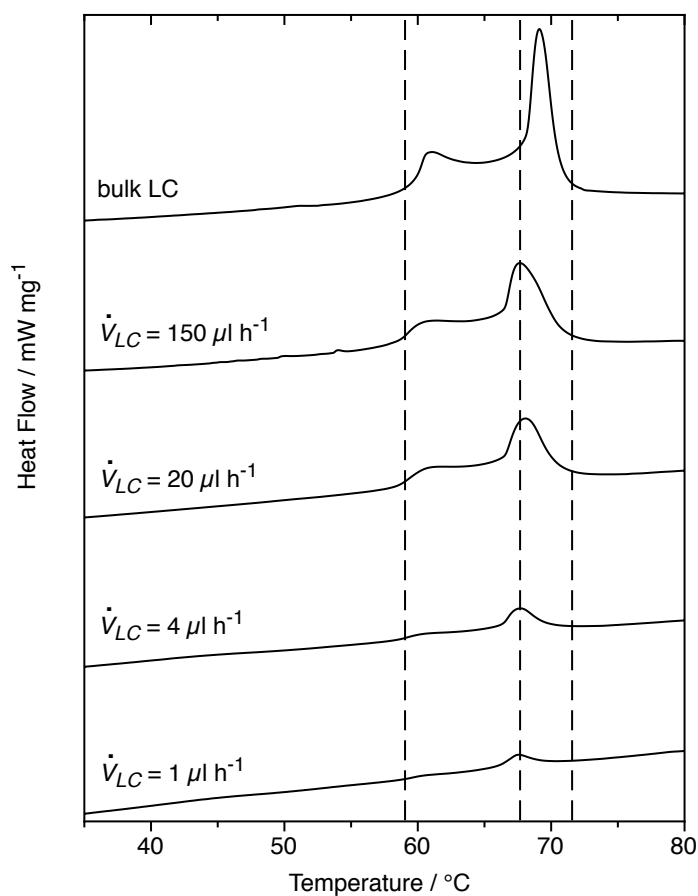


Figure 5.23: First heating parts of the DSC thermograms of the fibres and the bulk LC discussed in this section. The dashed lines correspond to the onset temperatures of the SmA – N and the onset as well as offset temperature of the clearing transition in the bulk material.

Astonishingly, for the two lowest flow rates a very broad and flat peak between 39 and 49 °C is found in the first heating part of the DSC which in the following cooling and reheating part has disappeared. Also the clearing transition is shifted by about 1 °C

towards higher temperatures in the second heating. An example is plotted in fig. 5.24. When regarding only these last thermograms one might explain this, as for 8CB, in the way that one of the phases, in this case most probably the tilted SmC phase, is not formed in the fast cooling part of the DSC measurement as it requires a shift of the LC molecules which could be prevented by the surface interaction. When observing the LC textures in the fibres with polarising microscopy no difference between the three phases are distinguishable in any of the discussed fibres, so this method also does not give an explanation. As last characterisation method X-ray scattering was conducted on the fibres with $\dot{V}_{LC} = 150 \mu\text{l h}^{-1}$. As will be discussed below, from these experiments it can be concluded that at least for these fibres the phase sequence of the LC is the same as in the bulk and the SmC – SmA is only invisible in DSC because of the smaller amount LC measured in the fibres. Unfortunately fibres with low LC content cannot be investigated with X-ray scattering since the scattering intensity of the LC core becomes too low in comparison to the scattering of the sheath.

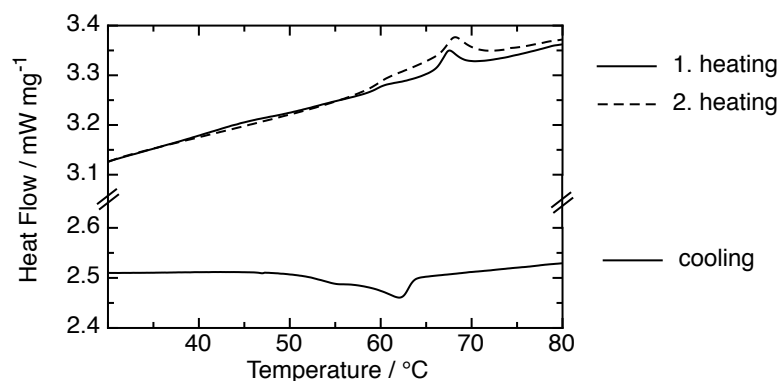


Figure 5.24: Complete DSC thermogram of the composite fibres produced at a LC flow rate of $1 \mu\text{l h}^{-1}$.

The X-ray experiments were again done on aligned fibre mats, to obtain information about the orientation of the mesogen molecules, as well as of the smectic layers, inside the fibres. As for the 8CB composite fibres, rolling perpendicular to the fibres gave a better result on that aspect. The 2D X-ray patterns in fig. 5.25 show that the molecules of the liquid crystal are aligned with their long axes parallel to the fibre formation axis, as the almost temperature independent outer diffuse scattering has its maxima on the meridian of the pattern, i.e. normal to the fibre axis, and the maxima of the inner scattering appear on the equator.

The found phase sequence is the same as for the bulk material. The general temperature shift of about 5°C to higher temperatures in the fibre (cf. fig. 5.26a) is due to experimental problems: a fibre mat hanging almost freely in the air on the sample

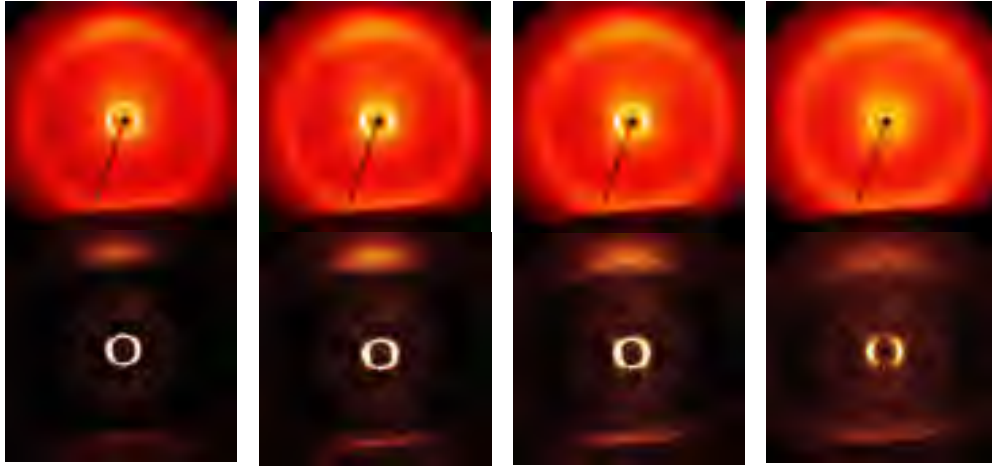
a) aligned composite fibre

30°C (303 K), SmC

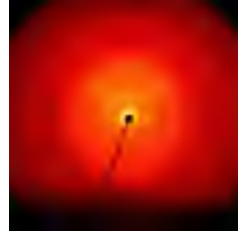
60°C (333 K), SmA

69°C (342 K), N

81°C (354 K), N – iso.



b) unfilled fibre

(PVP-TiO₂ composite)

c)

$T/^\circ\text{C}$	$2\theta/^\circ$		$d/\text{\AA}$		$\tau/^\circ$
	SAXD	WAXD	SAXD	WAXD	
303	3.335	20.52	26.5	4.33	17
308	3.320	20.45	26.6	4.34	17
313	3.298	20.33	26.8	4.37	15
318	3.273	20.30	27.0	4.37	14
323	3.239	20.24	27.3	4.39	11
328	3.186	20.21	27.7	4.39	
333	3.182	20.14	27.8	4.41	
338	3.184	20.04	27.7	4.43	
340	3.208	20.04	27.5	4.43	
342	3.298	19.99	26.8	4.44	
344	3.366	19.94	26.2	4.45	
349	3.555	19.80	24.9	4.48	
354	4.408	19.70	20.0	4.51	

d)

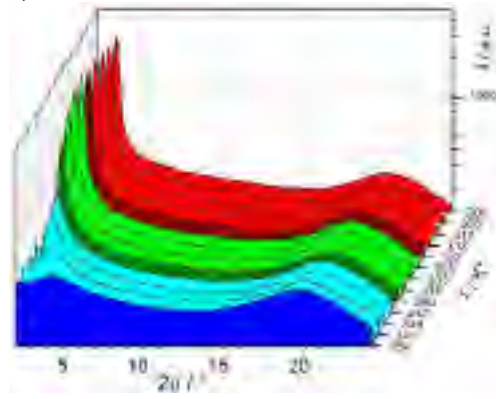


Figure 5.25: Results of the X-ray measurements (performed on cooling) on the RT-SmC-LC composite fibres, part 1. (a) 2D diffraction patterns of aligned composite fibres at different temperatures. Upper pattern: original; lower pattern: $I(T) - I(iso.)$. (b) For comparison: diffraction pattern of unfilled fibre. (c) Maxima in the scattering angle 2θ , corresponding distances d and calculated tilt angles. (d) Θ -scans of filled fibres as function of temperature. Colour code: red ... SmC, dark red ... SmC – SmA, green ... SmA, dark yellow ... SmA – N, cyan ... N, blue ... iso.

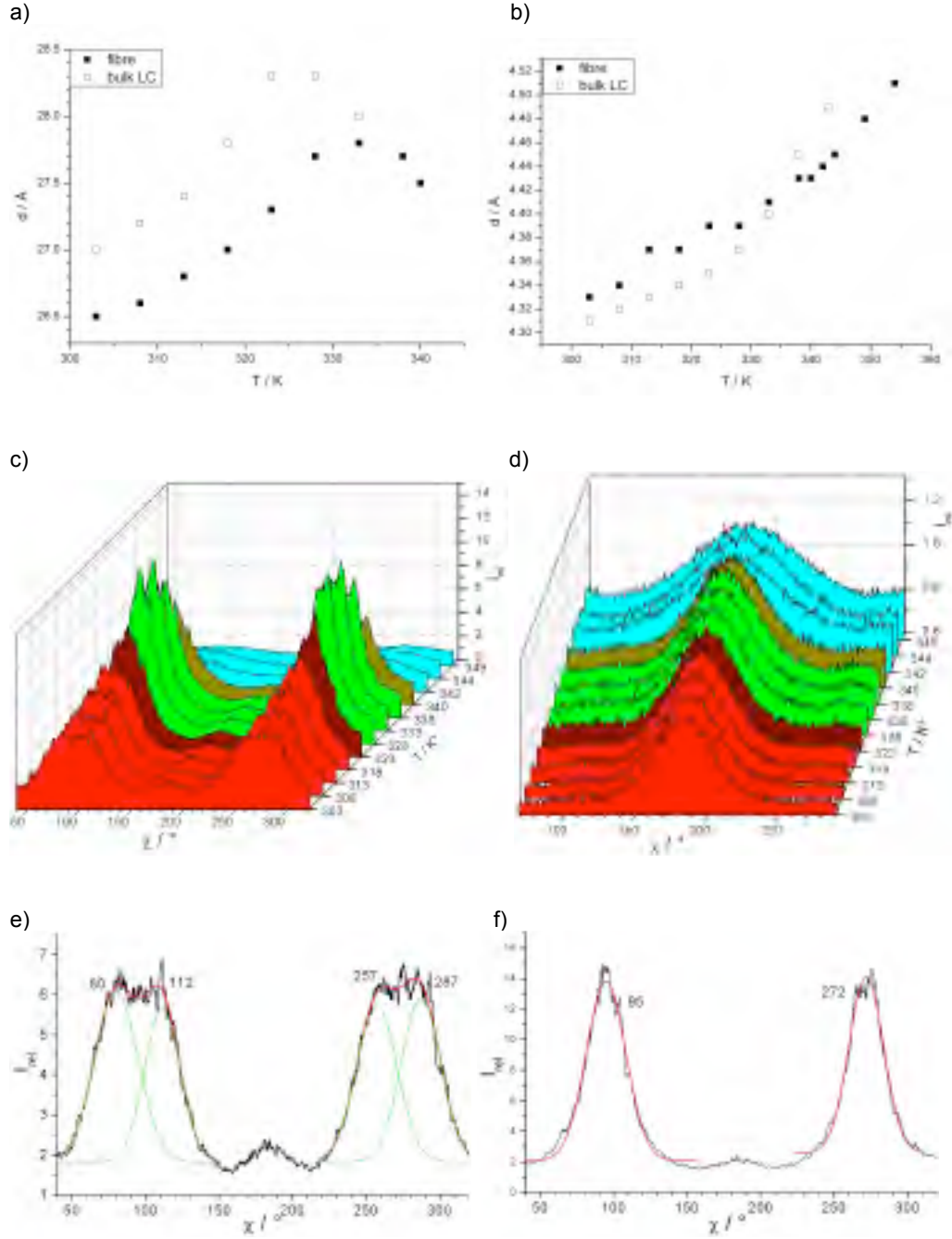


Figure 5.26: Results of the X-ray measurements (performed on cooling) on the RT-SmC-LC composite fibres, part 2. Plot of d for the maximum of SAXD (a) and WAXD (b) for the composite fibre and the bulk LC in comparison. (c, d) χ -scans for the maxima of SAXD and WAXD, respectively, colour code as in fig. 5.25. (e, f) Examples for the χ -distribution of the intensity for the layer reflection in the SmC phase at 303 K (tilt $\sim 16^\circ$) and in the SmA phase at 328 K, respectively.

holder (a sketch is found in fig. 3.5 in chapter 3.6) will always have lower temperature than a drop of LC laying on a thin glass slide placed directly on the heater. But since it was not possible to measure the actual temperature of the fibre sample it was decided to use the temperature values as they would be for a standard sample.

Below the isotropic a nematic phase with cybotactic groups appears as indicated by halos of inner diffuse scattering with maxima on the equator. On cooling this diffuse scattering condenses to a sharp ring with strong maxima on the equator of the pattern, meaning that the molecules stay parallel to the fibre axes but they are now organised in layers with the layer normal also parallel to the fibre axes, hence in a SmA phase. Like in the bulk sample, the pattern does not change much when cooling further. But carefully examining the intensity distribution of the inner ring a splitting into four main maxima can be observed (cf. fig. 5.26e). This is a hint that the average tilt of the molecules deviates significantly from zero. And also a reduction of layer spacing from 2.78 nm to 2.65 nm is found, giving a calculated tilt angle of 17° at room temperature as for the bulk mixture. When comparing the values of layer spacing as function of temperature for the fibre and the bulk LC a general reduction by 0.05 nm in the fibre is found (cf. the plot in fig. 5.26a). This shrinkage indicates that in the fibres either the orientational order is lower, giving a larger average tilt and thus smaller layer spacing, or the molecules are more kinked than in bulk, with end chains that on the average are less aligned along the average molecule long axis.

Chapter 6

Fibres with Cholesteric and Blue Phases

6.1 Finding a suitable LC Mixture

After having studied fibres with relatively simple liquid crystalline phases in the last chapter here the more complex chiral nematic (also called cholesteric) phase should be studied. These LCs show strongly coloured selective reflection in characteristic iridescent colours if their pitch length is in the range of visible light wavelengths (also called short-pitch cholesteric). As this pitch and thereby the colour can be influenced by external factors like temperature and sample thickness, and also the composition of the LC, they are very interesting for use in sensing devices. In some relatively rare cases so-called blue phases appear in a short temperature range between the cholesteric and isotropic phase. They also have some unique characteristics making them attractive for applications but the small temperature range is still a problem so that possible methods for stabilising them have recently gained interest [24, 31, 145]. For a somewhat more detailed introduction into these topics refer to chapter 2.1.2.

To investigate both the short-pitch cholesteric as well as the blue phases a liquid crystal mixture with these properties had to be found. For example the commercially available chiral dopant CB15 is known for inducing blue phases when added to nematic host phases, cf. [134] and the references therein. The first choice therefore was to use one of these already characterised mixtures, a combination of CB15 with 4-cyano-4'-hexyloxybiphenyl (6OCB). According to [146] the clearing temperature increases continuously with amount of 6OCB from -28 to 75 °C and the largest blue phase width is to be expected between 30 and 40% 6OCB (below and above this concentration range it decreases again). At these concentrations the LC mixture is isotropic at room temperature ($T_c = 10$ to 20 °C), so that instead a mixture of 51 wt.% CB15 was prepared that should have a phase sequence of N* ~ 32 BPI* 32.5 BP II* 32.6 iso.

With this LC mixture some very well-filled fibres were achieved as can be seen in fig. 6.1a. But it turned out that when storing them at room temperature crystallisation of the LC started as shown in fig. 6.1b,c. The fibre structure is still present but crystallites larger than the fibre diameter are visible. As there was also some liquid crystal material outside the fibres, especially at crossing points, it is difficult to distinguish whether the process started alongside or inside the fibres and in this way partly destroyed the fibres. Since in the bulk phase no crystallisation was observed one can assume that the encapsulation inside the fibres induced it (crystallisation temperatures were not found in the mentioned or other literature [147, 148, 149]). At present we can only speculate about the exact origin of this change in phase sequence. On the one hand, it may be a primarily physical effect from the strong encapsulation, related for instance to reduced fluctuations and stabilization of a long-range uniform structure by the close proximity throughout the sample of the cylindrical walls. On the other hand, we cannot rule out that some degree of local demixing takes place due to a chemical preference of one of the components with the PVP sheath. Elucidating this phenomenon could be an interesting topic for a follow-up study. Also on varying the LC composition slightly the same behaviour occurred so it was decided to try to find a LC mixture with a much lower crystallisation temperature.

In the literature it was also found that mixtures of CB15 with the nematic mixture RO-TN-404 form cholesteric and blue phases [150, 151]. Since the similar multi-component mixture RO-TN-403 with a large nematic temperature range from below 0 to about 80 °C was available in our laboratory and had itself already been used in the first experiments of coaxial electrospinning with LC core, mixtures between CB15 and this LC were investigated. In a contact sample it was observed that in a certain concentration and temperature range the desired properties are possible. To find out the exact concentration of CB15 needed (which is in general not possible from a contact sample), five mixtures were prepared whose properties are listed in the table below.

Table 6.1: *Investigated CB15 / RO-TN-403 mixtures*

wt.% CB15	phase sequence	optical properties at room temperature and above
22	N* \sim 61 °C iso.	no selective reflection, but birefringence
33	N* \sim 50 °C iso.	selective reflection: red to light blue on heating
42	N* \sim 40 °C iso.	selective reflection: green to yellow on heating
50	N* 28.5 °C BP* 30.2 °C iso.	selective reflection: green-blue in N* phase
61	N* \sim 18 °C iso.	-

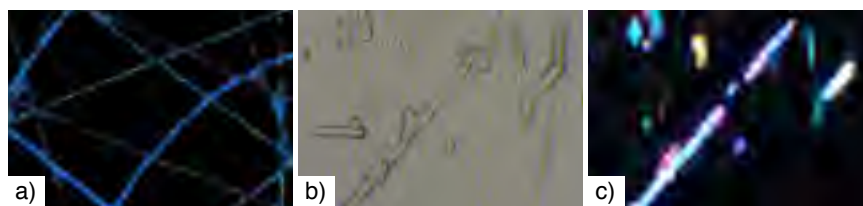


Figure 6.1: PVP fibres filled with the CB15/6OCB mixture. a) Directly after electrospinning; b, c) after storing a few days at room temperature. Photos a) and c) are taken with the sample between crossed polarizers, photo b) is taken without analyzer.

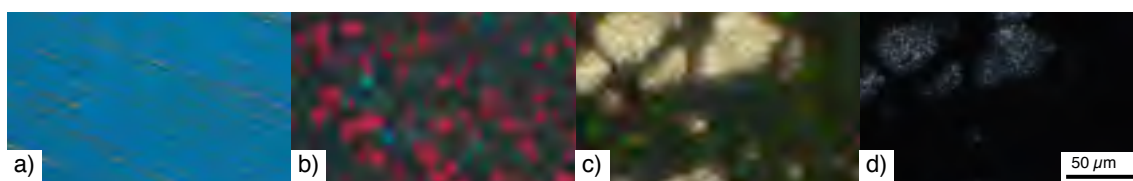


Figure 6.2: Polarising microscopy photographs of the used LC mixture observed with reflected (a – c) or with transmitted light (d). Thick sample at room temperature in cholesteric phase before heating (a). The following photos were taken on cooling the sample from the isotropic state. Blue Phase at 30°C (b) and transition from BP* to N* phase at 28.5°C, the latter showing birefringence in transmission while the first does not (c, d). The yellowish white appearance of N* in (c), rather than the selective reflection blue in (a), is due to an irregular texture ("sand texture") forming initially when cooling from the isotropic phase.

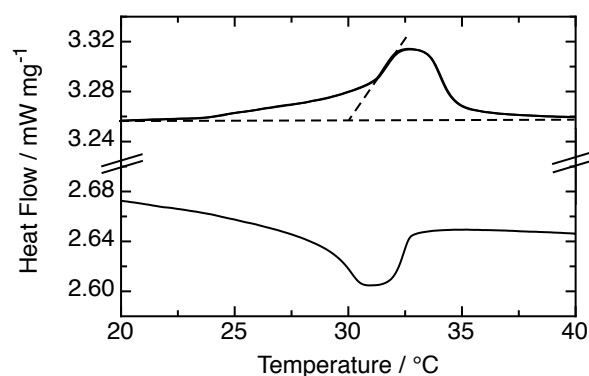


Figure 6.3: DSC thermogram of the LC mixture showing the clearing transition, but not the N* – BP* transition detected in the microscopy investigation. The dotted lines show the determination of the onset temperature of the main peak.

From this experiment it was decided to use the mixture with a content of 50 wt.% CB15 and the phase sequence $N^* 28.5 \text{ BP}^* 30.2 \text{ iso. } / ^\circ\text{C}$ for electrospinning. This mixture shows a green-blue coloured selective reflection that is almost temperature-independent between room temperature and the $N^* - \text{BP}^*$ transition. Polarising microscopy photographs and a DSC thermogram are shown in fig. 6.2 and fig. 6.3. In the DSC the clearing transition is visible as a peak with a shoulder on the low temperature side. The latter might correspond to the $N^* - \text{BP}^*$ transition since the onset temperature of the main peak coincides with the temperature determined in the microscopy investigation. On the other hand the onset temperature of this shoulder is lower than expected for this transition (about 24°C).

When a cholesteric LC is confined between two planar-aligning substrates (with the director along the same direction), these boundary conditions lead to a structure where the gap between the substrates must be filled by an integer number of half-pitches. Since this is not possible with the natural pitch length p_0 for any arbitrary gap distance the LC can adopt to this condition by either increasing or decreasing the pitch length. This behaviour can be used to determine the natural pitch length with a classical Cano wedge cell [12]. As is sketched in the upper part of fig. 6.4 (here using a lens on a flat substrate instead of a wedge, qualitatively an equivalent situation, see below) the distance between the substrates increases continuously, so that the helix must compress or expand at any location where the distance is not equal to an integer number of natural half pitches. This leads to a change in the colour of selective reflection, which will become an important effect in the next section when explaining the colours of the LC core in the fibres. Between regions of compression and expansion a defect appears where the number of half-pitch units in the helix changes by one. From the distances between these defects the natural pitch length can be calculated.

For practical reasons the upper substrate can also be a lens instead of a flat substrate [152] leading to the same effects, except that the areas with the same pitch length (as well as the defects) appear as circles. In this geometry p_0 can be calculated from the lens radius r_{lens} and the radii r_n of defect rings according to eqn. 6.1 (for a derivation of this equation, see appendix A).

$$\frac{p_0}{2} = \sqrt{r_{lens}^2 - r_n^2} - \sqrt{r_{lens}^2 - r_{n+1}^2} \quad (6.1)$$

From the ring radii p_0 is determined to be approximately 310 nm. From this value and from the average of reflected wavelength λ of 460 nm (reflection band of 440– 480 nm as determined from UV-Vis-spectroscopy) also the average refractive index n can be calculated according to $n = \lambda/p_0$ to be about $n = 1.5$.

In the next section again the influence on the LC core in a series of fibres with varied LC content and a sheath of pure PVP (resulting from the 12.5 wt.% solution and standard electrospinning conditions) will be discussed. In the section following

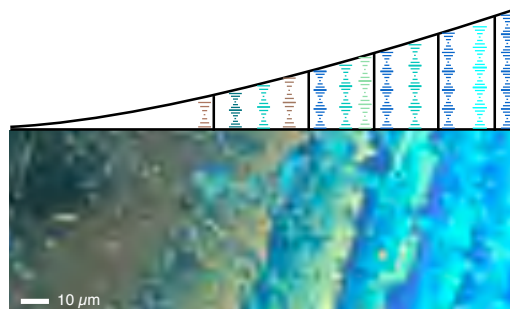


Figure 6.4: Cano preparation of the cholesteric LC used in this work, enclosed between a flat substrate and a lens (severely scratched, giving rise to many defects). The photo shows the colour changes as the helix adjusts to the boundary conditions as is sketched in the upper cartoon part. From ref. [153], reproduced by permission of the Royal Society of Chemistry (RSC).

this, the further studies with SEM to gain information on their outer morphology will be discussed. Thereby it was found that slight changes in composition of the sheath solution were useful which will also be discussed there.

6.2 Phase Behaviour and optical Properties of the LC in PVP Fibres

The LC mixture was pumped directly at room temperature with flow rates increased stepwise from 0.09 to 0.80 ml h^{-1} as was plotted in fig. 3.4. As the cholesteric phase has a lower viscosity than the SmA phase of 8CB a much higher flow rate at the same applied pressure and temperature was achieved (for 8CB the maximum was 0.215 ml h^{-1}). The standard flow rate for the polymer solution was set to 1.8 ml h^{-1} as in the experiments with 8CB. This results in fibres with mean outer diameters increasing from about $2 \mu\text{m}$ to $7 \mu\text{m}$ (cf. fig. 6.5). The even larger diameters found in comparison to those for 8CB (2 to $4 \mu\text{m}$) are due to the higher LC flow rates.

As can be seen in the same plot and in fig. 6.6 a correlation between decreasing fibre diameter and increasing clearing temperature T_c detected in DSC measurements is established that is much greater than in the previous experiments in this thesis. Its value increases from 32.3°C at the highest flow rate (already above the 30.2°C in the bulk) to 43.2°C for the lowest flow rate. Since in the DSC thermograms no overlap of transitions occurred as in previous investigations it is now also possible to calculate the amount of LC core in the fibre from the transition enthalpies, resulting in a maximum value of about 50 wt.% in this series. The exact values of the discussed quantities are summarised in table 6.2.

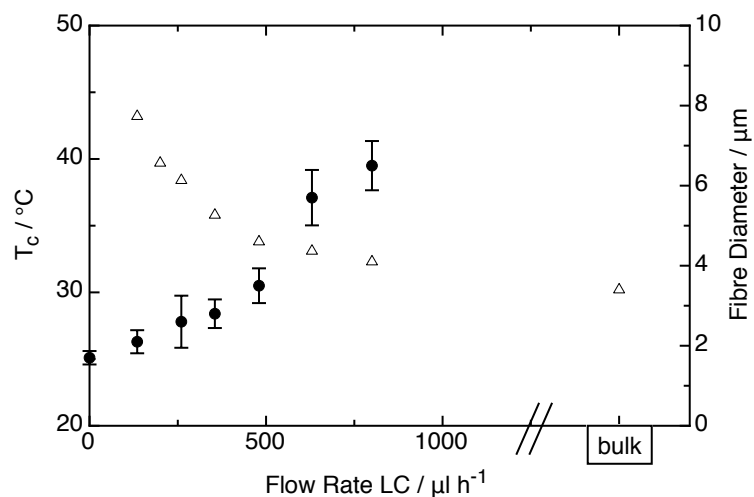


Figure 6.5: Average outer fibre diameter (filled circles) and clearing temperature (empty triangles) of the liquid crystal in the fibre (from DSC), as a function of LC flow rate. All other electrospinning parameters were kept constant. From ref. [153], reproduced by permission of the Royal Society of Chemistry (RSC).

Table 6.2: Thermodynamic data and diameters of fibres with the cholesteric mixture

\dot{V}_{LC} / ml h^{-1}	T_c / $^{\circ}\text{C}$	ΔH_c / J g^{-1}	content LC / wt.%	fibre diameter / μm
0	-	-	-	1.7
0.14	43.2	0.03	2	2.1 ± 0.3
0.20	39.7	0.08	6	-
0.26	38.4	0.15	10	2.6 ± 0.7
0.35	35.8	0.27	19	2.8 ± 0.4
0.48	33.8	0.50	34	3.5 ± 0.4
0.63	33.1	0.65	45	5.7 ± 0.7
0.80	32.3	0.70	48	6.5 ± 0.6
bulk	30.2	1.45	-	-

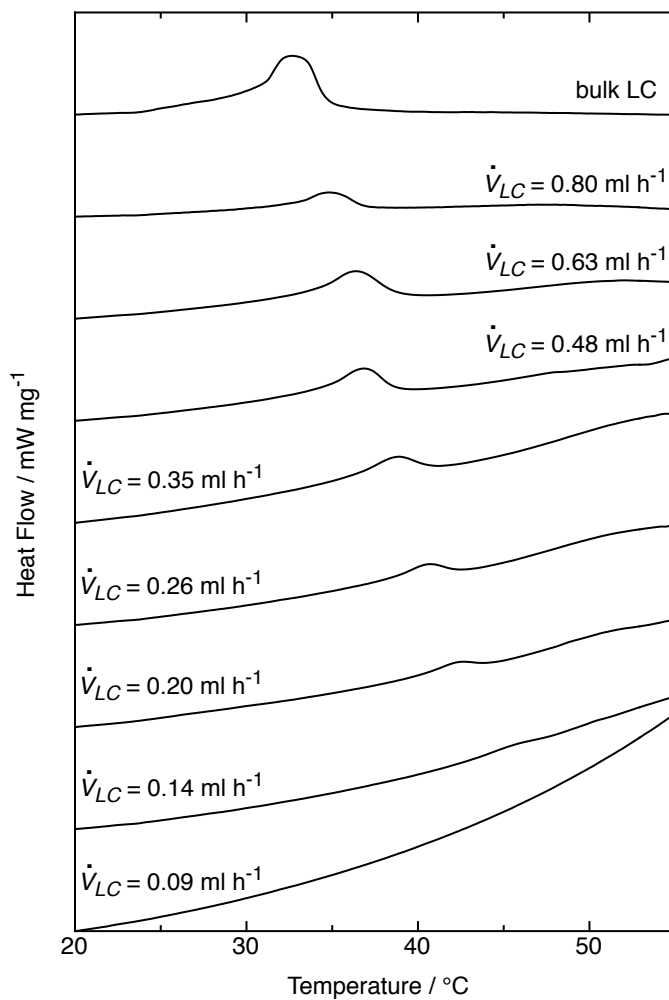


Figure 6.6: Staggered plot of the DSC thermograms (first heating) of fibres with decreasing LC content and of the bulk LC for comparison. The clearing peak becomes smaller as to be expected and is shifted to higher temperatures.

As already seen in previous experiments, below a certain flow rate the first heating parts of the DSC thermograms differ from the immediately following cooling and second heating part. At $\dot{V}_{LC} = 0.35 \text{ ml h}^{-1}$ the clearing peak becomes smaller in the following scans, below this flow rate the clearing peak is only visible in the first heating scan, finally at $\dot{V}_{LC} = 0.09 \text{ ml h}^{-1}$ it disappears completely (cf. fig. 6.6). An explanation is incomplete or no transition to the LC phase in the fibres during the fast cooling in the DSC experiments (10 K min^{-1}). Further to these results, in contrast to the bulk LC behaviour any inter-LC phase transition was never found in the fibres, no matter what fibre thickness. Neither by polarising microscopy nor by DSC could any phase transition between N^* and BP be detected on heating or on cooling. After the following discussion of the optical properties of the fibres, which will lead to a model for the arrangement of the LC molecules in the fibres, this phenomenon can be explained.

Depending on the content of LC in the fibres several textures and complex optical behaviours were found in polarising microscopy of these samples. When observed by reflected light a strong selective reflection appears in many fibres, whose colour and intensity are independent of fibre orientation with respect to the polarisers. When viewing the same fibre by transmitted light the same colours appear but weaker and more blueish, again irrespective of sample orientation, due to an effect that may be called 'selective transmission': because light in the reflection band is circularly polarised the transmitted component passes through the analyser of the microscope regardless of sample orientation. Often this selective transmission colour is overlaid with birefringence. Summarising, three main configurations can be distinguished:

- At medium to large feed rates, yielding thicker fibres, a semi-continuous to continuous LC core is the result (fig. 6.7). This shows selective reflection / transmission at all colours of the spectrum, yellow to blue being most common, overlaid with weak birefringence.
- At low LC feed rates, thus thin fibres, the core is not continuous but separated into elongated drops inside the fibre resulting in a punctuated / dashed texture (fig. 6.8), as was the case for the previously studied fibres. The LC in these drops selectively reflects in various colours ranging from red to blue, sometimes in one and the same fibre. The drops exhibit selective transmission that in some cases is very weak. Birefringence only rarely occurs, then without selective reflection / transmission.
- A few fibres are quite strongly birefringent without any selective reflection / transmission, with the optic axis along the fibre axis (fig. 6.9).

In order to explain these rather complicated optical properties one should first consider what director configurations can be expected for an N^* phase encapsulated inside

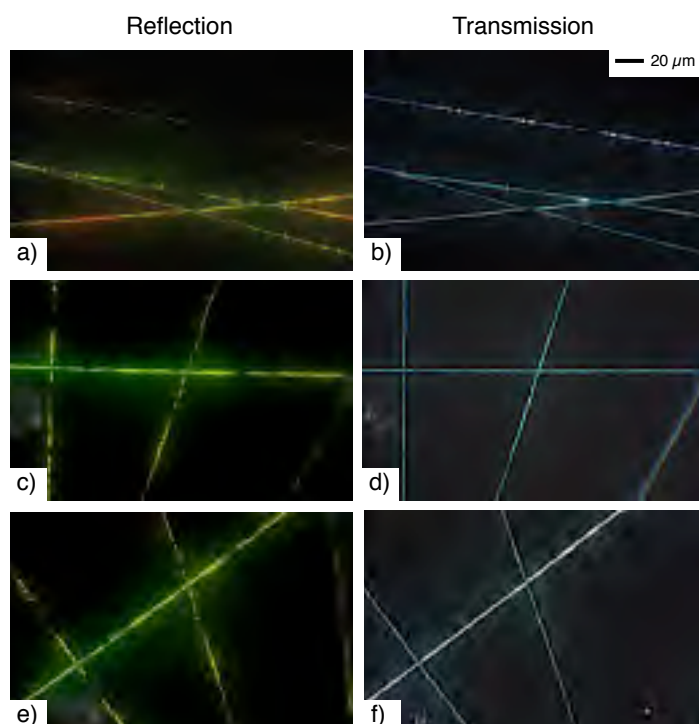


Figure 6.7: Polarising microscopy photos of the semicontinuous texture found in fibres with medium to large diameter. The first row shows the same sample position in reflection (a) as well as transmission (b), strongly coloured red and yellow sections being most pronounced in the former due to the effect of overlaid birefringence weakening the colour in transmission. Pictures (c – f) show another area of the same sample with greenish selective reflection (c, e), the most common in the thickest fibres. In transmission (d, f) the colour is again weaker due to overlaid birefringence. From ref. [153], reproduced by permission of the Royal Society of Chemistry (RSC).

a very thin cylindrical fibre.[¶] As illustrated in fig. 6.10 three different cases should be distinguished. Strong planar anchoring of the mesogen molecules on the inner side of the PVP sheath, as was found in all previous studied PVP-LC composite fibres, can lead to two scenarios: With a core diameter much smaller than the pitch length an unwinding of the natural helix structure (fig. 6.10a) can be expected (for the used short-pitch LC mixture this model would require extremely thin fibres but such were not achieved in these experiments). But if the core diameter is on the order of the pitch length or even

[¶]Even though it turned out by the SEM investigations that a cylindrical shape of the outer morphology is not the case for all fibres, one can still take a cylindrical core as reasonable approximation, since the optical properties show only a gradual change with degree of filling, not a drastic change as might be expected if the core shape changes radically. Moreover, even with a non-cylindrical sheath the core can be cylindrical, as it was sketched in fig. 5.11.

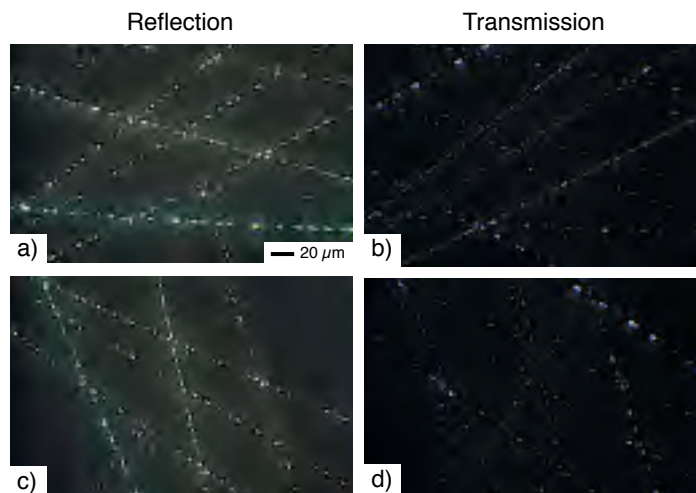


Figure 6.8: *Polarising microscopy photos of the punctuated texture found in the thinnest fibres showing selective reflection in all colours (a, c) and weak transmission (b, d). For photos (c) and (d) the sample has been rotated compared to (a) and (b), revealing close to no orientation dependence in reflection as well as in transmission. From ref. [153], reproduced by permission of the Royal Society of Chemistry (RSC).*

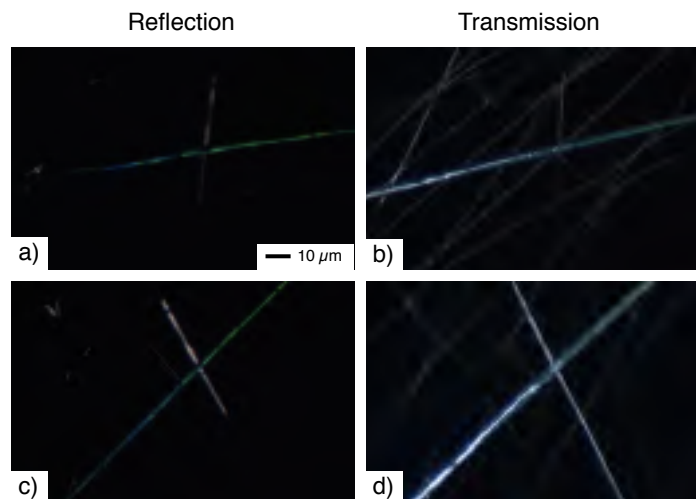


Figure 6.9: *Example of one of the quite rare fibre samples exhibiting strong birefringence but no selective reflection/transmission as one can see from the intensity change on rotating the sample (compare (a) to (c) and (b) to (d), respectively). From ref. [153], reproduced by permission of the Royal Society of Chemistry (RSC).*

larger the planar anchoring will more likely lead to the structure sketched in fig. 6.10c with several helical structures developing perpendicular to the fibre. As a third scenario, if there is no or only weak anchoring, also a configuration with the helix developing *along* the fibre as sketched in fig. 6.10b could be considered.

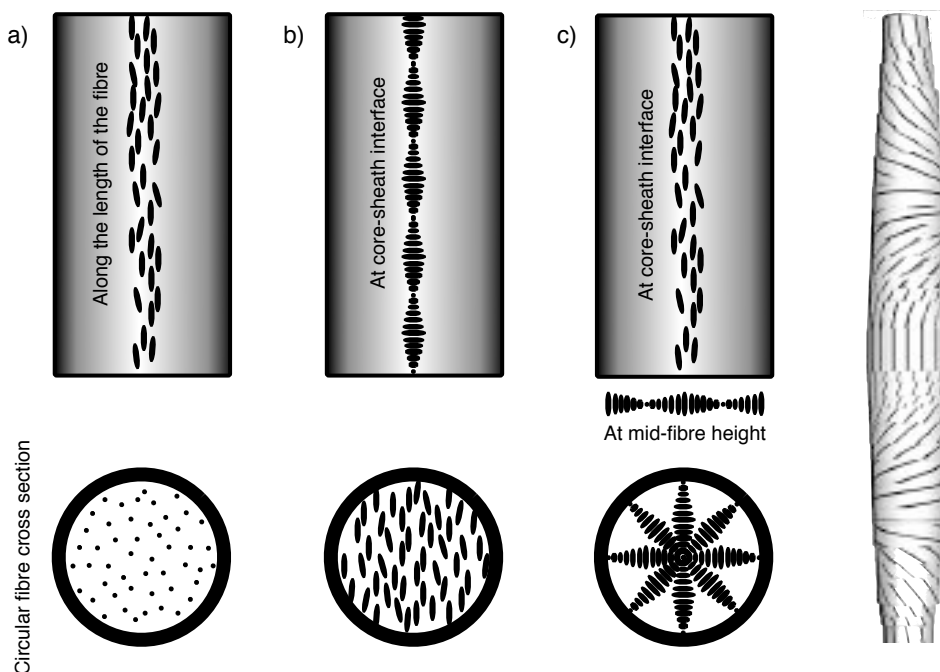


Figure 6.10: Schematic illustration of three possible director configurations for an N^* phase encapsulated inside a cylindrical fibre. (a) Planar director anchoring at the core-sheath interface and unwound helix, (b) no or weak director anchoring and helix along the fibre, (c) planar anchoring at the core-sheath interface and helix perpendicular to the fibre. The latter corresponds to the double twist cylinder geometry (right model, lines indicating the director field) that constitutes the basic building block of blue phases. From ref. [153], reproduced by permission of the Royal Society of Chemistry (RSC).

For the last mentioned model the expected optical properties are strong birefringence and no selective reflection / transmission, as one looks perpendicular to a short-pitch helical modulation of the director. Therefore it could explain the rarely occurring textures like in fig. 6.9 with exactly these optical properties. An advantage of this configuration compared to the models with planar anchoring would be that the helix structure can have its natural pitch and is defect-free regardless of fibre diameter. Since in all previous experiments with PVP as sheath material in combination with a LC core a planar anchoring was found this would however be somehow unexpected if there are alternatives to this configuration. One should also note that this scenario violates the cylindrical symmetry locally, see the perpendicular cross section in fig. 6.10b, even though globally

it is recovered over a fibre length of half the pitch. But it will turn out from the following detailed discussion of the properties of a fibre with the configuration suggested in fig. 6.10c that also this model can explain the behaviour of the strongly birefringent textures.

After having ruled out two director configurations as less likely, what remains is the one sketched in fig. 6.10c. The optical appearance of such a fibre will be dominated by selective reflection / transmission. But as the helix axis lies in the sample plane at mid-fibre height (sketch in the middle of fig. 6.10c) also a weak birefringence should be expected as is indeed observed in the majority of fibres of medium to large filling degree. As can be seen in the drawing of the cross section the planar anchoring boundary condition requires the inner diameter to be a multiple of the helix pitch. It should be noted specially that for symmetry reasons it is in the fibres not possible to have a multiple of *half* pitches, like in the case of flat samples of the Cano-geometry discussed in the previous section, but there must instead be a multiple of a *full* pitches since the director at the centre of the fibre must also be directed along the fibre.

Because a certain variation of fibre inner diameter can be expected also a variation in selective reflection / transmission colour can be expected when the pitch adjusts to the actual fibre diameter.^{||} And indeed there is a substantial variation of colour in the fibres, although the LC in bulk is distinctly blue. When remembering again fig. 6.4, however, dramatic colour changes result only in case of very small substrate separation, allowing only a single helix 'quantum' to develop between the substrates. For larger separations the colour should essentially be the colour of the bulk phase. As all colours of the spectrum appear in the punctually as well as the almost continuously filled fibres (with a tendency of more and more yellow-green colour the larger the fibre) one can conclude that the core diameter must be on the order of a single helix pitch.

This can also be proved by calculating the reflection colours from the natural pitch length p_0 of the LC as a function of core diameter d_{core} . For three different values of p_0 , resulting in red, green and blue reflection in a bulk sample, the results are plotted in fig. 6.11a. With increasing diameter the reflected wavelength increases up to a discontinuity in the function at those diameters at which the structure changes from an expanded to a compressed helix with a smaller reflected wavelength again. With larger diameters these steps and therefore the colour changes become smaller and smaller until the colour is indistinguishable from the bulk colour. When comparing the three plots one can also see that the lower the value of p_0 the smaller the diameters at which this happens.

^{||}In principle it would also be possible to avoid this pitch adjustment in this model if one assumes that the mesogens form an isotropic core of variable diameter surrounded by the helices. But this would generate different optical properties and would not explain the colour variations, and the energy penalty of such a non-uniform structure would most likely be substantially higher than that of the slight stretching or compressing of the helix.

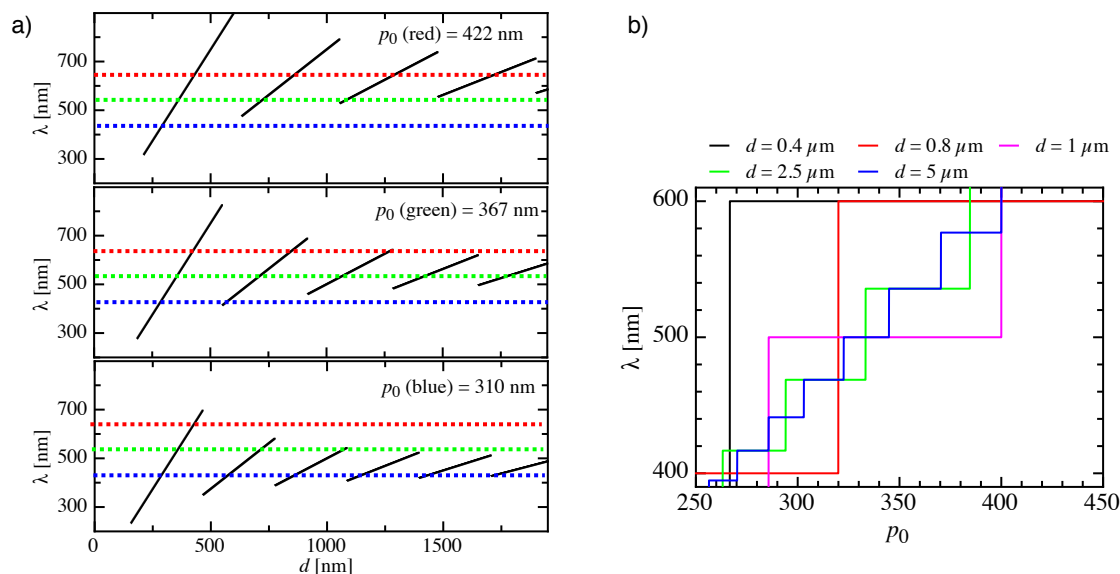


Figure 6.11: a) Selective reflection wavelength λ_{refl} from a cholesteric LC confined in a cylindrical fibre as in fig. 6.10c, calculated for three different values of the natural pitch p_0 that the N^* phase adopts in a bulk sample and plotted as a function of the core diameter d_{core} . As a guide to the eye blue, green and red dotted lines have been drawn roughly at the wavelengths corresponding to these colours. b) Selective reflection wavelength of the same director configuration calculated for five different values of core diameter and plotted as a function of the natural pitch. Both graph taken from ref. [153], reproduced by permission of the Royal Society of Chemistry (RSC). For details on the calculations refer to appendix B.

The lowest diagram with $p_0 = 310$ nm, the approximate natural pitch length of the used LC as determined in the previous section, should correspond to the situation in the fibres. With this it is now possible to explain the colours visible in the fibres and also to give an estimate of the core diameters of these fibres, which turned out to be difficult to establish by other methods (see chapter 6.3). As one can see, the rarely appearing red colour is only possible for a core diameter of about ~ 420 nm, neither less nor more. On the other hand, the yellow-green colour of the majority of fibres with continuous LC filling, i. e. reflection at wavelengths around 500 – 550 nm, can appear for three core diameter ranges: ~ 350 nm, ~ 700 nm and (just barely) ~ 1050 nm. The first range is highly unlikely since then much more red-coloured fibres should appear and also the largest range is unlikely since then blue would have been much more frequently encountered. From these considerations one can conclude that these best filled fibres have a core diameter around ~ 700 nm.

A last conclusion from this diagram is that the reflected wavelength can also be in the UV range for many core diameters, for example in the diameter range 465 – 535 nm.

These fibres will thus not produce any *visibly* reflected colour but still birefringence, which then should appear stronger in comparison to those fibres where it is overlaid by reflection colours. This may be an alternative explanation of the purely birefringent fibres to the model in fig. 6.10b with its non-planar anchoring. One should point out that for the two upper plots in fig. 6.11a this UV range is only reached for very thin fibres, so that for LCs with a larger p_0 it should be possible to avoid these regions if desired.

Supplementary to the already shown plots the same relation between reflection wavelength, natural helix pitch and core diameter can be plotted as λ_{refl} as function of p_0 for certain diameters (fig. 6.11b). It turns out that for core diameters around $1\text{ }\mu\text{m}$ and below, the reflected colour is almost entirely determined by the confinement, any tendency of the cholesteric to change its pitch having essentially no effect. Only above around $2.5\text{ }\mu\text{m}$ a colour change with changing pitch should be detectable (if present in the bulk LC at all).

After having found explanations for two of the LC textures in the fibres, what still remains is the droplet texture of those fibres achieved with the smallest LC flow rates (fig. 6.8). When remembering the other results on various LCs in fibres achieved in this thesis the occurrence of droplets below a certain threshold flow rate is not unexpected. But their optical properties, especially the contrast between strong reflection and weak transmission, are quite bewildering. Without any aim to give a solid explanation, one may speculate that the apparent general darkness of the droplets when viewed in transmission is related to the more complex optical situation of a liquid crystal in droplet geometry, resulting in greater variation of the helix axis as well as stronger refraction effects arising from the curvature in all directions as well as the varying sheath thickness. Moreover, the general reduction in core thickness in these fibres obviously renders the effective birefringence smaller.

From the conclusion that most of the fibres have the director configuration sketched in fig. 6.10c one more, very important aspect of this model must be discussed. As can be seen in the model on the right of this sketch this radial helix arrangement represents nothing else than a double-twist cylinder configuration, the basic building block for blue phases. The same arrangement of a cholesteric LC, not in fibres but in glass capillaries, was already achieved by Kitzerow et al. [52]. With both the cholesteric pitch and the capillary diameter in the range tens of microns, their double-twist configurations were about one order of magnitude larger than the BP* phase building blocks. But with core diameters on the order of one micron, or even less, as was achieved here, the structure *and* the scale of the N* director configuration inside the fibres is equivalent to the BP* phase building block. This means the two phases are effectively degenerate in these fibres and therefore also no N* – BP* transition is observed. For much thicker fibres, with weaker confinement and large enough that a network of several double-twist cylinders

could build up a normal BP* structure, one would eventually expect to see the transition again.

After having discussed in detail the microscopic optical appearance of the composite fibres finally also their macroscopic appearance must be mentioned. For low LC flow rates it is dominated by scattering of the polymer sheath, rendering the spun mat white (as all composite fibres in the previous chapters). However, above $\dot{V}_{LC} \sim 0.7 \text{ ml h}^{-1}$, corresponding to a fibre thickness around $5 \mu\text{m}$, or at lower LC flow rates but a reduced outer flow rate of 1.1 ml h^{-1} and thereby a thinner sheath thickness, the blue selective reflection colour of the LC can be directly seen by the naked eye as shown in fig. 6.12a. On the other hand when instead viewed in transmission the yellow-brown complementary colour is observed (fig. 6.12b). When spun with these conditions the mat therefore gets a threshold-type temperature sensing capability, as the colour disappears and instead the white scattering becomes visible when the LC is heated into the isotropic state as shown in fig. 6.12c.

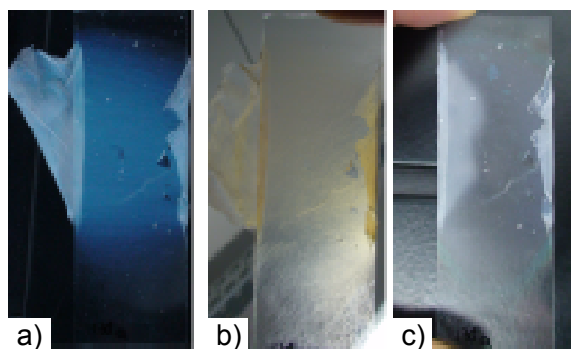


Figure 6.12: *Fibre mat with the colour of the selective reflection of the LC being visible even macroscopically by the naked eye, viewed in reflection (a), transmission (b) and reflection after heating the LC to the isotropic phase (c). From ref. [153], reproduced by permission of the Royal Society of Chemistry (RSC).*

6.3 SEM Investigations of the external Fibre Morphology - Variations of the Polymer Solution

As already discussed, a sheath of PVP was reported prior to our work to give rather poor results in coaxial electrospinning except in combination with a sol-gel-precursor [126, 141]. But instead, in this thesis it turned out that in combination with a liquid crystalline core as a non-Newtonian fluid, it is possible to gain smooth and stable fibres. Furthermore a sheath of pure PVP has some attractive characteristics for the study of the LC in the fibres, like its optical transparency and only weak birefringence compared to the LC core. Following from this argumentation it became important to study also the external fibre morphology in more detail than possible with an optical microscope

used so far. Therefore some of the fibres described in the last part were reproduced and investigated by SEM.

For LC flow rates up to 0.35 ml h^{-1} characteristic examples are shown in fig. 6.13. Higher flow rates were also investigated but these samples were damaged during transport due to softening of the sheath in a too humid atmosphere (which of course affects a thinner sheath more than a thicker one achieved for lower LC flow rates) and are therefore not further discussed. In the upper row of the figure an empty PVP fibre is shown, which turned out to be in most cases not cylindrical as expected, but forming ribbon structures as if the middle part had collapsed. With a LC core more fibres show cylindrical morphology, but still some ribbons are present. Most of the latter seem to be empty like the one in fig. 6.13f.

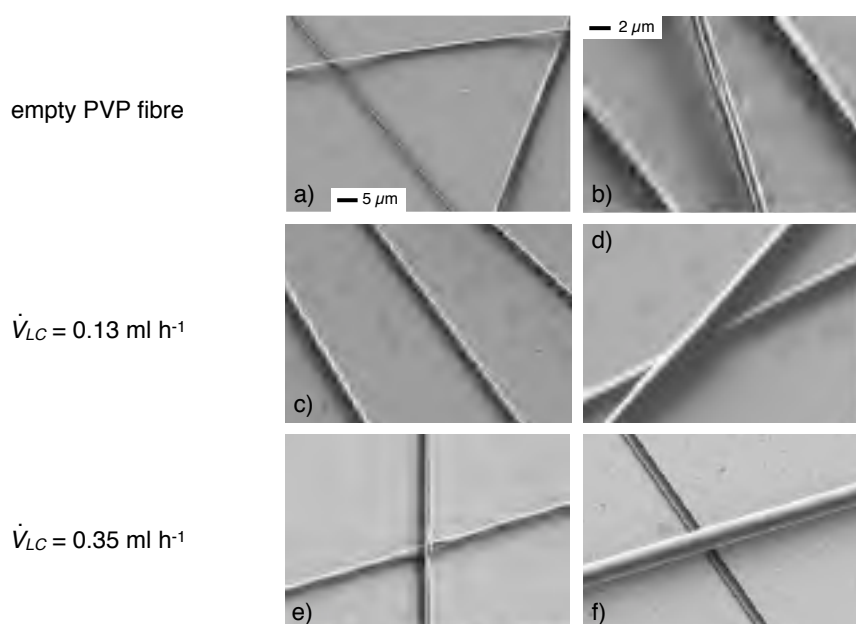


Figure 6.13: SEM images of fibres with PVP sheath and varied LC content.

As in general regular, cylindrical fibres are favourable over the ribbon morphology several strategies were tried to prevent the ribbon structures. First the spinneret to collector distance was increased in order that the fibres have more time to dry during the electrospinning process, therefore should be more stable. Unexpectedly the opposite effect occurred and now only ribbon structures were found that also had many porous areas as if the sheath had been ruptured by the collapse. As second step a more concentrated PVP solution was used to gain a thicker sheath. This improved the situation a little bit in the sense that even for the highest LC flow rate of the original experiment

of 0.8 ml h^{-1} there were cylindrical fibres present, but still there were also ribbons and porous fibres.

So, as a third step, two sheath solutions were tried that contained the sol-gel-precursor $\text{Ti}(\text{O}^i\text{Pr})_4$ and the catalyst acetic acid in an amount, that resulted in 1.5 and 9 wt.% TiO_2 , respectively, in the PVP sheath. With the 1.5 wt.% solution quite inhomogenous fibres were the result, already when observed with the optical microscope. But with 9 wt.% the result was very much improved in the way that independent of LC flow rate the fibres were cylindrical and not fused (cf. SEM images in fig. 6.14) and they also have a smaller distribution of fibre diameters in the same sample (see especially the left column of fig. 6.14 and also the upper row of fig. 6.15). In fig. 6.14e and (h) one can see that on places where fibres cross each other, they flatten each other out slightly, probably because they are, even if dried, not completely rigid when containing only this small amount of TiO_2 .

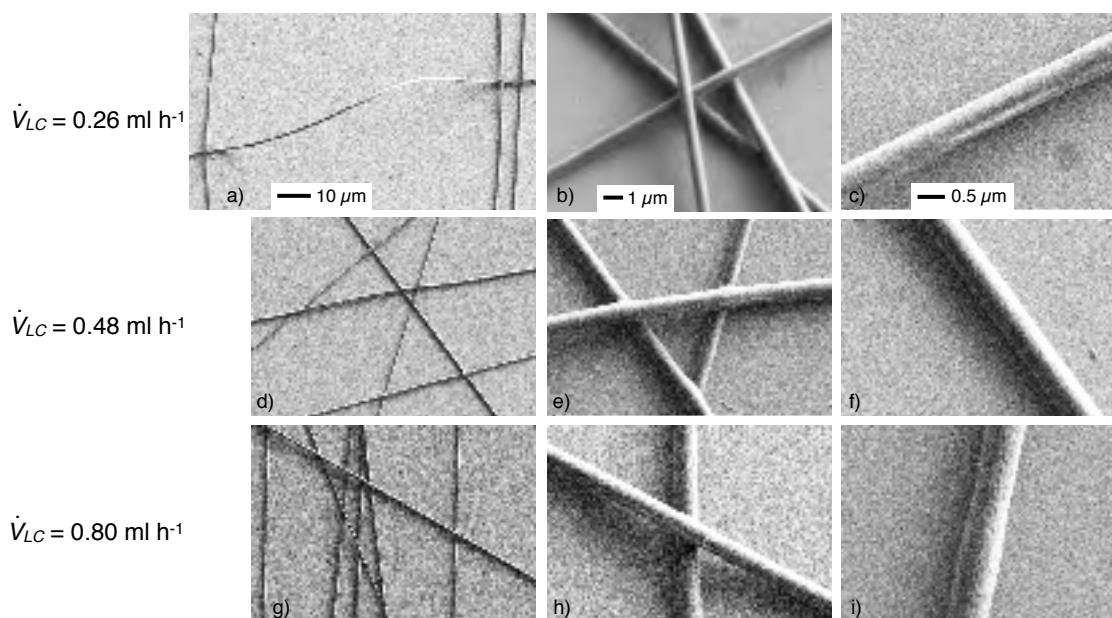


Figure 6.14: SEM images of fibres with PVP/ TiO_2 sheath and varied LC content.

In addition especially for higher LC flow rates the fibres show a small modulation in diameter (cf. fig. 6.14h,i) that might correlate with the droplet structure of the LC core in these fibres: In contrast to those fibres with only PVP as sheath material, even for the highest LC flow rate a droplet distribution, not a (semi-)continuous core is found (cf. fig. 6.15). At the lowest flow rate the droplets show selective reflection almost only in red, whereas at the highest flow rate all colours from red to green are present (see the lowest row of fig. 6.15). As for the fibres with droplet LC core in a sheath of pure

PVP the birefringence is only very weak (therefore not shown). Comparing with the results for the RT-SmC-LC in the same sheath where at similar LC flow rates an almost continuous core was achieved (cf. fig. 5.21), one must conclude that the morphology of the LC core is influenced both by the used sheath material and the used LC. Most likely, the droplet formation in this case is a result of unmatched elongational viscosities between core and sheath fluids.

As a last aspect of the SEM results, the found ribbon like structures might help to explain an unexpected optical behaviour in polarising microscopy of the fibres, that has not yet been mentioned as it seems *not* to be caused by the liquid crystal core, but instead by the sheath, independent of if this was PVP or PVP/TiO₂: In some parts of the fibres the sheath shows visible reflection between crossed polarisers, like for example 6.15 and fig. 6.16. The intensity of the two white to yellow stripes does not change on rotating the sample and when observed in reflection *without* polarisers again the sheath in these areas appears bright. The middle of these fibre parts also show differing colours, in most cases better visible when observed without polarisers than with them.

It turned out that this phenomenon appeared in all produced fibres, independent of which LC was used as core and especially also in PVP fibres without LC core. On heating the samples these reflections disappear slowly from about 80 to 110 °C as shown for an empty fibre in fig. 6.16. When heating fibres in the DSC to such high temperatures irregular and non-repeatable peaks appear, also signalling that some irreversible transformation takes place, possibly connected to a combination of glass transition (at reduced temperature compared to pure, bulk PVP with a glass temperature of 120 to 150 °C) and evaporation of remaining solvent. By closely comparing the photos (c), (f) and (g) in fig. 6.16 taken at room temperature, 105 and 110 °C, respectively, an increase in fibre diameter and fusion between fibres can be seen. On cooling the sample it is not further changed and the original optical appearance is never retained. A possible explanation for these unexpected optical phenomena will be discussed in the following.

The reflected light has apparently been depolarised, as evidenced by the insensitivity to rotations of the sample or of the analyser (the latter obviously affects the surrounding but the bright fibre edges remain bright regardless of analyser setting). This suggests that the origin of the reflected light is a complex scattering process within the fibre. As illustrated in fig. 6.17 such a process is to be expected for a fibre that is hollow, i. e. it is neither filled with liquid crystal, nor does the PVP extend throughout the fibre cross section. This leads to a strong contrast in refractive index both at the outside-sheath interface and the core-sheath interface, since in both cases the non-sheath index is that of air, $n_{air} = 1$, whereas the PVP sheath has a refractive index of about $n_{PVP} \approx 1.5$. Depending on where a light ray enters the sheath (three different examples are drawn in the figure) it may cross an interface a few or many times, it may traverse to the other side of the fibre, and it may even suffer total internal reflection (blue ray in the example).

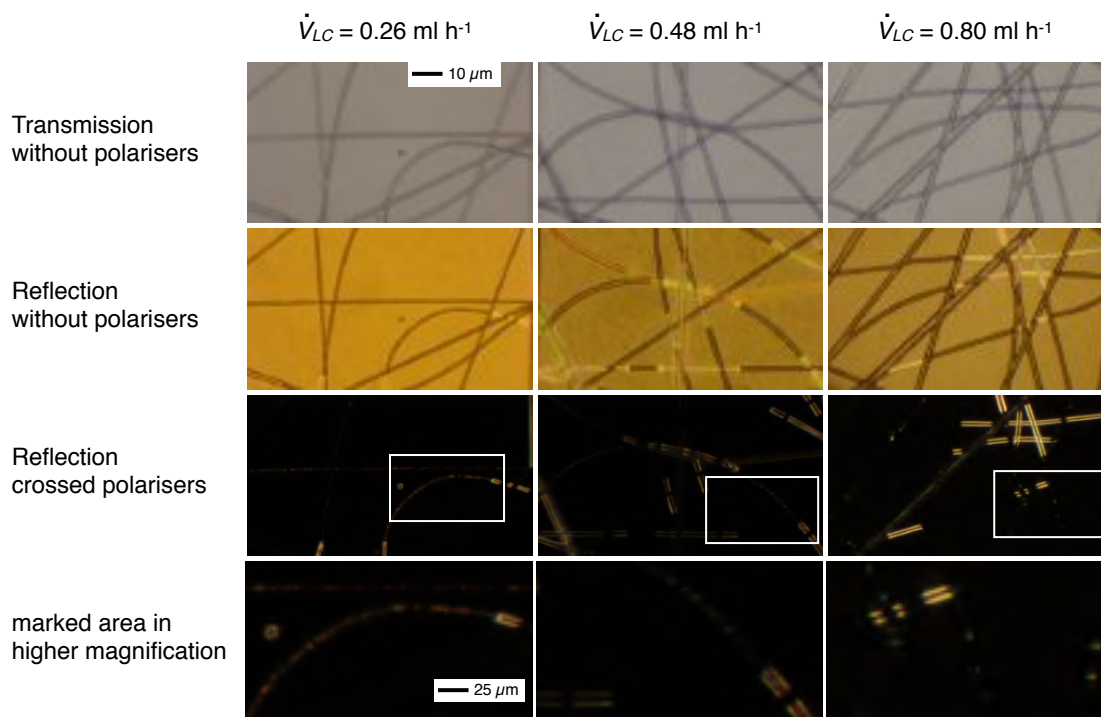


Figure 6.15: POM images of the composite fibres of fig. 6.14 with PVP/TiO₂ sheath at different LC flow rates observed in different modes of optical microscopy. For an explanation of the optical phenomena see the discussion in the main text.



Figure 6.16: Empty PVP fibres with reflecting parts. Upper row: original appearance at room temperature viewed through crossed polarisers in reflection (a) and transmission (b) and without polarisers in transmission (c). Lower row: sample on heating at 95°C (d), 105°C (e,f) and 110°C (g).

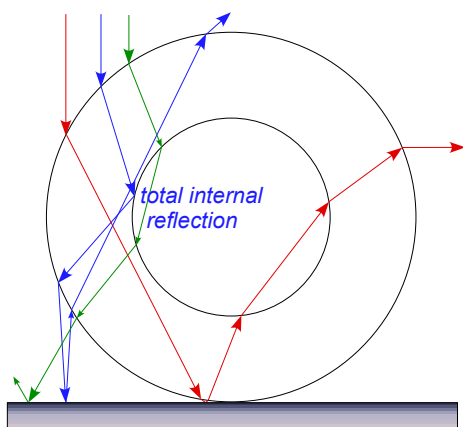


Figure 6.17: Drawing of how light entering at three different locations into a hollow PVP fibre will suffer quite different combinations of refraction and reflection within the fibre, eventually exiting in different directions. At every interface light is also reflected (not drawn apart from the case of total internal reflection of the blue ray at one interface). The colours are just for separating the rays, they do not reflect different light wavelengths. The paths were drawn assuming refractive indices $n_{air} = 1$ and $n_{PVP} = 1.5$.

Every time a ray meets an interface it is not only refracted, as drawn in the figure, but a fraction of the light is also reflected (generally disregarded in the figure). This means that the whole sheath will be traversed by light rays having entered the sheath at different locations and it will essentially glow in any direction along which it is viewed, since some light will exit essentially in any direction. And after having suffered a large number of reflections as well as refraction it is not surprising that the polarisation state has been lost. Although we do not have proof that this is the origin of the cases of brightly but unpolarised shining fibre edges, we believe that this is a very likely explanation, which would need to be corroborated in future experiments and a more detailed analysis.

Moreover, as the fibre diameter is on the order of a micron one can in case of a hollow fibre expect interference effects for light that enters close to the centre, where it will suffer only little refraction. It will be reflected at every interface, and just like in the well-known case of a thin oil film on water, reflected light with a wavelength equal to twice the interface distance will interfere constructively, while that with wavelength equal to four times the distance will interfere destructively, explaining the colourful fibre centres that can be seen without the analyser in the locations where the fibre lacks filling (fig. 6.15, second row). This colour generally disappears when the analyser is inserted, since the light basically retains its original linear polarisation in this case of only a few reflections and very little refraction.

In case of collapse of the cylindrical fibre both optical effects should disappear, as there is then little refractive index contrast and no longer a pair of interfaces spaced a distance apart that is close to visible light wavelengths. This is indeed what happens if the samples are heated up, rendering the softened PVP sheath insufficiently stable to maintain the cylindrical structure in this case of empty core. The explanation for the (partly) hollow fibre geometry that must be assumed from this discussion of optical phenomena most probably is the fact that *all* fibres, also those without core material, were spun through the same coaxial spinneret: The uniformly charged, cylindrical jet

that results from this setup repels itself to such an extent that at least partly a hollow fibre is formed, not a closed one. But such a hollow structure should not be very stable, especially when it consists only of a relatively flexible polymer sheath. If it is not able to support its own weight it would collapse in the middle, resulting in the ribbon structure. The reflection visible in the optical microscope seems to be caused by remaining hollow parts. The tendency that these parts are more common in those fibres containing TiO_2 , making them more stable and rigid, supports this explanation. On heating the fibres also the remaining hollow parts collapse, resulting in a completely flattened, smeared out structure like in fig. 6.16g.

Atomic force microscopy (AFM) experiments in collaboration with Bob-Dan Lechner, Martin-Luther-Universität Halle-Wittenberg revealed that some fibres are softer in the middle than on the sides of the sheath, suggesting also the existence of hollow, non-collapsed parts. To clarify this possible correlation, experiments should be conducted in which POM, SEM and AFM investigations are made on exactly the same sample area to be able to compare the results of these different methods. This would require the deposition of only few characteristic fibres in a way that ensures that individual parts can be detected, a challenge that is still difficult to meet with our equipment. Therefore this kind of experiments remain an open task for the future.

To fully characterise the coaxial fibres one of the still remaining problems is also to establish a generalised way of determining the core diameter, as the use of the LC properties for this purpose like with the cholesteric LC is not generally possible. One method would be to use transmission electron microscopy (TEM) to distinguish between core and sheath material. But as the fibres have diameters in the micrometer range they are too large for this technique. To avoid this it was instead decided to study cuts perpendicular to the fibres long axis with either TEM or SEM. Preliminary investigations were done in collaboration with the group of Dr. Martin Steinhart at the Max Planck Institute of Microstructure Physics in Halle and later with the group of Prof. Goerg Michler at the Institute of Physics at the Martin-Luther-Universität Halle-Wittenberg.

In a first try fibres with PVP sheath were spun directly on aluminium foil and then cut manually (with the substrate). When studying these samples it turned out that all fibres were closed and no coaxial structure was visible any more. In a second try the fibres were first embedded in epoxy resin and cut by microtoming before studying them with SEM. In this case the result was that no fibres structures were distinguishable from the supporting material. Also when repeating this experiment with fibres of composite PVP/ TiO_2 sheath the result was similar. It seems that the fibres were destroyed either during the embedding or the cutting processes. Three factors might have led to this result. First, the sheath is relatively small in comparison to the core material. Second, when the core is a liquid it does not help the stabilisation but instead the core can be

squeezed away. Finally, the sheath is still mainly the elastic polymer not the brittle TiO_2 .

But after these unsuccessful experiments it turned out that there is still another, even though completely new way of investigating coaxial electrospun fibres. By focused ion beam (FIB) milling it is possible to cut slices through the fibres or to remove material layer by layer which enables to reveal the inner structure of the fibres. It is also immediately possible to image the resulting opened fibre by reducing the power of the ion beam. An example of a cut into the sheath of a fibre is shown in fig. 6.18 exposing a channel structure as a result of the coaxial electrospinning process. When having a closer look at this channel one can see its asymmetric shape with a flat bottom and a semicircular upper part. This asymmetry can explain the sometimes found defect-rich textures of the LCs as the space cannot be regularly filled with the natural LC structure. One should note that the core *size* can only be estimated from the gained images as the perspective view onto the fibre makes a correct measurement very difficult.



Figure 6.18: *Electrospun fibre with PVP sheath and chiral nematic LC core after treatment with FIB: the sheath is partly removed and reveals the inner structure of the fibre. Image courtesy of Giusy Scalia and Vera La Ferrara (ENEA Porticy, Italy).*

Chapter 7

Electrospinning with a liquid crystalline Elastomer

In this last chapter some results on mono- and coaxial electrospinning with a main-chain LC elastomer will be described. It was decided to use a polymer developed by Krause et al. as they showed in ref. [41] that it could be electrospun. The synthesis was done by my colleague Martin Kühnast according to this paper and the references therein, the chemical structure can be seen in fig. 7.1. The polymer contains a benzophenone unit as photocrosslinker that reacts on irradiation with UV light. According to the reference the polymer shows a glass transition at 8 °C and a nematic - isotropic transition at 51 °C. When prepared as a thin film these transitions shift after crosslinking to 14 °C and 40 °C, respectively. At the clearing point the crosslinked film showed a spontaneous change in length of about 60 %. For the electrospun fibres no transition temperatures and other observations on the phase transition were stated.

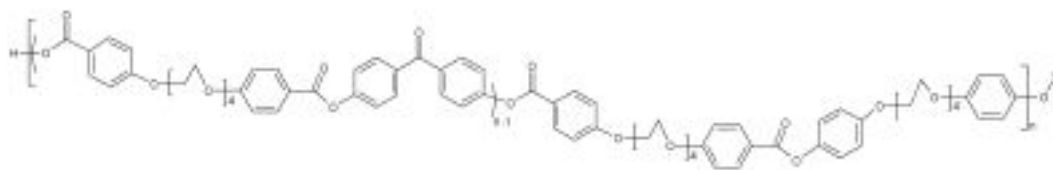


Figure 7.1: Chemical structure of the main-chain liquid crystal elastomer.

In the cited reference [41] it was found that fibres were produced from solutions of 5 and 7.2 wt.% elastomer in CHCl_3 , below these concentrations only droplets were formed. The flow rates were about $0.016 \text{ ml min}^{-1}$, the spinneret to collector distance was 19 cm and the applied voltage was between 21 and 26 kV. The crosslinking could be achieved by placing a UV lamp inside the electrospinning setup at 30 cm distance from the spun

fibre. For our electrospinning setup some changes in these experimental details had to be made, which will be briefly discussed now.

First, it was found that crosslinking the fibres during the electrospinning process was not possible: as soon as the UV lamp was turned on, thick, insoluble fibres were formed at the spinneret, but when the UV lamp was not turned on this did not happen. The reason was that the crosslinking started already in the polymer solution hanging at the spinneret. This again was most likely caused by the fact that in our setup the UV lamp had to be placed much closer to the spinneret and fibre (only about 10 cm) so that much more light reached the polymer. To prevent this the crosslinking was initiated on fibre samples after they had been deposited on glass slides. Secondly, the mentioned concentrations resulted in solutions of too low viscosity for our setup. As the use of a thinner metallic spinneret or a thinner tube to transport the solution was not possible, instead more concentrated solutions were prepared. In a first experiment 15 wt.% elastomer was used, but this resulted in very inhomogenous, thick fibres shown in fig. 7.2a,b. Therefore in a second experiment a solution of 10 wt.% was used, giving better results (cf. fig. 7.2c – f).

The fibre diameters became much thinner and also the distribution of diameters became smaller, compare for example fig. 7.2a and (e) observed with the same magnification. But as can also be seen from the photos the fibres contain many beads and are sometimes very short. The occurrence of beading somehow correlates with the results from Krause et al. that the fibres from the lower concentrated solution (in their case 5 wt.%) were beaded, but those at higher concentration (7.2 wt.%) gave smooth fibres. Also the fibres produced here from the 15 wt.% solution contain no beads, but their general appearance is much worse. The reason for this might be the about 10 times higher flow rate in these experiments in comparison to the literature. From the POM photos in fig. 7.2d and (f) one can see that the fibres are birefringent and in straight segments the director is oriented along the fibre formation axis.

In order to investigate the thermomechanical properties of these fibres it was tried to gain a freely hanging fibre mat with one of the collectors discussed in chapter 4, but it turned out that this was not possible with these fibres. Instead short fibre segments were collected on the aluminium foils and only a few fibres bridged the gap between them. After transferring the latter ones to a glass slide it was found that they were not oriented as they were expected to, but had a rather random distribution with many curled and only few straight segments (cf. fig. 7.2c,e).

A similar behaviour had also been found sometimes in the alignment experiments with poly(vinyl alcohol) of low molar mass ($M_w = 20\,000 - 30\,000 \text{ g mol}^{-1}$) (remember the short discussion at the end of chapter 4). For the elastomer the number-average molar mass had been determined in the cited literature to be $44\,000 \text{ g mol}^{-1}$. For the sample used for the electrospinning experiments here the molar mass was not determined,

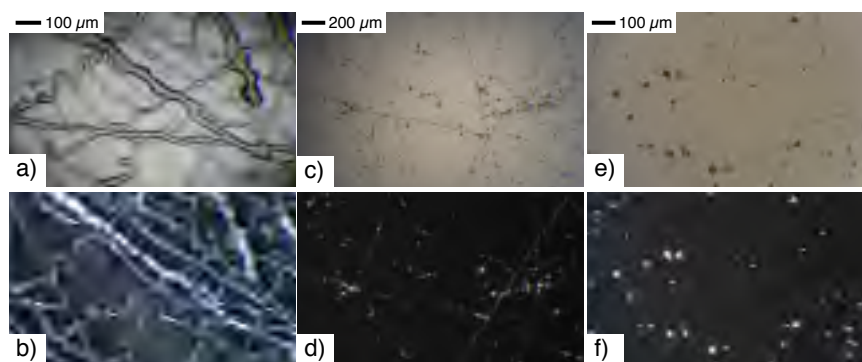


Figure 7.2: Microscopy photos of electrospun fibres of the LC elastomer, the lower row viewed between crossed polarisers. (a, b) Spun from a solution of 15 wt.% polymer in CHCl_3 . (c – f) Spun with 10 wt.% polymer in CHCl_3 at a flow rate of 0.1 ml min^{-1} . The used collector should result in aligned fibres, which were not achieved.

but it should be in a similar range or lower. As was already discussed in chapter 2.2.2 electrospinning with polymers of too low molar mass can lead to the formations of only short, beaded fibres. It seems that with this polymer as well as with the mentioned PVA this limit was reached and the resulting fibres are too short to bridge the gap between the separated electrodes used in our laboratory as aligning collector.

In a new attempt coaxial fibres with PVP as sheath material and the LC elastomer as core were produced which were expected to be easier to align. As the PVP is water-soluble and the elastomer not, the sheath can also be washed away to gain elastomer fibres. Some of the resulting fibres are shown in fig. 7.3. They have a continuous birefringent core with the nematic director aligned along the fibre formation axis as can be seen on rotating the sample. The alignment was slightly better but the formed fibre mat was hanging down to the bottom of the collector, which made it difficult to transfer it from there to another substrate without deformation.



Figure 7.3: Composite fibres with the LC elastomer as core and PVP as sheath observed through crossed polarisers (a) and without them (b). Note that (b – d) show the marked area in the larger magnification. On rotating the sample from (c) to (d) the birefringence of the core is visible with its director along the fibre formation axis.

The PVP was removed by either dropping water on a transferred mat or by inserting the whole mat into water. Unfortunately the mat shrank very much and in an irregular way during this process, so that the alignment was lost. Also it was very difficult to gain a thin layer of fibres observable in a microscope as they were sticking onto themselves as well as to substrates very much. The crosslinking process (performed before removing the PVP) did not result in any change, neither on the phase transition temperature nor were any thermomechanical properties observed.

Instead, the encapsulation into the PVP sheath had a much stronger impact on the phase transition. For non-crosslinked as well as crosslinked core sheath fibres the clearing point of the LC elastomer was observed at about $75 - 85^{\circ}\text{C}$, not at 51°C or 40°C , respectively, as expected from the literature. But after removing the sheath the clearing point was detected around 45°C . The clearing transition in an aligned crosslinked LC elastomer is expected to be accompanied by a decrease in length and an increase in width of the sample. It seems that in the case of the core sheath fibres the surrounding PVP prevents this process and thereby the phase transition. The actual clearing temperature coincides on the other hand well with the temperature at which the PVP starts to soften. The optical appearance of the fibres after heating also resembles that of others heated to such high temperatures.

Chapter 8

Summary and Outlook

8.1 Fibre Alignment

In this part with the electrode height an experimental detail of fibre alignment by the use of a collector formed of split electrodes [119] or a frame-shaped electrode [120] was studied. And indeed it turned out that the height of the electrode with respect to the bottom (cf. the sketch in fig. 4.2 can be seen as an parameter that influences the quality of alignment. The best results were achieved for either flat electrodes or for a height of 15 mm or more (in between for h of 5 and 10 mm the quality got worse). Up to now no sure explanation for this observation can be given, but some possibilities are discussed in the chapter. It was furthermore observed that the quality as well as the possibility to gain aligned fibres at all can also depend on the used polymer material, as for low-molar-mass PVA no alignment was achieved while for higher M_w it was possible [133]. On investigating these topics one must further obey that also other experimental details can play a role like collector material [122], length and width [119, 121] or mechanical stability of the collector.

8.2 Core-sheath Fibres filled with Liquid Crystals

In the following summary of the main part of this thesis the common and / or different features of the produced fibres shall be emphasised in order to point out some more general aspects that one can learn from this study.

It seems that for the outer as well as inner fibre morphology the used sheath material is the most influencing part. For fibres produced with a sheath of pure PVP relatively thick outer diameters of 1 up to several μm were found and in many cases they were not cylindrical as one might expect, but rather flattened out or ribbon-like. In these fibres always the same behaviour for increased liquid crystal content was observed: first the LC formed droplets which became more and more elongated and finally almost continuous.

Instead for fibres with a sheath of PVP and 9 wt.% TiO_2 , the latter produced by a sol-gel-process during spinning, it depended also on the used LC if such a transformation took place: for the investigated RT-SmC-mixture the transformation appeared, while for the cholesteric mixture only droplets were observed even for high LC flow rates. We explain the latter by unmatched elongational viscosities during the spinning process. The advantage of using this sheath solution is however that it produces cylindrical fibres of slightly smaller size and size distribution that are still transparent in the microscope.

For all fibres investigated in this thesis the LC molecules at the interface to the sheath material were found with their long axis along the fibre formation axis. For the nematic and smectic phases this means also that the director points along this direction as could be proved by X-ray experiments. For the cholesteric phase a more complicated configuration has to be adapted as was sketched in fig.6.10c in which the cholesteric phase builds up a helix structure perpendicular to the fibre in which the helix pitch adapts to the inner diameter of the core resulting in sudden variations of the reflected colour. Note that this structure is also degenerate to the Blue Phase also present in the bulk LC material.

Generally some encapsulation effect on the phase transition temperatures is found, but it depends very much on the investigated material how strong this effects is. For example for the RT-SmC-mixture only small effects could be detected, but as only one material with such a phase sequence (SmC - SmA - N - iso.) was investigated it is difficult to discuss whether this is due to the chosen material or due to the chosen phases. For 8CB, with a SmA and a nematic phase, a more distinct effect was observed with a stabilisation of the SmA phase on heating and a stabilisation of the N phase on cooling, most likely due to surface-anchoring on the polymer that prevent transitions. For decreasing LC content and subsequent decreasing fibre diameter a small shift of the clearing transition towards higher temperatures is found while the SmA-N-transition changes from a (weakly) first to a second-order character of the transition.

The largest effect however was found for the cholesteric LC mixture with an increase of the clearing point up to 13 K above the bulk value for the smallest investigated fibres. Note that this mixture is based on the same mixture that Lagerwall et al. [5] had used for their investigations in which a up-shift of the clearing temperature of 20 K above the bulk value was detected. This might indicate that also the chosen material can play a major role in whether stronger or weaker encapsulation effects take place. But as there are up to now only a few materials studied in the context of cylindrical encapsulation in a fibre of the diameter range available by electrospinning this remains to be investigated in more detail.

8.3 Fibres with the LC-Elastomer

For this experiment an LC-elastomer was used, that had been reported already to be possible to electrospin [41]. After some modifications of experimental parameters in comparison to those given in this reference which were due to differences in the electrospinning setup it was possible to repeat their result. But it turned out to be not possible to gain a freely hanging mat of aligned fibres with this material, for further studying them in thermomechanical experiments. To avoid this problem coaxial fibres were spun with the elastomer material surrounded by a PVP sheath, which then were well aligned. Unfortunately when washing away the PVP by rinsing with water the mat shrank in an irregular way so that the orientation got lost again so that the mechanical properties of the elastomer fibres could not be investigated. But for the core-sheath fibres instead another, somehow unexpected behaviour was observed: the clearing temperature is shifted more than 25 K upwards to the softening temperature of the PVP sheath. We explain this by considering that the shape change that would occur in the LC-elastomer during the transition to the isotropic state is prevented by the encapsulation in the sheath until that itself becomes soft enough.

Appendix A

Cano Lens Calculation

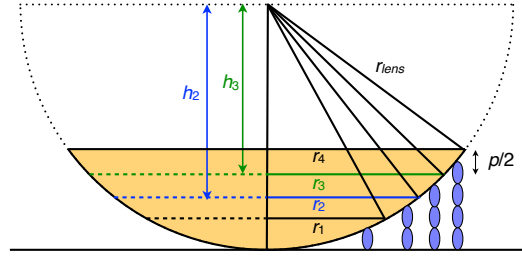


Figure A.1: Sketch of the geometric situation in a Cano lens with the quantities needed to derive the calculation of the cholesteric pitch p .

The Pythagoras' law gives for the defect circles with radii r_2 and r_3 :

$$r_2^2 + h_2^2 = r_{lens}^2 \quad (\text{A.1})$$

and

$$r_3^2 + h_3^2 = r_{lens}^2 \quad (\text{A.2})$$

The vertical distance between two defect circles is $h_2 - h_3 = p/2$. Solving h_2 and h_3 from equations (A.1) and (A.2) results in:

$$p/2 = h_2 - h_3 = \sqrt{r_{lens}^2 - r_2^2} - \sqrt{r_{lens}^2 - r_3^2} \quad (\text{A.3})$$

For an arbitrary choice of circle couple this leads to the relation:

$$p/2 = \sqrt{r_{lens}^2 - r_n^2} - \sqrt{r_{lens}^2 - r_{n+1}^2} \quad (\text{A.4})$$

Appendix B

Calculation of the selective reflection wavelength in fig. 6.11

The following text has been already published as part of the electronic supplementary information to the publication on fibres with cholesteric LC core [153].

When confined inside a cylindrical fibre according to the geometry in fig. 6.10c (page 93) the cholesteric liquid crystal must adapt its helical director modulation to fit the cylinder diameter d , in the sense that an integer number of full helix turns (pitches p) fit in the cylinder, i.e.

$$d = np \tag{B.1}$$

where n is an integer. This relation is fulfilled by the natural pitch p_0 of the helix only in exceptional cases, hence the helix will be either compressed or expanded to fulfil eqn. B.1 with a value of the pitch p that is as close to p_0 as possible.

Under these constraints, the effective number of helix turns i for a given natural pitch p_0 and a given cylinder diameter d can be calculated as:

$$i := \text{Floor}((d + p_0/2)/p_0) \tag{B.2}$$

Note that for $d < p_0/2$ the helix is assumed to be unwound, yielding $i = 0$ in eqn. B.2. For $d \geq p_0/2$ the effective pitch is thus $p = d/i$ with i calculated according to eqn. B.2, yielding selective reflection for light with a wavelength d/i in the liquid crystal medium. We finally achieve the reflected wavelength in air (its refractive index approximated as 1) by multiplying this wavelength by the average refractive index n_{N^*} of our cholesteric liquid crystal, $\lambda = n_{N^*} d/i$, where n_{N^*} has been determined experimentally (see the end of chapter 6.1) to be about 1.5

The full functions for obtaining the graphs in fig. 6.11a,b (page 95), written in the script language (resembling Pascal) of the plotting and fitting software Pro Fit (Quantumsoft), are included below.

```

function ConstrainedPitch;
defaults
    a[1]:= 310, active, 'p_0',1, INF;
    a[2]:=1.5, active, 'n',1,2;
var
    NumberOfPitches: integer;
    NaturalPitch, d, RefIndex: real;
begin
    d:=x;
    NaturalPitch:=a[1];
    RefIndex:=a[2];
    NumberOfPitches:= Floor((d+NaturalPitch/2) / NaturalPitch);
    if NumberOfPitches > 0 then y:= RefIndex*d/NumberOfPitches;
end;

```

```

function ConstrainedPitchFixd;
defaults
    a[1]:= 500, active, 'd',1, INF;
    a[2]:=1.5, active, 'n',1,10;
var
    NumberOfPitches: integer;
    NaturalPitch, d, RefIndex: real;
begin
    NaturalPitch:=x;
    d:=a[1];
    RefIndex:=a[2];
    NumberOfPitches:= Floor((d+NaturalPitch/2) / NaturalPitch);
    if NumberOfPitches > 0 then y:= RefIndex*d/NumberOfPitches;
end;

```

Bibliography

- [1] J. F. COOLEY, Apparatus for electrically dispersing fluids, U.S. patent no. 692631 (1902); Electrical method of dispersing fluids, U.S. patent no. 745276 (1903).
- [2] W. J. MORTON, Method of dispersing fluids, U.S. patent no. 705691 (1902).
- [3] F. REINITZER, *Monatshefte Chemie* **9**, 421 (1888).
- [4] O. LEHMANN, *Z. Phys. Chem.* **4**, 462 (1889).
- [5] J. P. F. LAGERWALL, J. T. MCCANN, E. FORMO, G. SCALIA, and Y. XIA, *Chem. Commun.* , 5420 (2008).
- [6] E. BUYUKTANIR, A. M. FREY, and W. J. WEST, *Polymer* **51**, 4823 (2010).
- [7] A. JÁKLI and A. SAUPE, *One- and two-dimensional Fluids: Physical Properties of smectic, lamellar and columnar Liquid Crystals*, Taylor & Francis, 2006.
- [8] I. DIERKING, *Textures of Liquid Crystals*, Wiley-VCH Verlag, Weinheim, 2003.
- [9] D. DEMUS and L. RICHTER, *Textures of Liquid Crystals*, Verlag Chemie, Weinheim, 1979.
- [10] J. M. SEDDON, Structural Studies of Liquid Crystals by X-ray Diffraction, in *Handbook of Liquid Crystals, Vol. 1*, edited by D. DEMUS, J. GOODBY, G. W. GRAY, and H.-W. SPIESS, Wiley-VCH Verlag, Weinheim, 1998.
- [11] J. P. F. LAGERWALL and F. GIESSELMANN, *ChemPhysChem* **7**, 20 (2006).
- [12] P.-G. DE GENNES and J. PROST, *The Physics of Liquid Crystals*, Clarendon Press, Oxford, 1993.
- [13] D. DEMUS, J. GOODBY, G. W. GRAY, H.-W. SPIESS, and V. VILL, editors, *Handbook of Liquid Crystals*, volume 1-3, Wiley-VCH Verlag, Weinheim, 1998.
- [14] H.-S. KITZEROW and C. BAHR, editors, *Chirality in Liquid Crystals*, Springer-Verlag, New York, 2001.

- [15] D. R. LINK, G. NATALE, R. SHAO, J. E. MACLENNAN, N. A. CLARK, E. KORBLOVA, and D. M. WALBA, *Science* **278**, 1924 (1997).
- [16] R. A. REDDY and C. TSCHIERKE, *J. Mater. Chem.* **16**, 907 (2006).
- [17] G. CHILAYA, Cholesteric Liquid Crystals: Optics, Electro-Optics and Photo-Optics, in *Chirality in Liquid Crystals*, edited by H.-S. KITZEROW and C. BAHR, Springer-Verlag, New York, 2001.
- [18] P. P. CROOKER, Blue Phases, in *Chirality in Liquid Crystals*, edited by H.-S. KITZEROW and C. BAHR, Springer-Verlag, New York, 2001.
- [19] H.-S. KITZEROW, *Ferroelectrics* **395**, 66 (2010).
- [20] E. DUBOISVIOLETTE and B. PANSU, *Mol. Cryst. Liq. Cryst.* **165**, 151 (1988).
- [21] H. YOSHIDA, Y. TANAKA, K. KAWAMOTO, H. KUBO, T. TSUDA, A. FUJII, S. KUWABATA, H. KIKUCHI, and M. OZAKI, *Appl. Phys. Express* **2**, 1501 (2009).
- [22] E. KARATAIRI, B. ROZIC, Z. KUTNJAK, V. TZITZIOS, G. NOUNESIS, G. CORDOYIANNIS, J. THOEN, C. GLORIEUX, and S. KRALJ, *Phys. Rev. E* **81**, 041703 (2010).
- [23] B. ROZIC, V. TZITZIOS, E. KARATAIRI, U. TKALEC, G. NOUNESIS, Z. KUTNJAK, G. CORDOYIANNIS, R. ROSSO, E. G. VIRGA, I. MUSEVIC, and S. KRALJ, *Eur. Phys. J. E* **34**, 1 (2011).
- [24] H. KIKUCHI, M. YOKOTA, Y. HISAKADO, H. YANG, and T. KAJIYAMA, *Nat. Mater.* **1**, 64 (2002).
- [25] T. NOMA, M. OJIMA, H. ASAGI, Y. KAWAHIRA, A. FUJII, M. OZAKI, and H. KIKUCHI, *e-J. Surf. Sci. Nanotech.* **6**, 17 (2008).
- [26] M. OJIMA, T. NOMA, H. ASAGI, A. FUJII, M. OZAKI, and H. KIKUCHI, *Appl. Phys. Express* **2**, 021502 (2009).
- [27] A. YOSHIZAWA, M. SATO, and J. ROKUNOHE, *J. Mater. Chem.* **15**, 3285 (2005).
- [28] A. YOSHIZAWA, Y. KOGAWA, K. KOBAYASHI, Y. TAKANISHI, and J. YAMAMOTO, *J. Mater. Chem.* **19**, 5759 (2009).
- [29] Z. ZHENG, D. SHEN, and P. HUANG, *New Journal of Physics* **12**, 113018 (2010).
- [30] S. TAUSHANOFF, K. V. LE, J. WILLIAMS, R. J. TWIEG, B. K. SADASHIVA, H. TAKEZOE, and A. JÁKLI, *J. Mater. Chem.* **20**, 5893 (2010).

- [31] H. J. COLES and M. N. PIVNENKO, *Nature* **436**, 997 (2005).
- [32] C. OHM, M. BREHMER, and R. ZENTEL, *Adv. Mater.* **22**, 3366 (2010).
- [33] M.-H. LI and P. KELLER, *Phil. Trans. R. Soc. A* **364**, 2763 (2006).
- [34] D. L. THOMSEN, P. KELLER, J. NACIRI, R. PINK, H. JEON, D. SHENOY, and B. R. RATNA, *Macromolecules* **34**, 5868 (2001).
- [35] J. REIBEL, M. BREHMER, R. ZENTEL, and G. DECHER, *Adv. Mater.* **7**, 849 (1995).
- [36] M.-H. LI, P. KELLER, J. Y. YANG, and P. A. ALBOUY, *Adv. Mater.* **16**, 1922 (2004).
- [37] M. BREHMER, R. ZENTEL, G. WAGENBLAST, and K. SIEMENSMEYER, *Macromol. Chem. Phys.* **195**, 1891 (1994).
- [38] J. NACIRI, A. SRINIVASAN, H. JEON, N. NIKOLOV, P. KELLER, and B. R. RATNA, *Macromolecules* **36**, 8499 (2003).
- [39] C. OHM, C. SERRA, and R. ZENTEL, *Adv. Mater.* **21**, 4859 (2009).
- [40] S. V. AHIR, A. R. TAJBAKHSI, and E. M. TERENTJEV, *Adv. Funct. Mater.* **16**, 556 (2006).
- [41] S. KRAUSE, R. DERSCH, J. H. WENDORFF, and H. FINKELMANN, *Macromol. Rapid Commun.* **28**, 2062 (2007).
- [42] J. KUPFER and H. FINKELMANN, *Makromol. Chem. Rapid Commun.* **12**, 717 (1991).
- [43] P. BEYER, E. M. TERENTJEV, and R. ZENTEL, *Macromol. Rapid Commun.* **28**, 1485 (2007).
- [44] H. YANG, A. BUGUIN, J. M. TAULEMESSE, K. KANEKO, S. MERY, A. BERGERET, and P. KELLER, *J. Am. Chem. Soc.* **131**, 15000 (2009).
- [45] P. J. HAINES, editor, *Principles of Thermal Analysis and Calorimetry*, RSC Paperbacks, Cambridge, 2002.
- [46] G. W. H. HÖHNE, W. F. HEMMINGER, and H.-J. FLAMMERSHEIM, *Differential Scanning Calorimetry*, Springer-Verlag, Berlin, 2nd edition, 2003.
- [47] P. ATKINS and J. DE PAULA, *Atkins' Physical Chemistry*, Oxford University Press, 7th edition, 2002.

- [48] F. GIESSELMANN, *Smectic A-C Phase Transitions in Liquid Crystals*, Habilitationsschrift, Technische Universität Clausthal, 1997.
- [49] M. SKARABOT, I. MUSEVIC, and R. BLINC, *Phys. Rev. E* **57**, 6725 (1998).
- [50] M. SKARABOT, S. KRALJ, R. BLINC, and I. MUSEVIC, *Liq. Cryst.* **26**, 723 (1999).
- [51] J. P. F. LAGERWALL, D. D. PARGHI, D. KRÜERKE, F. GOUDA, and P. JAEGERM, *Liq. Cryst.* **29**, 163 (2002).
- [52] H.-S. KITZEROW, B. LIU, F. XU, and P. P. CROOKER, *Phys. Rev. E* **54**, 568 (1996).
- [53] G. P. CRAWFORD, L. M. STEELE, R. ONDRISCRAWFORD, G. S. IANNACCHIONE, C. YEAGER, J. DOANE, and D. FINOTELLO, *J. Chem. Phys.* **96**, 7788 (1992).
- [54] M. KUZMA and M. M. LABES, *Mol. Cryst. Liq. Cryst.* **100**, 103 (1983).
- [55] U. ZAMMIT, M. MARINELLI, F. MERCURI, and S. PAOLONI, *J. Phys. Chem. B* **113**, 14315 (2009).
- [56] T. JIN, B. ZALAR, A. LEBAR, M. VILFAN, S. ZUMER, and D. FINOTELLO, *Eur. Phys. J. E* **16**, 159 (2005).
- [57] T. BELLINI, L. RADZIHOVSKY, J. TONER, and N. A. CLARK, *Science* **294**, 1074 (2001).
- [58] G. S. IANNACCHIONE, G. P. CRAWFORD, S. QIAN, J. W. DOANE, and D. FINOTELLO, *Phys. Rev. E* **53**, 2402 (1996).
- [59] G. CORDOYIANNIS, A. ZIDANSEK, G. LAHAJNAR, Z. KUTNJAK, H. AMENITSCH, G. NOUNESIS, and S. KRALJ, *Phys. Rev. E* **79**, ARTN 051703 (2009).
- [60] M. STEINHART, S. ZIMMERMANN, P. GORING, A. K. SCHAPER, U. GOSELE, C. WEDER, and J. H. WENDORFF, *Nano Lett.* **5**, 429 (2005).
- [61] M. STEINHART, S. MURANO, A. K. SCHAPER, T. OGAWA, M. TSUJI, U. GOSELE, C. WEDER, and J. H. WENDORFF, *Adv. Funct. Mater.* **15**, 1656 (2005).
- [62] M. SKARABOT, R. BLINC, G. HEPPKE, and I. MUSEVIC, *Liq. Cryst.* **28**, 607 (2001).
- [63] N. A. CLARK and S. T. LAGERWALL, *Appl. Phys. Lett.* **36**, 899 (1980).
- [64] K. HIRAOKA, T. MARUYAMA, and Y. NOGUCHI, *Jpn. J. Appl. Phys. 1* **43**, 8173 (2004).

- [65] Q. JI, R. LEFORT, and D. MORINEAU, *Chem. Phys. Lett.* **478**, 161 (2009).
- [66] L. V. MIRANTSEV and E. G. VIRGA, *Phys. Rev. E* **76**, 021703 (2007).
- [67] D. D. L. HERAS, E. VELASCO, and L. MEDEROS, *Phys. Rev. Lett.* **94**, 017801 (2005).
- [68] G. P. CRAWFORD, R. STANNARIUS, and J. W. DOANE, *Phys. Rev. A* **44**, 2558 (1991).
- [69] G. S. IANNACCHIONE and D. FINOTELLO, *Phys. Rev. Lett.* **69**, 2094 (1992).
- [70] G. IANNACCHIONE and D. FINOTELLO, *Liq. Cryst.* **14**, 1135 (1993).
- [71] J. QING, R. LEFORT, R. BUSSELEZ, and D. MORINEAU, *J. Chem. Phys.* **130**, 234501 (2009).
- [72] D. LI and Y. N. XIA, *Adv. Mater.* **16**, 1151 (2004).
- [73] C. BURGER, B. S. HSIAO, and B. CHU, *Annu. Rev. Mater. Res.* **36**, 265 (2006).
- [74] A. GREINER and J. H. WENDORFF, *Angew. Chem. Int. Edit.* **46**, 5670 (2007).
- [75] A. GREINER and J. H. WENDORFF, *Adv. Polym. Sci.* **219**, 107 (2008).
- [76] A. L. ANDRADY, *Science and Technology of Polymer Nanofibers*, John Wiley & Sons, Inc., 2008.
- [77] G. C. RUTLEDGE and S. V. FRIDRIKH, *Adv. Drug Deliver. Rev.* **59**, 1384 (2007).
- [78] D. H. RENEKER and A. L. YARIN, *Polymer* **49**, 2387 (2008).
- [79] D. H. RENEKER, A. L. YARIN, H. FONG, and S. KOOMBHONGSE, *J. Appl. Phys.* **87**, 4531 (2000).
- [80] Q. B. YANG, Z. Y. LI, Y. L. HONG, Y. Y. ZHAO, S. L. QIU, C. WANG, and Y. WEI, *J. Polym. Sci. Part B* **42**, 3721 (2004).
- [81] S. CHUANGCHOTE, T. SAGAWA, and S. YOSHIKAWA, *J. Appl. Polym. Sci.* **114**, 2777 (2009).
- [82] M. M. MUNIR, A. B. SURYAMAS, F. ISKANDAR, and K. OKUYAMA, *Polymer* **50**, 4935 (2009).
- [83] W. K. SON, J. H. YOUK, T. S. LEE, and W. H. PARK, *Polymer* **45**, 2959 (2004).
- [84] S. R. GIVENS, K. H. GARDNER, J. F. RABOLT, and D. B. CHASE, *Macromolecules* **40**, 608 (2007).

- [85] J. B. XIE and Y. L. HSIEH, *J. Mater. Sci.* **38**, 2125 (2003).
- [86] S. L. SHENOY, W. D. BATES, H. L. FRISCHE, and G. E. WNEK, *Polymer* **46**, 3372 (2005).
- [87] M. G. MCKEE, G. L. WILKES, R. H. COLBY, and T. E. LONG, *Macromolecules* **37**, 1760 (2004).
- [88] P. GUPTA, C. ELKINS, T. E. LONG, and G. L. WILKES, *Polymer* **46**, 4799 (2005).
- [89] A. KOSKI, K. YIM, and S. SHIVKUMAR, *Mater. Lett.* **58**, 493 (2004).
- [90] L. J. FETTERS, D. J. LOHSE, D. RICHTER, T. A. WITTEN, and A. ZIRKEL, *Macromolecules* **27**, 4639 (1994).
- [91] Z. JUN, H. Q. HOU, J. H. WENDORFF, and A. GREINER, *E-Polymers*, ARTN 038 (2005).
- [92] C. X. ZHANG, X. Y. YUAN, L. L. WU, Y. HAN, and J. SHENG, *Eur. Polym. J.* **41**, 423 (2005).
- [93] C. MIT-UPPATHAM, M. NITHITANAKUL, and P. SUPAPHOL, *Macromol. Chem. Phys.* **205**, 2327 (2004).
- [94] J. M. DEITZEL, J. KLEINMEYER, D. HARRIS, and N. C. B. TAN, *Polymer* **42**, 261 (2001).
- [95] H. FONG, I. CHUN, and D. H. RENEKER, *Polymer* **40**, 4585 (1999).
- [96] H. Q. LIU and Y. L. HSIEH, *J. Polym. Sci. Pol. Phys.* **40**, 2119 (2002).
- [97] L. YAO, T. W. HAAS, A. GUISEPPI-ELIE, G. L. BOWLIN, D. G. SIMPSON, and G. E. WNEK, *Chem. Mater.* **15**, 1860 (2003).
- [98] S. Q. WANG, J. H. HE, and L. XU, *Polym. Int.* **57**, 1079 (2008).
- [99] X. H. QIN, E. L. YANG, N. LI, and S. Y. WANG, *J. Appl. Polym. Sci.* **103**, 3865 (2007).
- [100] G. K. ARUMUGAM, S. KHAN, and P. A. HEIDEN, *Macromol. Mater. Eng.* **294**, 45 (2009).
- [101] Z. JUN, H. Q. HOU, A. SCHAPER, J. H. WENDORFF, and A. GREINER, *E-Polymers*, ARTN 009 (2003).

- [102] K. MOROTA, H. MATSUMOTO, T. MIZUKOSHI, Y. KONOSU, M. MINAGAWA, A. TANIOKA, Y. YAMAGATA, and K. INOUE, *J. Colloid Interf. Sci.* **279**, 484 (2004).
- [103] C. M. HSU and S. SHIVKUMAR, *Macromol. Mater. Eng.* **289**, 334 (2004).
- [104] S. KOOMBHONGSE, W. X. LIU, and D. H. RENEKER, *J. Polym. Sci. Pol. Phys.* **39**, 2598 (2001).
- [105] R. V. N. KRISHNAPPA, K. DESAI, and C. M. SUNG, *J. Mater. Sci.* **38**, 2357 (2003).
- [106] S. KIDOAKI, K. KWON, and T. MATSUDA, *J. Biomed. Mater. Res. B* **76**, 219 (2006).
- [107] R. JALILI, S. A. HOSSEINI, and M. MORSHED, *Iran. Polym. J.* **14**, 1074 (2005).
- [108] P. SUPAPHOL and S. CHUANGCHOTE, *J. Appl. Polym. Sci.* **108**, 969 (2008).
- [109] S. C. BAKER, N. ATKIN, P. A. GUNNING, N. GRANVILLE, K. WILSON, D. WILSON, and J. SOUTHGATE, *Biomaterials* **27**, 3136 (2006).
- [110] S. D. VRIEZE, T. V. CAMP, A. NELVIG, B. HAGSTROM, P. WESTBROEK, and K. D. CLERCK, *J. Mater. Sci.* **44**, 1357 (2009).
- [111] Y. YANG, Z. JIA, Q. LI, and Z. GUAN, *IEEE Trans. Dielectr. Electr. Insul.* **13**, 580 (2006).
- [112] S. TRIPATANASUWAN, Z. ZHONG, and D. H. RENEKER, *Polymer* **48**, 5742 (2007).
- [113] C. WANG, H.-S. CHIEN, C.-H. HSU, Y.-C. WANG, C.-T. WANG, and H.-A. LU, *Macromolecules* **40**, 7973 (2007).
- [114] M. A. COSTOLO, J. D. LENNHOFF, R. PAWLE, E. A. RIETMAN, and A. E. STEVENS, *Nanotechnology* **19**, ARTN 035707 (2008).
- [115] W. E. TEO and S. RAMAKRISHNA, *Nanotechnology* **17**, R89 (2006).
- [116] J. A. MATTHEWS, G. E. WNEK, D. G. SIMPSON, and G. L. BOWLIN, *Biomacromolecules* **3**, 232 (2002).
- [117] P. KATTA, M. ALESSANDRO, R. D. RAMSIER, and G. G. CHASE, *Nano Lett.* **4**, 2215 (2004).
- [118] L. S. CARNELL, E. J. SIOCHI, N. M. HOLLOWAY, R. M. STEPHENS, C. RHIM, L. E. NIKLASON, and R. L. CLARK, *Macromolecules* **41**, 5345 (2008).

- [119] D. LI, Y. L. WANG, and Y. N. XIA, *Nano Lett.* **3**, 1167 (2003).
- [120] R. DERSCH, T. Q. LIU, A. K. SCHAPER, A. GREINER, and J. H. WENDORFF, *J. Polym. Sci. Part A* **41**, 545 (2003).
- [121] R. JALILI, M. MORSHED, and S. A. H. RAVANDI, *J. Appl. Polym. Sci.* **101**, 4350 (2006).
- [122] H. YAN, L. Q. LIU, and Z. ZHANG, *Appl Phys Lett* **95**, ARTN 143114 (2009).
- [123] I. G. LOSCERTALES, A. BARRERO, I. GUERRERO, R. CORTIJO, M. MARQUEZ, and A. M. GANAN-CALVO, *Science* **295**, 1695 (2002).
- [124] Z. C. SUN, E. ZUSSMAN, A. L. YARIN, J. H. WENDORFF, and A. GREINER, *Adv. Mater.* **15**, 1929 (2003).
- [125] I. G. LOSCERTALES, A. BARRERO, M. MARQUEZ, R. SPRETZ, R. VELARDE-ORTIZ, and G. LARSEN, *J. Am. Chem. Soc.* **126**, 5376 (2004).
- [126] D. LI and Y. N. XIA, *Nano Lett.* **4**, 933 (2004).
- [127] S. N. REZNIK, A. L. YARIN, E. ZUSSMAN, and L. BERCOVICI, *Phys. Fluids* **18**, ARTN 062101 (2006).
- [128] A. L. YARIN, E. ZUSSMAN, J. H. WENDORFF, and A. GREINER, *J. Mater. Chem.* **17**, 2585 (2007).
- [129] A. K. MOGHE and B. S. GUPTA, *Polymer Reviews* **48**, 353 (2008).
- [130] A. L. YARIN, *Polym. Advan. Technol.* **22**, 310 (2011).
- [131] D. LI and Y. N. XIA, *Nano Lett.* **3**, 555 (2003).
- [132] M. NIEDERBERGER and N. PINNA, *Metal Oxide Nanoparticles in Organic Solvents: Synthesis, Formation, Assembly and Application*, Springer Verlag, 2009.
- [133] N. SONNENBERGER, *Elektrospinning von Poly(vinylalkohol)-Fasern mit flüssig-kristallinem Kern*, Bachelor Thesis, Martin-Luther-Universität Halle-Wittenberg, 2009.
- [134] H.-S. KITZEROW, *Mol. Cryst. Liq. Cryst.* **202**, 51 (1991).
- [135] J. THOEN, H. MARYNISSEN, and W. V. DAEL, *Phys. Rev. A* **26**, 2886 (1982).
- [136] G. W. GRAY and J. E. LYDON, *Nature* **252**, 221 (1974).
- [137] S. URBAN, J. PRZEDMOJSKI, and J. CZUB, *Liq. Cryst.* **32**, 619 (2005).

- [138] C. R. SAFINYA, E. B. SIROTA, and R. J. PLANO, *Phys. Rev. Lett.* **66**, 1986 (1991).
- [139] I. W. HAMLEY, V. CASTELLETTO, and P. PARRAS, *Phys. Rev. E* **74**, ARTN 020701 (2006).
- [140] E. ENZ, U. BAUMEISTER, and J. P. F. LAGERWALL, *Beilstein J. Org. Chem.* **5**, ARTN 58 (2009).
- [141] J. E. DIAZ, A. BARRERO, M. MARQUEZ, and I. G. LOSCERTALES, *Adv. Funct. Mater.* **16**, 2110 (2006).
- [142] Y. Y. HU and Z. M. HUANG, *J. Appl. Phys.* **101**, ARTN 084307 (2007).
- [143] I. SCHRÖDER, *Z. Phys. Chem.* **11**, 449 (1893).
- [144] J. J. VAN LAAR, *Z. Phys. Chem.* **63**, 216 (1905).
- [145] S. K. HONG, G. H. LIM, and H. KIKUCHI, *Mol. Cryst. Liq. Cryst.* **511**, 248 (2009).
- [146] P. L. FINN and P. E. CLADIS, *Mol. Cryst. Liq. Cryst.* **84**, 159 (1982).
- [147] H. STEGEMEYER and F. PORSCH, *Phys. Rev. A* **30**, 3369 (1984).
- [148] N. R. CHEN and J. T. HO, *Phys. Rev. A* **35**, 319 (1987).
- [149] F. PORSCH and H. STEGEMEYER, *Liq. Cryst.* **2**, 395 (1987).
- [150] G. HEPPKE, M. KRUMREY, and F. OESTREICHER, *Mol. Cryst. Liq. Cryst.* **99**, 99 (1983).
- [151] F. PORSCH and H. STEGEMEYER, *Chem. Phys. Lett.* **125**, 319 (1986).
- [152] F. OESTREICHER, *Über induziert cholesterische Phasen und neue elektrooptische Anwendungsmöglichkeiten*, Dissertation, TU Berlin, 1984.
- [153] E. ENZ and J. P. F. LAGERWALL, *J. Mat. Chem.* **20**, 6866 (2010).

List of Figures

2.1	Generalised phase diagram with liquid crystalline and classical phases . . .	4
2.2	Schematic structures of a calamitic and a discotic mesogen	4
2.3	Sketches of the N, SmA and SmC phases and typical POM textures . . .	6
2.4	Sketches of X-ray diffraction patterns of N, SmA and SmC phases	8
2.5	Molecular arrangement in a cholesteric phase	11
2.6	Schematic sketch of a double twist cylinder	12
2.7	The three basic structures of LC polymers	13
2.8	Sketches of the micro- and macroscopic shape changes in a LC elastomer .	14
2.9	Schematic illustration of a DSC thermogram	17
2.10	A basic setup for electrospinning	23
2.11	Behaviour of a polymer solution at increasing voltage	24
2.12	Instabilities in a jet path and their consequences	26
2.13	Processing parameters in electrospinning and their influence	27
2.14	Effects of concentration and molecular weight on electrospinning	28
2.15	Electrospinning setup with split electrodes to gain uniaxially aligned fibres	33
2.16	Setup for coaxial electrospinning	34
3.1	The electrospinning setup as developed in our laboratory	36
3.2	Prevention of beading in coaxial fibres	39
3.3	Chemical structures of the used liquid crystals and polymers	42
3.4	Flow rates of the used liquid crystals as function of applied pressure . . .	42
3.5	Experimental procedure of X-ray scattering on oriented fibres	45
4.1	PVA-8CB composite fibres on a frame collector	47
4.2	Sketch of the four investigated collector configurations	48
4.3	Microscope photos and distribution of fibre angles on height-varied collector configuration 1	49
4.4	Distribution of fibre angles for collector configuration 3 and 4	50
4.5	2D-order parameter as dependent on collector geometry and height	51
4.6	Sketch of the electrospun fibres on the investigated collectors	53

4.7	PVA fibres spun on a collector of configuration 1	54
5.1	Microscopy photographs of fibres with 5CB as core material	56
5.2	DSC thermograms of bulk 5CB and of fibres with 5CB core	57
5.3	POM photos of the first 8CB-PVP composite fibres on heating	58
5.4	DSC thermograms of bulk 8CB and of fibres with 8CB core	59
5.5	X-ray measurements on 8CB-PVP composite fibres, part 1	60
5.6	X-ray measurements on 8CB-PVP composite fibres, part 2	61
5.7	X-ray measurements on oriented 8CB-PVP composite fibres	63
5.8	Arrangement of LC molecules and smectic layers in a fibre	63
5.9	Microscopy photographs of fibres with varied LC flow rate	64
5.10	Outer fibre diameters as a function of LC flow rate	64
5.11	Drawing of cross sections through fibres with small and large core	66
5.12	DSC thermograms of 8CB as bulk and in fibres of different LC flow rates	67
5.13	DSC-thermograms of fibres spun with $\dot{V}_{LC} = 20, 45$ and $70 \mu\text{l h}^{-1}$	68
5.14	Microscopy photographs of fibres produced at increasing applied voltage .	70
5.15	Influence of the applied voltage on the outer fibre diameter	70
5.16	Selection of DSC thermograms of the fibres plotted in fig. 5.15	71
5.17	Predicted melting temperatures of the binary system 6OPhPy8 / 8OPhPy8	72
5.18	DSC thermogram of the 50/50 mixture of 6OPhPy8 / 8OPhPy8.	73
5.19	X-ray measurements on the bulk RT-SmC-LC mixture, part 1	74
5.20	X-ray measurements on the bulk RT-SmC-LC mixture, part 2	75
5.21	Microscopy photographs of the resulting fibres at increasing LC flow rate	76
5.22	Outer fibre diameters as a function of LC flow rate	76
5.23	DSC thermograms of fibres with the RT-SmC mixture as core	77
5.24	Complete DSC thermogram of fibres with LC flow rate of $1 \mu\text{l h}^{-1}$	78
5.25	X-ray measurements on RT-SmC-LC composite fibres, part 1	79
5.26	X-ray measurements on RT-SmC-LC composite fibres, part 2	80
6.1	PVP fibres filled with the CB15 / 6OCB mixture	85
6.2	POM photographs of the CB15 / RO-TN-403 mixture	85
6.3	DSC thermogram of the CB15 / RO-TN-403 mixture	85
6.4	Cano preparation of a cholesteric LC	87
6.5	Fibre diameter and clearing temperature as a function of LC flow rate . .	88
6.6	DSC thermograms of fibres with decreasing LC content	89
6.7	POM photos of the semicontinuous texture of medium to large fibres . . .	91
6.8	POM photos of the punctuated texture found in the thinnest fibres	92
6.9	POM photos of fibres with the least found texture	92
6.10	Possible director configurations of a N^* phase in a cylindrical fibre	93
6.11	Calculated selective reflection wavelength of the confined N^* phase	95

6.12	Fibre mat with the colour of selective reflection visible by the naked eye . . .	97
6.13	SEM images of fibres with PVP sheath and different LC flow rates	98
6.14	SEM images of fibres with PVP/TiO ₂ sheath and varied LC content . . .	99
6.15	Optical microscopy images of the composite fibres of fig. 6.14	101
6.16	Empty PVP fibres with reflecting parts	101
6.17	Pathways of light entering at different points into a hollow PVP fibre . . .	102
6.18	Electrospun fibre after treatment with FIB	104
7.1	Chemical structure of the main-chain liquid crystal elastomer.	105
7.2	Microscopy photos of electrospun fibres of the LC elastomer	107
7.3	Composite fibres with the LC elastomer as core and PVP as sheath	107
A.1	Sketch of the geometric situation in a Cano lens	113

List of Tables

2.1	Summary of Landau rules	18
3.1	Flow rates of the used liquid crystals as function of applied pressure . . .	43
6.1	Investigated CB15 / RO-TN-403 mixtures	84
6.2	Thermodynamic data and diameters of fibres with the cholesteric mixture	88

Danksagung

Mein besonderer Dank gilt Prof. Dr. Jan Lagerwall für die Bereitstellung des interessanten Themas und die gute praktische und theoretische Betreuung bei der Anfertigung dieser Arbeit. Außerdem danke ich ihm für die große Geduld und die immer wieder neu gegebenen Anregungen während der schriftlichen Ausarbeitung. Weiterer Dank geht an Prof. Dr. Alfred Blume für die Übernahme der Interims-Betreuung während der letzten Phase der Promotionszeit.

Besonderer Dank gilt auch den anderen Mitarbeitern unserer Gruppe, Sarah Dölle, Martin Kühnast, Hsin-Ling Liang und Stefan Schymura, für die gute Zusammenarbeit, die Unterstützung und mancherlei neue Ideen.

Weiterer Dank geht an die Mitarbeiter und Professoren im Bereich Physikalische Chemie der MLU Halle für die freundliche Aufnahme und die vielseitige Zusammenarbeit. Im besonderen sind dies: Gabriela Tamba für die große Hilfsbereitschaft am Anfang beim Kennenlernen des Instituts, Dr. Ute Baumeister für die Röntgenmessungen, Frau Fölting für die Hilfe bei den DSC-Messungen, sowie Herr Reese und seine Mitarbeiter in der feinmechanischen Werkstatt für die Arbeiten am Elektrosponning-Setup.

Für Diskussionen und praktische Versuche zur elektronenmikroskopischen Bestimmung des Faserinnendurchmessers danke ich Martin Steinhart und seinen Mitarbeitern am Max-Planck-Institut für Mikrostrukturphysik Halle sowie Prof. Dr. Goerg Michler und seinen Mitarbeitern am Institut für Physik der MLU Halle. Dr. Giusy Scalia, Oronzo Calò und Vera La Ferrara von ENEA Portici (Neapel, Italien) danke ich für die SEM- und FIB-Aufnahmen.

Für die finanzielle Unterstützung durch den Exzellenzcluster “Nanostrukturierte Materialien” des Landes Sachsen-Anhalt soll ebenfalls gedankt werden.

Zuletzt gilt meinen Eltern noch besonderer Dank für die große Unterstützung während meines gesamten Studiums und für die immer wieder neu gegebene Motivation.

Lebenslauf

Name: Eva Bianca Enz
Geburtsdatum und -ort: 22.10.1981 in Waiblingen
Staatsangehörigkeit: deutsch

Schulbildung

1988 – 1992 Grundschule
1992 – 2001 Staufer-Gymnasium in Waiblingen
06/2001 Erwerb der allgemeinen Hochschulreife

Studium

10/2001 – 07/2007 Studium zur Diplom-Chemikerin, Universität Stuttgart
 Wahlpflichtfach: Polymerchemie
 Vertiefungsfach: Physikalische Chemie
06/2004 Vordiplom in Chemie
01/2007 – 07/2007 Diplomarbeit “NMR-Untersuchungen zur Ordnung und Dynamik
 von Pyridinium-Tetrafluoroborat in mesoporösen Materialien”
 Institut für Physikalische Chemie, Universität Stuttgart,
 Betreuer: Prof. Dr. Emil Roduner
seit 09/2007 Doktorandin am Institut für Chemie - Physikalische Chemie,
 Martin-Luther-Universität Halle-Wittenberg,
 Betreuer: Prof. Dr. Jan Lagerwall

Publikationsliste

- E. Enz, S. Findeisen-Tandel, R. Dabrowski, F. Giesselmann, W. Weissflog, U. Baumeister, J. Lagerwall, “On the balance between syn- and anticlinicity in smectic phases formed by achiral hockey stick mesogens with and without chiral dopants”, *J. Mater. Chem.* **19**, 2950 (2009).
- S. Schymura, E. Enz, S. Roth, G. Scalia, J. Lagerwall, “Macroscopic-scale carbon nanotube alignment via self-assembly in lyotropic liquid crystals”, *Synthetic Metals* **159**, 2177 (2009).
- E. Enz, U. Baumeister, J. Lagerwall, “Coaxial electrospinning of liquid crystal-containing poly(vinyl pyrrolidone) microfibers”, *Beilstein J. Org. Chem.* **5**, ARTN 58, (2009).
- E. Enz, J. Lagerwall, “Electrospun microfibres with temperature sensitive iridescence from encapsulated cholesteric liquid crystal”, *J. Mater. Chem.* **20**, 6866 (2010).
- H.-L. Liang, E. Enz, G. Scalia, J. Lagerwall, “Liquid crystals in novel geometries prepared by microfluidics and electrospinning”, *Mol. Cryst. Liq. Cryst.* **549**, 69 (2011).
- G. Scalia, E. Enz, O. Calò, D. K. Kim, M. Hwang, J. H. Lee, J. Lagerwall, “Morphology and core continuity of liquid-crystal-functionalized, coaxially electrospun fiber mats tuned via the polymer sheath solution”, accepted for publication in *Macromol. Mat. Eng.* (2012), doi: 10.1002/mame.201200361
- E. Enz, V. La Ferrara, J. Lagerwall, G. Scalia, “Soft nanophotonics with cholesteric liquid crystals confined in electrospun fibers”, submitted to *ACS Nano* (2013).

Erklärung

Hiermit erkläre ich, dass ich die vorliegende Arbeit selbstständig und ohne fremde Hilfe verfasst, andere als die von mir angegebenen Quellen und Hilfsmittel nicht benutzt und die den benutzten Werken wörtlich oder inhaltlich entnommenen Stellen als solche kenntlich gemacht habe.

Eva Enz

Halle (Saale), April 2013